極限状態における QCD 熱力学

佐々木, 崇宏

https://doi.org/10.15017/1441026

QCD thermodynamics under extreme conditions

by

Takahiro Sasaki

Theoretical Nuclear Physics, Depertment of Physics
Graduate School of Science, Kyushu University
6-10-1, Hakozaki, Higashi-ku, Fukuoka 812-8581, Japan

九州大学
KYUSHU UNIVERSITY

Abstract

At high temperature in the early universe or at high density inside neutron stars, matter has quite different properties from those in our everyday lives. If the system has the same energy scale as the binding energy of constituent particles, it cannot retain the structure any more, and consequently more fundamental degrees of freedom appear. This requires us to understand matter from more microscopic viewpoint.

Nucleus is a bound state of interacting protons and neutrons. The dynamics is described by quantum chromodynamics (QCD) as the fundamental theory of quarks and gluons. The QCD vacuum is quite nontrivial because of its nonperturbative nature and has interesting properties such as color confinement and spontaneously chiral symmetry breaking. Color confinement is the phenomenon that color charged particles such as quarks and gluons do not explicitly appear in the low-energy QCD spectrum, whereas colorless particles such as proton, neutron and pion emerge. Spontaneously chiral symmetry breaking is the phenomenon that chiral symmetry is spontaneously broken in the QCD vacuum and hence in nature. It is an origin of mass generation; for example, more than 90 % of nucleon mass is generated by this mechanism. Meanwhile, $U_{\rm A}(1)$ symmetry is anomalous and is related to topological structure of the QCD vacuum.

Since the strong interaction becomes weak at high energy, QCD matter has phase transitions at high temperature (T) or high baryon chemical potential ($\mu_{\rm B}$). A chart of QCD matter in the T -$\mu_{\rm B}$ plane is called the QCD phase diagram. Although the Lagrangian of QCD is well known, the dynamics is still unknown in most of the diagram because of nonperturbative nature of QCD. Hence understanding of the QCD phase diagram is an important subject in nuclear physics and the related fields such

as elementary particle physics, astronomical physics and condensed matter physics.

The first-principle lattice QCD (LQCD) simulations are feasible at finite T and zero $\mu_{\rm B}$, so that the dynamics is well understood there. In other words, the LQCD simulations are not feasible at finite $\mu_{\rm B}$ because of the so-called sign problem, so that our understanding of QCD dynamics is far from perfection there.

As a complementary approach to LQCD simulations, one can consider effective models. In fact, the QCD phase diagram has often been analyzed with effective models. Although the effective models have large ambiguity coming from approximations taken, it can cover a large area in the phase diagram including the finite $\mu_{\rm B}$ region. The Polyakov-loop extended Nambu-Jona-Lasinio (PNJL) model is designed to treat chiral symmetry and color confinement simultaneously, but it cannot reproduce existing LQCD data perfectly.

In this thesis we improve the PNJL model so that the effective model can reproduce existing LQCD data and explain existing neutron-star observations. The improved model is referred to as the entanglement PNJL (EPNJL) model in this thesis. We analyze the following three subjects with the EPNJL model:

(1) Quark mass dependence of the Roberge-Weiss (RW) endpoint
(2) θ-parameter dependence of the QCD phase diagram
(3) Mass-Radius (MR) relation of neutron stars

In subject (1), we compare the EPNJL model results with the LQCD ones, since LQCD simulations are feasible at imaginary chemical potential where the RW phase transition takes place. The RW endpoint is a critical endpoint of the RW phase transition appearing at $\mu_{\rm B} = \pi/3$ and finite T. Very recently, the order of the RW endpoint was analyzed by LQCD simulations. The order is the first order at small and large quark masses, but the second order at intermediate mass. The EPNL model is successful in reproducing the mass dependence of the order of the RW endpoint, whereas the PNJL model is not. The extension of the PNJL model to the EPNJL model is thus essential. In this thesis, we then predict the phase diagram for the order of the RW endpoint as a function of light quark mass $m_{\rm l}$ ad strange quark mass $m_{\rm s}$.

In subjects (2) and (3), meanwhile, we make model predictions, since LQCD simu-

lations are not feasible at finite θ discussed in subject (2) and finite chemical potential considered in subject (3).

In subject (2), we consider nontrivial structure of the QCD vacuum called the θ vacuum. This topological structure is quite interesting from the theoretical point of view and is related to heavy ion collision measurements and the cosmic evolution. In principle, the θ vacuum can be analyzed by adding the θ term to the QCD action. However, LQCD simulations are not feasible at finite θ, and consequently properties of the QCD vacuum are unknown when the θ term is present or generated effectively at finite T. In this thesis, we explore the phase structure for finite θ and suggest a new method of making LQCD simulations feasible for finite θ.

In subject (3), we consider the MR relation of neutron stars as a new constraint on the phase diagram at finite $\mu_{\rm B}$ and zero T. Recently, a heavy neutron star (NS) with 2 $M_\odot$ mass was observed with great accuracy. The accurate observation should be used as a constraint on the QCD phase diagram at finite $\mu_{\rm B}$ and zero T. In this thesis, we determine the QCD phase transition in the entire region of $\mu_{\rm B}$ and T by using LQCD results at large T and zero $\mu_{\rm B}$ and NS-observation results at zero T and large $\mu_{\rm B}$.

Throughout the three subjects, we clarify QCD dynamics and phase transitions under the three extreme conditions. The EPNJL model used is successful in reproducing the results of both first- principle LQCD simulations at large T and imaginary and zero $\mu_{\rm B}$ and NS observations at large $\mu_{\rm B}$ and zero T. This indicates that the model prediction is reliable even in the unknown region of the phase diagram.

This thesis is mainly based on the following four thesis. Three of the four were already published in the international journals and one is in preparation:

- **"Quark-mass dependence of three-flavor QCD phase diagram at zero and imaginary chemical potential: Model prediction"**
  T. Sasaki, Y. Sakai, H. Kouno, and M. Yahiro,
  Physical Review D **84** (2011) 091901.
- **"Theta vacuum and entanglement interaction in the three-flavor Polyakov-loop extended Nambu-Jona-Lasinio model"**

T. Sasaki, J. Takahashi, Y. Sakai, H. Kouno, and M. Yahiro
Physical Review D **85** (2012) 056009.

- **"Practical approach to the sign problem at finite theta-vacuum angle"**
  T. Sasaki, H. Kouno, M. Yahiro
  Physical Review D **87** (2013) 056003.
- **"Determination of quark-hadron transition from lattice QCD and neutron-star observation"**
  T. Sasaki, N. Yasutake, M. Kohno, H. Kouno, and M. Yahiro
  arXiv:hep-ph/1307.0681.

Contents

List of Figures

List of Tables

Chapter 1

INTRODUCTION TO QCD PHASE DIAGRAM

Hot and dense matter is interesting from two viewpoints. First, one can see various phenomena characteristic in many body systems. Second, if the energy scale of system becomes the same order as the binding energy of constituent particles, the system cannot retain the structure any more and more fundamental degrees of freedoms appear. This requires us to understand matter from more microscopic viewpoint.

In this thesis, we concentrate on the energy scale of strong interaction described by Quantum Chromodynamics (QCD) with quark and gluon fields. Since hadrons consist of quarks and gluons, the fundamental degrees of freedom change from hadrons to quarks and gluons in this energy scale. In addition, since QCD has nontrivial vacuum structure, one can expect phase transitions of the vacuum at finite temperatures and densities.

In Secs. 1.1 and 1.2, we will briefly review QCD and its phase diagram. In Sec. 1.3, we explain the first principle lattice QCD and their difficulty for finite density. In Sec. 1.4, we recapitulate general properties of the Polyakov-loop extended Nambu-Jona-Lasinio (PNJL) model. Section 1.5 is devoted to the strategy of our analysis.

1.1 Quantum Chromodynamics

Strong interaction is described by Quantum Chromodynamics (QCD), which is the $SU(3)$ gauge theory with $N_{\rm f}$-flavor fermion fields. The classical QCD Lagrangian is given by

$$\mathcal{L}_{\rm QCD} = \bar{q}(\gamma_\mu D_\mu + \hat{m}_0)q + \frac{1}{4}F_{\mu\nu}F_{\mu\nu} - i\theta\frac{g^2}{64\pi^2}\epsilon_{\mu\nu\sigma\rho}\tilde{F}^a_{\mu\nu}F^a_{\sigma\rho}, \tag{1.1}$$

in Euclidean spacetime [1], where $D_\mu = \partial_\mu + iA_\mu$ is the covariant derivative and $F_{\mu\nu}$ is the field strength of gauge field,

$$F_{\mu\nu} = \partial_\mu A_\nu - \partial_\nu A_\mu + \frac{i}{g}[A_\mu, A_\nu], \tag{1.2}$$

where g is the dimensionless coupling constant. The field q and A_μ represent quark and gluon, respectively. The Lagrangian is invariant under the $SU(3)$ gauge transformation,

$$q(x) \to q'(x) = V(x)q(x), \tag{1.3}$$

$$A_\mu(x) \to A'_\mu(x) = V(x)\left(A_\mu(x) + i\partial_\mu\right)V^\dagger(x), \tag{1.4}$$

with $V(x) \in SU(3)$.

The $N_{\rm f}$-flavor quark fields are defined as $q = {}^{\rm t}(u, d, s, c, b, t)$ and their masses $\hat{m}_0 = {\rm diag}(m_{\rm u}, m_{\rm d}, m_{\rm s}, m_{\rm c}, m_{\rm b}, m_{\rm t})$ are summarized in Table 1.1 [2]. Since we are interested in physics with the energy scales around $\Lambda_{\rm QCD} \approx 200$ MeV, heavy flavors (c, b, t) are negligible. The system with u, d, and s quarks with isospin symmetry in the u-d quark sector is called "2 + 1 flavor", and the system with only 2 light flavors is named "2 flavor".

The last term of Lagrangian (1.1) is called the θ term that violates P and CP conservations [3–5]. The vacuum angle θ is a periodic variable with period 2π. It was known to be an observable parameter [6, 7]. Theoretically, we can take any arbitrary value between $-\pi$ and π for θ. Nevertheless, it is found from the measured neutron electric dipole moment [8] that $|\theta| < 10^{-9}$ [9–13]. Why is θ so small in

$m_{\rm u}$	$m_{\rm d}$	$m_{\rm s}$	$m_{\rm c}$	$m_{\rm b}$	$m_{\rm t}$
2.3 MeV	4.8 MeV	95 MeV	1.275 GeV	4.18 GeV	160 GeV

Table. 1.1 Summary of the current quark mass in QCD [2]. The u-, d-, and s-quark masses are estimates of current quark masses in a mass-independent subtraction scheme such as $\overline{\rm MS}$ at a scale $\mu \approx 2$ GeV. The c-, b- and t-quark masses are the running masses in the $\overline{\rm MS}$ scheme.

zero temperature (T)? This long-standing puzzle is called the strong CP problem. According to the experimental result, the QCD Lagrangian is simply reduced to

$$\mathcal{L}_{\rm QCD} = \bar{q}(\gamma_\mu D_\mu + \hat{m}_0)q + \frac{1}{4}F_{\mu\nu}F_{\mu\nu}. \tag{1.5}$$

1.1.1 Confinement and $\mathbf{Z}_3$ symmetry

In the QCD spectrum, one cannot find color charged particles such as quarks and gluons explicitly but see colorless particles such as pions, proton, and neutron. This phenomenon is called color confinement. This is a representative feature of the non-perturbative QCD vacuum.

To describe the confinement-deconfinement transition at finite T, we first introduce an order parameter in the pure Yang-Mills (YM) limit [1,14]. The YM action for finite T is

$$S_{\rm YM} = \int_0^\beta d\tau \int d^3x \ \frac{1}{4}F_{\mu\nu}F_{\mu\nu} \tag{1.6}$$

where $\beta = 1/T$ and the $A_\mu(\tau, \vec{x})$ satisfy the periodic boundary condition,

$$A_\mu(0, \vec{x}) = A_\mu(\beta, \vec{x}). \tag{1.7}$$

This boundary condition compactifies the imaginary time direction and plays an important role in the thermal system.

Since the $SU(3)$ gauge field is defined in the compactified spacetime, the configuration space is classified with homotopy classes. This topologically nontrivial structure is related to confinement and is visualized as follows. The YM action is invariant

under the periodic gauge transformation by definition. Additionally, one can consider the following aperiodic gauge transformation,

$$A_\mu \to A'_\mu(x) = V(x)(A_\mu(x) + i\partial_\mu)V^\dagger(x), \tag{1.8}$$

where

$$V(\tau + \beta, \vec{x}) = z_n V(\tau, \vec{x}), \tag{1.9}$$

$$V(\tau, \vec{x}) \in SU(3), \tag{1.10}$$

$$z_n \in \mathbb{Z}_3 \subset SU(3). \tag{1.11}$$

The symbol $\mathbb{Z}_3$ denotes the center group of $SU(3)$. It is the discrete subgroup of $SU(3)$ and its elements commute with any element of $SU(3)$. The explicit form of z_n is

$$z_n = \exp\left[i\frac{2\pi}{3}n\right] \tag{1.12}$$

with $n = 0, 1, 2$. The transformation (1.8) is called the $\mathbb{Z}_3$ transformation. Since the $\mathbb{Z}_3$ transformation is a part of the gauge transformation, it is one of the symmetry transformations of the YM Lagrangian density. Moreover the YM partition function is also invariant under the $\mathbb{Z}_3$ transformation, because it preserves the boundary condition for the gauge field (1.7). This symmetry is called $\mathbb{Z}_3$ symmetry. The thermal YM theory has thus the periodic gauge symmetry and $\mathbb{Z}_3$ symmetry.

It is known that $\mathbb{Z}_3$ symmetry is spontaneously broken at high temperature [15]. The order parameter is the Polyakov loop [*1],

$$\Phi = \frac{1}{3}\mathrm{tr_c}(L) \tag{1.13}$$

with

$$L = \exp\left[i\int_0^{1/T} A_4 d\tau\right]. \tag{1.14}$$

[*1] Formally, L is called "Polyakov loop" and Φ is "traced Polyakov loop". However we call Φ as Polyakov loop for simplicity.

This is nothing but the Wilson line in the imaginary-time direction. The Φ is transformed under the $\mathbb{Z}_3$ transformation as

$$\Phi \to z_n \Phi. \tag{1.15}$$

One can show that Φ can be interpreted as a partition function when an infinitely heavy quark is placed in the system;

$$\Phi = e^{-\beta F_{\rm Q}}, \tag{1.16}$$

where $F_{\rm Q}$ is the free energy of heavy quark. If $F_{\rm Q} = \infty$, one cannot put any quark i.e., color charge. This means that the system is in the confined phase. In the pure YM theory the conferment-deconfinement transition is thus understood by $\mathbb{Z}_3$ symmetry, and the order parameter is the Polyakov loop (Φ). This is summarized as

$$\text{Confined phase} : \Phi = 0,\ F_{\rm Q} = \infty,\ \mathbb{Z}_3 \text{ symmetric}$$
$$\text{Deconfined phase} : \Phi \neq 0,\ F_{\rm Q} \neq \infty,\ \mathbb{Z}_3 \text{ symmetry is spontaneously broken}$$

$\mathbb{Z}_3$ symmetry is not exact in realistic QCD with dynamical quarks, since the quarks breaks the symmetry explicitly. Since the exact order parameter of confinement is not discovered yet, and Φ is commonly used as the approximate order parameter.

1.1.2 Spontaneously chiral symmetry breaking

Low-energy QCD phenomena are governed by nearly massless bosons, i.e., pions. The origin of pion is well understood as a Goldstone boson generated by spontaneously chiral symmetry breaking.

In this section, we consider 2-flavor QCD in the chiral limit:

$$\mathcal{L}_{\rm QCD} = \bar{q}\gamma_\mu D_\mu q - \frac{1}{4} F_{\mu\nu} F_{\mu\nu} \tag{1.17}$$

with massless 2-flavor quarks

$$q = \begin{pmatrix} u \\ d \end{pmatrix}. \tag{1.18}$$

Performing the chiral decomposition,

$$q_{\rm L} \equiv \frac{1-\gamma_5}{2} q, \quad q_{\rm R} \equiv \frac{1+\gamma_5}{2} q, \tag{1.19}$$

One can decompose QCD Lagrangian (1.17) into the $q_{\rm L}$ and $q_{\rm R}$ parts;

$$\mathcal{L}_{\rm QCD} = \bar{q_{\rm L}} \gamma_\mu D_\mu q_{\rm L} + \bar{q_{\rm R}} \gamma_\mu D_\mu q_{\rm R} - \frac{1}{4} F^{\mu\nu} F_{\mu\nu}. \tag{1.20}$$

Hence one can perform a phase transformation for each of $q_{\rm L}$ and $q_{\rm R}$ independently. Combined with isospin symmetry, Lagrangian (1.17) is invariant under the $U(2)_{\rm L} \otimes U(2)_{\rm R}$ global transformation,

$$q_{\rm L} \to e^{-i\tau^a \theta^a_{\rm L}} q_{\rm L}, \quad q_{\rm R} \to e^{-i\tau^a \theta^a_{\rm R}} q_{\rm R}, \tag{1.21}$$

where τ_0 and $\vec{\tau} = (\tau_1, \tau_2, \tau_3)$ are the 2×2 unit and Pauli matrices, respectively, and the $\theta^a_{\rm L,R}$ are spacetime-independent parameters. The transformation (1.21) is called chiral transformation. Since the $q_{\rm L,R}$ are eigenstates of the chirality operator γ_5, it is also convenient to define the vector and axial-vector transformations as

$$q \to e^{-i\tau^a \theta^a_{\rm V}} q, \quad q \to e^{-i\tau^a \theta^a_{\rm A} \gamma_5} q, \tag{1.22}$$

where $\theta^a_{\rm V} = \theta^a_{\rm L} = \theta^a_{\rm R}$ and $\theta^a_{\rm A} = -\theta^a_{\rm L} = \theta^a_{\rm R}$. In particular, the transformation with $\theta^a_{\rm V} \propto \delta^0_a$ and $\theta^a_{\rm A} = 0$ is called $U(1)_{\rm V}$ transformation, and $\theta^a_{\rm V} = 0$ and $\theta^a_{\rm A} \propto \delta^0_{\rm a}$ is called $U(1)_{\rm A}$ transformation. The symmetry group is denoted by $U(2)_{\rm L} \otimes U(2)_{\rm R} \simeq U(1)_{\rm V} \otimes U(1)_{\rm A} \otimes SU(2)_{\rm L} \otimes SU(2)_{\rm R}$. Since the $U(1)_{\rm A}$ symmetry is not spontaneously broken but anomalous, we simply omit this symmetry here.

In the QCD vacuum, the chiral condensate,

$$\langle \bar{q} q \rangle = \langle \bar{q_{\rm L}} q_{\rm R} \rangle + \langle \bar{q_{\rm R}} q_{\rm L} \rangle \,, \tag{1.23}$$

becomes finite by the spontaneously breaking of chiral symmetry with finite $\theta^a_{\rm A}$. The chiral symmetry breaking pattern is

$$U(1)_{\rm V} \otimes SU(2)_{\rm L} \otimes SU(2)_{\rm R} \to U(1)_{\rm V} \otimes SU(2)_{\rm V}. \tag{1.24}$$

According to the Nambu-Goldstone (NG) theorem, there are massless NG bosons induced by the symmetry breaking. In the present case the massless bosons are pions.

In nature, the chiral symmetry is explicitly broken by small Higgs masses of quarks. However, u- and d-quark masses are negligible compared with the energy scale of chiral symmetry breaking. Although strange quark is much heavier than u and d quarks, one can apply chiral symmetry approximately. Actually, pions are nearly massless bosons and form meson octet with kaons as expected from the NG theorem.

1.1.3 θ vacuum and $U_{\rm A}(1)$ anomaly

In this subsection, we briefly review the so-called θ vacuum of QCD. It is a topologically nontrivial feature of gauge field and closely related to the $U(1)_{\rm A}$ anomaly of fermion field; see, for example, Ref. [16–21] for detailed discussion.

We consider the path-integral quantization of the pure YM theory in Euclidean space. The partition function is given by

$$Z = \int \mathcal{D}A \ \exp\left[-\frac{1}{4}\int d^4x F^a_{\mu\nu}F^{\mu\nu}_a\right]. \tag{1.25}$$

The $SU(3)$ gauge field A_μ with the proper boundary condition has nontrivial topology; arbitrary configurations $A^{(1)}_\mu$ and $A^{(2)}_\mu$ can belong to different homotopy classes [3]. In other words, they cannot be continuously deformed from each other. The homotopy group is $\mathbb{Z}$ and hence the configuration space is divided into an infinite number of homotopy classes labeled by the winding number,

$$n = -\frac{1}{32\pi^2}\int d^4x \ \epsilon^{\mu\nu\alpha\beta}{\rm Tr}[F_{\mu\nu}F_{\alpha\beta}]. \tag{1.26}$$

It leads to an infinite number of vacua $|n\rangle$. However the instanton solution allows transitions among them and hence the true vacuum is realized as a superposition of $|n\rangle$:

$$|\theta\rangle = \sum_n e^{in\theta}\,|n\rangle\,. \tag{1.27}$$

This is called θ vacuum [6]. Even though the winding number and $|n\rangle$ are gauge-dependent concepts, $|\theta\rangle$ is gauge-invariant eigenstate. This structure requires that the θ term is included in the classical QCD Lagrangian (1.1).

In the path-integral representation, the $U(1)_{\rm A}$ anomaly is understood through the $U(1)_{\rm A}$ transformation of integral measure [22,23]. The Noether current for the $U(1)_{\rm A}$

transformation is

$$\partial_\mu J^\mu_{\rm A} = -\sqrt{\frac{2}{N_{\rm f}}} 2N_{\rm f} \frac{g^2}{32\pi^2} \epsilon^{\mu\nu\alpha\beta} {\rm Tr}[F_{\mu\nu} F_{\alpha\beta}] \tag{1.28}$$

for massless $N_{\rm f}$ flavors. Although the right hand side is a total derivative, the instanton solution yields a non-vanishing value for the integral (1.26) and violate the $U(1)_{\rm A}$ symmetry explicitly. Hence η' meson is not a NG boson but a massive boson.

1.2 QCD at finite temperature and density

QCD is a theory that has the asymptotic freedom, i.e., the coupling becomes weak as the energy scale increases. This changes the QCD vacuum between low- and high-energy scales [24]. Such a transition was first conjectured as a function of temperature (T) and baryon-number density ($n_{\rm B}$) by Cabibbo and Parisi in 1975 [25], although it was motivated by not the asymptotic freedom but by the so-called Hagedorn limiting temperature [26,27]. Figure 1.1 is a schematic plot of QCD phase diagram in the $\mu_{\rm B}$-T plane where $\mu_{\rm B}$ is the baryon-number chemical potential. Since QCD is established theory, the QCD phase diagram should be derived from the QCD partition function analytically nor numerically. However, LQCD simulations cannot be applied to finite density in the current stage because of the so-called sign problem. We will make detail discussions on this point in Sec.1.3. In this section, we briefly review the current status of the phase diagram; see, for example, Refs. [1, 28–38] for the review.

At $T = \mu_{\rm B} = 0$, properties of the QCD vacuum are investigated experimentally. Quarks and gluons are confined in hadrons, whereas chiral symmetry is broken spontaneously there. Since pion is the lightest hadron and is well understood as a NG boson, QCD matter is well described by the chiral perturbation theory. Nucleus also gives information on QCD matter at $T = 0$ and the normal-nuclear density ($\rho_0 = 0.17$ fm^{-3}). Also in this situation, quarks and gluons are confined and chiral symmetry is broken.

At high temperature, quarks and gluons behave as free particles because of the weak coupling, that is, they are deconfined and chiral symmetry is restored. This state is called the quark-gluon plasma (QGP) phase. At high density, quarks should form Cooper pairs through the color anti-triplet channel of quark-quark interaction

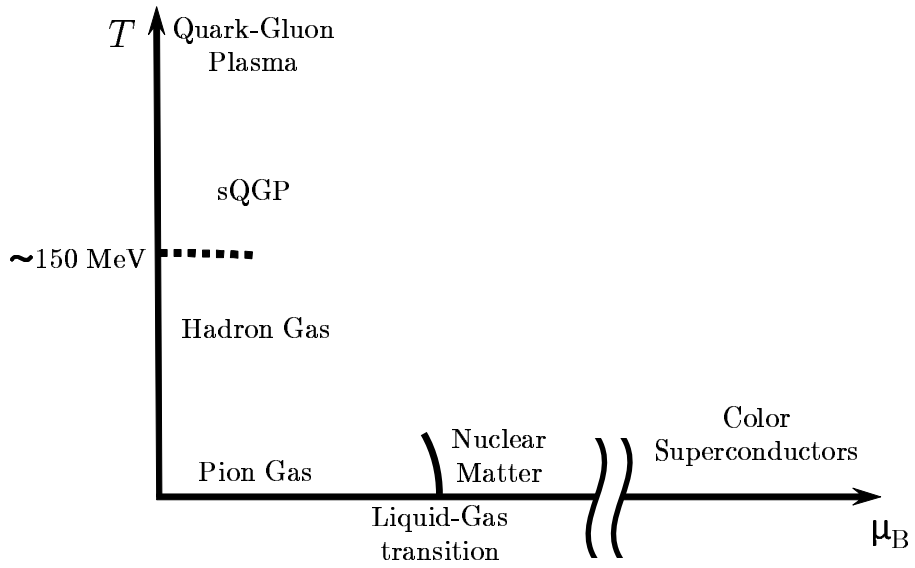

Fig. 1.1 A schematic plot of QCD phase diagram on $\mu_{\rm B}$-T plane.

that makes baryons at $T = \mu_{\rm B} = 0$ and is considered to keep attractive even at high $\mu_{\rm B}$. The state is called the color superconductor (CSC) phase [39, 40]. Hence QCD matter is in difficult phases under the following three limits:

- Hadron phase at $T = \mu_{\rm q} = 0$
- QGP phase in the $T \to \infty$ limit
- CSC phase in the $\mu_{\rm B} \to \infty$ limit

LQCD is a powerful tool to investigate QCD matter at $\mu_{\rm B} = 0$, even though it has the sign problem at finite $\mu_{\rm B}$. QCD phase structure with vanishing chemical potential is then well understood nowadays. Two big groups, Hot QCD and Wuppertal-Budapest collaborations, performed $2 + 1$ flavor LQCD simulations with the improved staggered fermion for nearly physical quark masses. The LQCD simulations showed that a phase transition from the hadron phase to the QGP phase is crossover [41]. The pseudo-critical temperature ($T_{\rm c}$) is around 155 MeV, and temperature dependence of the order parameters and the equation of state (EoS) are given qualitatively [42–44]. Charm quark is also considered in the simulations, but the effect is negligible around $T_{\rm c}$ [45, 46]. The realistic EoS of QCD matter is thus obtained at $\mu_{\rm B} = 0$ by the

simulations. Below T_c, the EoS is well simulated by the hadron resonance gas (HRG) model [42–44]. Just above T_c, meanwhile, the EoS is still far from that predicted by perturbative QCD. This behavior is now called strongly-coupled QGP (sQGP). This was first discovered in heavy-ion collision measurement in the Relativistic Heavy Ion Collider (RHIC) [47] ; see, for example, Refs. [48,49] for the review. Although perturbation does not work just above T_c [50], the behavior of QCD matter at $T \gtrsim 2T_c$ can be understood by the next-to-next-to-leading order hard-thermal-loop perturbation theory [51].

On the μ_B axis where $T = 0$ and μ_B is finite, the phase structure is still unknown, since LQCD simulations are not feasible there. The EoS around the normal nuclear density is investigated by nuclear experiments. The saturation property of nuclear matter indicates that there exists a first-order liquid-gas transition driven by the instability of homogeneous matter [52–54]. Although high-density QCD matter is realized in the inner core of neutron stars (NSs), observations of NSs on mass, radius and cooling curve give only indirect information on high-density QCD matter through. Hence it is not confirmed yet whether the CSC phase and/or the deconfinement phase transition takes place or not in NSs.

1.3 Lattice QCD simulation

LQCD simulation is the most widely used method as the first-principle calculation of QCD. In this section, we briefly review the method and its difficulty at finite density; see, for example, Refs. [55–59] for the review.

LQCD is a regularization scheme in quantum field theories [60], in which fermion fields are defined on each lattice site and gauge fields are on each lattice link to preserve local gauge invariance. In LQCD simulations, the path integral is evaluated by the Monte Carlo (MC) method. In the present stage, LQCD simulation is only a method to confirm QCD in its nonperturbative regime. Actually, LQCD simulations successfully reproduce existing experimental values on hadron masses and their decay constants [61] and the qualitative behavior of nuclear force [62].

At finite quark chemical potential (μ_q), however, LQCD simulations have the so-

called sign problem. For simplicity, we use the notation of continuum QCD without loss of generality. The QCD partition function is give by

$$Z(\mu_{\rm q}) = \int \mathcal{D}A\mathcal{D}\bar{q}\mathcal{D}q \ \exp\left[-(S_{\rm q}+S_{\rm g})\right], \tag{1.29}$$

$$S_{\rm q} \equiv \int d\tau \int d^3\vec{x} \ \bar{q}(\gamma_\mu D_\mu + \hat{m}_0 - \gamma_4\mu_{\rm q})q, \tag{1.30}$$

$$S_{\rm g} \equiv \int d\tau \int d^3\vec{x} \ \frac{1}{4}F^a_{\mu\nu}F^a_{\mu\nu}. \tag{1.31}$$

The path integration is evaluated by the MC method. Practically, one can use the important sampling method for the gluon-field configuration after integrating the quark field:

$$Z(\mu_{\rm q}) = \int \mathcal{D}A \det\mathcal{M}(\mu_{\rm q}) \ \exp\left[-S_{\rm g}\right], \tag{1.32}$$

$$\mathcal{M}(\mu_{\rm q}) \equiv \gamma_\mu D_\mu + \hat{m}_0 - \gamma_4\mu_{\rm q}. \tag{1.33}$$

The $\det\mathcal{M}(\mu_{\rm q})$ is called the fermion determinant and should be a real number to use the important sampling method. At $\mu_{\rm q}=0$, reality of $\det\mathcal{M}(\mu_{\rm q}=0)$ is easily derived. For finite $\mu_{\rm q}$, the determinant is not real but satisfies the relation,

$$(\det\mathcal{M}(\mu_{\rm q}))^* = \det\mathcal{M}(-\mu^*_{\rm q}). \tag{1.34}$$

Hence the important sampling method is not feasible at finite $\mu_{\rm q}$. This is so-called "sign-problem".

In some parameter choices, one can make LQCD simulations without sign problem. Equation (1.34) shows that the fermion determinant is real for pure imaginary chemical potential [63–69]. Moreover, LQCD simulations are feasible for real and imaginary isospin chemical potential $\mu_{\rm I}$ that is related to u- and d-quark chemical potentials, $\mu_{\rm u}$ and $\mu_{\rm d}$, as $\mu_{\rm u}=\mu_{\rm I}$ and $\mu_{\rm d}=-\mu_{\rm I}$ [70].

1.4 Effective model of QCD

The Polyakov-loop extended Nambu-Jona-Lasinio (PNJL) model is one of the most practical effective models for low energy QCD [71–116]. The PNJL model is the Nambu-Jona-Lasinio (NJL) type model [117, 118] in which the quark field is coupled

with the back-ground gauge field [75]; see for example Refs. [119–121] for the NJL model. Using the PNJL model, one can analyze spontaneous chiral symmetry breaking and confinement simultaneously. In this section, basic properties of the model are briefly reviewed.

1.4.1 Polyakov-loop extended Nambu-Jona-Lasinio model

The $N_{\rm f}$-flavor PNJL Lagrangian is obtained as

$$\begin{aligned}\mathcal{L}_{\rm PNJL} = \bar{q}(\gamma_\nu D_\nu + \hat{m}_0 - \gamma_4\hat{\mu})q - G_1\sum_a\left[(\bar{q}T_a q)^2 + (\bar{q}i\gamma_5 T_a q)^2\right] \\ -G_2\left[\det_{ij}\bar{q}_i(1+\gamma_5)q_j + \det_{ij}\bar{q}_i(1-\gamma_5)q_j\right] + \mathcal{U}(\Phi[A],\Phi^*[A],T),\end{aligned} \tag{1.35}$$

where $D_\nu = \partial_\nu - i\delta_{\nu 4}A_4^a\lambda_a/2$ with the Gell-Mann matrices λ_a. The $N_{\rm f}$-flavor quark fields q have masses $\hat{m}_0 \equiv {\rm diag}(m_{\rm u}, m_{\rm d}, \cdots)$, where the matrix $\hat{\mu} \equiv {\rm diag}(\mu_{\rm u}, \mu_{\rm d}, \cdots)$ denotes the quark-number chemical potential matrix in the flavor space. The G_1 is a coupling constant of $SU_{\rm V}(N_{\rm f})\otimes SU_{\rm A}(N_{\rm f})\otimes U_{\rm V}(1)\otimes U_{\rm A}(1)$ symmetric quark interaction. The G_2 is a coupling constant of the Kobayashi-Maskawa-'t Hooft (KMT) determinant interaction which breaks $U_{\rm A}(1)$ symmetry explicitly, where the determinant runs in the flavor space [4, 5, 122, 123].

The gauge field A_μ is treated as a homogeneous and static background field in the PNJL model. The Polyakov-loop Φ and its conjugate Φ^* are determined in Euclidean spacetime by

$$\Phi = \frac{1}{3}{\rm tr}_{\rm c}(L), \qquad \Phi^* = \frac{1}{3}{\rm tr}_{\rm c}(\bar{L}), \tag{1.36}$$

where $L = \exp(iA_4/T)$ with $A_4/T = {\rm diag}(\phi_r, \phi_g, \phi_b)$ in the Polyakov-gauge; note that the λ_a are traceless and hence $\phi_r + \phi_g + \phi_b = 0$. We, therefore, obtain

$$\begin{aligned}\Phi &= \frac{1}{3}(e^{i\phi_r} + e^{i\phi_g} + e^{i\phi_b}) \\ &= \frac{1}{3}(e^{i\phi_r} + e^{i\phi_g} + e^{-i(\phi_r+\phi_g)}), \\ \Phi^* &= \frac{1}{3}(e^{-i\phi_r} + e^{-i\phi_g} + e^{-i\phi_b}) \\ &= \frac{1}{3}(e^{-i\phi_r} + e^{-i\phi_g} + e^{i(\phi_r+\phi_g)}).\end{aligned} \tag{1.37}$$

a_0	a_1	a_2	b_3
3.51	−2.47	15.2	−1.75

Table. 1.2 Summary of the parameter set in the Polyakov-loop potential sector determined in Ref. [94]. All parameters are dimensionless.

We use the Polyakov-loop potential $\mathcal{U}$ of Ref. [94]:

$$\mathcal{U} = T^4 \left[-\frac{a(T)}{2}\Phi^*\Phi + b(T)\ln(1 - 6\Phi\Phi^* + 4(\Phi^3 + \Phi^{*3}) - 3(\Phi\Phi^*)^2) \right] \tag{1.38}$$

with

$$a(T) = a_0 + a_1\left(\frac{T_0}{T}\right) + a_2\left(\frac{T_0}{T}\right)^2, \quad b(T) = b_3\left(\frac{T_0}{T}\right)^3. \tag{1.39}$$

There are five parameters, $(a_0, a_1, a_2, b_3, T_0)$, and they are determined to reproduce LQCD results at finite T in the pure gauge limit. The $\mathcal{U}$ is constructed to reach the Stefan-Boltzmann (SB) limit at large T:

$$\lim_{T\to\infty} \mathcal{U} = -\frac{14\pi^2}{90}T^4 \tag{1.40}$$

leading to $a_0 = 3.51$. LQCD results show that a first-order deconfinement phase transition occurs at $T = T_0$ in the pure gauge limit. This leads to an another constraint,

$$b_3 = -0.108(a_0 + a_1 + a_2). \tag{1.41}$$

The parameters except T_0 are summarized in Table 1.2. The original value of T_0 is 270 MeV determined from the pure gauge LQCD data, but the PNJL model with this value of T_0 yields a larger value of the pseudocritical temperature T_c of the deconfinement transition at zero chemical potential than $T_c \approx 173 \pm 8$ MeV predicted by full LQCD [124–126]. We, therefore, rescale T_0 to 212 MeV so that the PNJL model can reproduce $T_c = 174$ MeV [100].

1.4.2 Two-flavor PNJL model

The two-flavor PNJL Lagrangian is obtained in Euclidean spacetime as

$$\mathcal{L} = \bar{q}(\gamma_\nu D_\nu + \hat{m}_0 - \gamma_4\hat{\mu})q - G_1\sum_{a=0}^{3}\left[(\bar{q}\tau_a q)^2 + (\bar{q}i\gamma_5\tau_a q)^2\right] \\ -G_2\left[\det_{ij}\bar{q}_i(1+\gamma_5)q_j + \det_{ij}\bar{q}_i(1-\gamma_5)q_j\right] + \mathcal{U}(T,\Phi,\Phi^*). \tag{1.42}$$

The two-flavor quark fields $q = (q_\mathrm{u}, q_\mathrm{d})$ have masses $\hat{m}_0 = \mathrm{diag}(m_\mathrm{u}, m_\mathrm{d})$, the quark-number chemical potential matrix $\hat{\mu}$ is defined by $\hat{\mu} = \mathrm{diag}(\mu_\mathrm{u}, \mu_\mathrm{d})$, and τ_0 and $\vec{\tau} = (\tau_1, \tau_2, \tau_3)$ are the 2×2 unit and Pauli matrices in the flavor space, respectively. In this section, we take $G_1 = G_2 \equiv G/2$. This reduces Lagrangian (1.42) to a simpler form,

$$\mathcal{L} = \bar{q}(\gamma_\nu D_\nu + \hat{m}_0 - \gamma_4\hat{\mu})q - G\left[(\bar{q}q)^2 + (\bar{q}i\gamma_5\vec{\tau}q)^2\right] + \mathcal{U}(T,\Phi,\Phi^*). \tag{1.43}$$

Although this choice overestimates the anomaly term, the effect does not affect our discussion particularly under the meanfield approximation. In Chap. 3. we will take more realistic values for G_1 and G_2.

Performing the mean-field approximation and the path integral over the quark field, one can obtain the thermodynamic potential Ω (per volume) as

$$\frac{\Omega}{V} = G\sigma^2 + \mathcal{U} - 2N_\mathrm{c}\sum_{f=\mathrm{u,d}}\int_\Lambda \frac{d^3p}{(2\pi)^3}E_f \\ -\frac{2N_\mathrm{c}}{\beta}\sum_{f=\mathrm{u,d}}\int\frac{d^3p}{(2\pi)^3}\Big\{\ln\Big[1+3\Phi e^{-\beta(E_f-\mu_f)}+3\Phi^* e^{-2\beta(E_f-\mu_f)}+e^{-3\beta(E_f-\mu_f)}\Big] \\ +\ln\Big[1+3\Phi^* e^{-\beta(E_f+\mu_f)}+3\Phi e^{-2\beta(E_f+\mu_f)}+e^{-3\beta(E_f+\mu_f)}\Big]\Big\} \tag{1.44}$$

with

$$E_f = \sqrt{\vec{p}^{\,2}+M_f^2},\quad M_f = m_0 - 2G\sigma,\quad \sigma \equiv \langle\bar{q}q\rangle\,. \tag{1.45}$$

The three-dimensional cutoff is introduced for the momentum integration, since this model is nonrenormalizable; this regularization is denoted by $\int_\Lambda$ in Eq. (1.44). For simplicity, we assume isospin symmetry for u and d quarks by setting $m_l \equiv m_\mathrm{u} = m_\mathrm{d}$.

m_l(MeV)	Λ(MeV)	G(GeV^{-2})
5.5	631.5	5.498

Table. 1.3 Summary of the parameter set in the 2 flavor NJL model taken from Ref. [127].

The present model thus has three parameters of m_0, Λ, and G. A typical parameter set is shown in Table 1.3 [127]. Assuming $m_0 = 5.5$ MeV, we determined Λ and G from the pion decay constant $f_\pi = 93$ MeV and the pion mass $m_\pi = 138$ MeV.

The classical variables $X = \Phi$, Φ^* and σ are determined by the stationary conditions

$$\frac{\partial \Omega}{\partial X} = 0. \tag{1.46}$$

The solutions to the stationary conditions do not give the global minimum of Ω necessarily. They may yield a local minimum or even a maximum. We then have checked that the solutions yield the global minimum when the solutions $X(T, \mu_{\rm u}, \mu_{\rm d})$ are inserted into Eq. (1.44).

1.4.3 Two-flavor EPNJL model

The original PNJL model cannot reproduce LQCD data at imaginary μ quantitatively [100]. This shortcoming seems to be originated in the fact that the correlation between the chiral condensate σ and the Polyakov loop Φ is too weak. In Ref. [101], therefore, we extended the two-flavor PNJL model by introducing the effective four-quark vertex depending on Φ. This effective vertex includes additional mixing effects between σ and Φ. The new model is called the entanglement PNJL (EPNJL) model. The two-flavor EPNJL model reproduces LQCD data at zero and imaginary μ, particularly on strong correlations between the chiral and deconfinement transitions and also on quark-mass dependence of the order of the RW endpoint [128]. The two-flavor EPNJL model reproduces all LQCD data, without changing the parameters, at small real μ without [101] and with strong magnetic field [81] and at finite isospin chemical potential [101].

The four-quark vertex originates from the one-gluon exchange between quarks and

its higher-order diagrams. If the gluon field A_ν has a vacuum expectation value $\langle A_0 \rangle$ in its time component, A_ν is coupled to $\langle A_0 \rangle$ and then to Φ through L. Hence the effective four-quark vertex can depend on Φ [129]. In this thesis, we use the following form for $G(\Phi)$ [101]:

$$G(\Phi) = G_{\rm S}[1 - \alpha_1 \Phi\Phi^* - \alpha_2(\Phi^3 + \Phi^{*3})]. \tag{1.47}$$

This form preserves chiral symmetry, charge conjugation (C) symmetry and extended $\mathbb{Z}_3$ symmetry [97]. We take the parameters $(\alpha_1, \alpha_2) = (0.2, 0.2)$ to reproduce LQCD data at imaginary $\mu_{\rm q}$ [101]. It is expected that Φ dependence of $G(\Phi)$ will be determined in future by the accurate method such as the exact renormalization group method [129–132].

1.4.4 Three-flavor PNJL model

The three-flavor PNJL Lagrangian is obtained in Euclidean spacetime as

$$\begin{aligned}\mathcal{L} = \bar{q}(\gamma_\nu D_\nu + \hat{m}_0 - \gamma_4\hat{\mu})q - G_{\rm S}\sum_{a=0}^{8}[(\bar{q}\lambda_a q)^2 + (\bar{q}i\gamma_5\lambda_a q)^2] \\ + G_{\rm D}\Big[\det_{ij}\bar{q}_i(1-\gamma_5)q_j + \det_{ij}\bar{q}_i(1+\gamma_5)q_j\Big] + \mathcal{U}(\Phi[A], \Phi^*[A], T).\end{aligned} \tag{1.48}$$

The three-flavor quark fields $q = (q_u, q_d, q_s)$ have masses $\hat{m}_0 = {\rm diag}(m_u, m_d, m_s)$, and the chemical potential matrix $\hat{\mu}$ is defined by $\hat{\mu} = {\rm diag}(\mu_u, \mu_d, \mu_s)$. Parameters $G_{\rm S}$ and $G_{\rm D}$ denote coupling constants of the scalar-type four-quark and the KMT determinant interaction, respectively.

Making the mean-field approximation, one can obtain the mean-field Lagrangian as

$$\mathcal{L}_{\rm MF} = \bar{q}(\gamma_\nu D_\nu + M_f - \gamma_4\hat{\mu})q + U_M + \mathcal{U}(\Phi[A], \Phi^*[A], T), \tag{1.49}$$

where

$$M_{\rm u} = m_{\rm u} - 4G_{\rm S}\sigma_{\rm u} + 2G_{\rm D}\sigma_{\rm d}\sigma_{\rm s}, \tag{1.50}$$

$$M_{\rm d} = m_{\rm d} - 4G_{\rm S}\sigma_{\rm d} + 2G_{\rm D}\sigma_{\rm s}\sigma_{\rm u}, \tag{1.51}$$

$$M_{\rm s} = m_{\rm s} - 4G_{\rm S}\sigma_{\rm s} + 2G_{\rm D}\sigma_{\rm u}\sigma_{\rm d} \tag{1.52}$$

m_l(MeV)	m_s(MeV)	Λ(MeV)	$G_{\rm S}\Lambda^2$	$G_{\rm D}\Lambda^5$
5.5	140.7	602.3	1.835	12.36

Table. 1.4 Summary of the parameter set in the 2 + 1 flavor NJL model taken from Ref. [133].

with $\sigma_f \equiv \langle \bar{q}_f q_f \rangle$ and

$$U_M = 2G_{\rm S}(\sigma_{\rm u}^2 + \sigma_{\rm d}^2 + \sigma_{\rm s}^2) - 4G_{\rm D}\sigma_u\sigma_d\sigma_s. \tag{1.53}$$

Performing the path integral over the quark field, one can obtain the thermodynamic potential Ω (per volume) :

$$\begin{aligned}\frac{\Omega}{V} = U_M + \mathcal{U}(\Phi, \Phi^*, T) - 2\sum_{f=u,d,s}\int \frac{d^3\vec{p}}{(2\pi)^3}\Big[N_{\rm c}E_f \\ + \frac{1}{\beta}\ln\ [1 + 3\Phi e^{-\beta(E_f-\mu_f)} + 3\Phi^* e^{-2\beta(E_f-\mu_f)} + e^{-3\beta(E_f-\mu_f)}] \\ + \frac{1}{\beta}\ln\ [1 + 3\Phi^* e^{-\beta(E_f+\mu_f)} + 3\Phi e^{-2\beta(E_f+\mu_f)} + e^{-3\beta(E_f+\mu_f)}]\Big]\end{aligned} \tag{1.54}$$

with $E_f = \sqrt{\vec{p}^{\,2} + M_f^2}$.

The three-dimensional cutoff for the momentum integration is introduced. We assume isospin symmetry for the u-d sector: $m_l \equiv m_u = m_d$. This three-flavor PNJL model has five parameters $G_{\rm S}$, $G_{\rm D}$, m_l, m_s and Λ. A typical parameter set is shown in Table 1.4 [133]. These parameters are fitted to empirical values of pion decay constant and π, K, η' meson masses at vacuum.

1.4.5 Typical behavior of two flavor PNJL model

In this subsection, we overview some results of the 2-flavor PNJL model. Figure 1.2(a) shows T dependence of the order parameters σ and Φ at $\mu_{\rm u} = \mu_{\rm d} = 0$. The solid (dashed) line describes σ (Φ). The σ is normalized by the value $\sigma_0 \equiv \sigma(T = \mu_{\rm u} = \mu_{\rm d} = 0) = -0.0302$ (GeV^3). At lower temperature, $|\sigma|$ is large, whereas Φ is nearly zero. QCD matter is hence in the hadron phase where chiral symmetry is spontaneously broken and quarks are confined. Meanwhile, the fact $\sigma \approx 0$ and $\Phi \neq 0$ at higher temperature means that QCD matter is in the QGP phase where chiral

symmetry is restored and quarks are deconfined. Since the KMT coupling G_2 has a constant value, $U_{\rm A}(1)$ symmetry is broken in both the phases in the PNJL model. One can see this effect in meson spectrum [95, 96].

Since the transitions are crossover, one cannot see any critical behavior and need a prescription to define the pseudo-critical temperature ($T_{\rm c}$). In this thesis, $T_{\rm c}$ is defined by a peak point of susceptibility, and the definition is consistent with LQCD analyses. The susceptibility matrix (χ) is given by

$$\chi = C^{-1} \tag{1.55}$$

with the dimensionless curvature matrix

$$\begin{aligned} C &= \begin{pmatrix} c_{\sigma\sigma} & c_{\sigma\Phi} & c_{\sigma\bar{\Phi}} \\ c_{\Phi\sigma} & c_{\Phi\Phi} & c_{\Phi\bar{\Phi}} \\ c_{\bar{\Phi}\sigma} & c_{\bar{\Phi}\Phi} & c_{\bar{\Phi}\bar{\Phi}} \end{pmatrix} \\ &= \begin{pmatrix} T^2\Omega_{\sigma\sigma} & T^{-1}\Omega_{\sigma\Phi} & T^{-1}\Omega_{\sigma\bar{\Phi}} \\ T^{-1}\Omega_{\Phi\sigma} & T^{-4}\Omega_{\Phi\Phi} & T^{-4}\Omega_{\Phi\bar{\Phi}} \\ T^{-1}\Omega_{\bar{\Phi}\sigma} & T^{-4}\Omega_{\bar{\Phi}\Phi} & T^{-4}\Omega_{\bar{\Phi}\bar{\Phi}} \end{pmatrix} \end{aligned} \tag{1.56}$$

with $\Omega_{xy} = \partial^2\Omega/\partial x\partial y$ for $x, y = \sigma, \pi, \Phi, \bar{\Phi}$ [76].

Figure 1.2(b) shows T dependence of susceptibilities for the order parameters σ and Φ. Here, χ_σ and χ_Φ are shorthand notations of $\chi_{\sigma\sigma}$ and $\chi_{\Phi\Phi^*}$, respectively, and χ_σ is multiplied by 10^{-2}. The chiral and deconfinement transitions have slightly different pseudo-critical temperatures, $T_{\rm c}^\sigma = 212$ MeV and $T_{\rm c}^\Phi = 174$ MeV, in the PNJL model. The $T_{\rm c}$ are inconsistent with the LQCD results quantitatively, but this is improved by EPNJL model [101].

Once the order parameters are determined, the thermodynamic potential (1.44) is fixed. The resultant Ω leads to various thermodynamic quantities. Pressure (P) of the system is obtained by

$$P = -\left(\frac{\Omega}{V} - \frac{\Omega_0}{V}\right), \tag{1.57}$$

where Ω_0 is the thermodynamic potential at $T = \mu = 0$. In the grand canonical ensemble, entropy density (s), number densities (n_f with $f = {\rm u}, {\rm d}$), and energy density

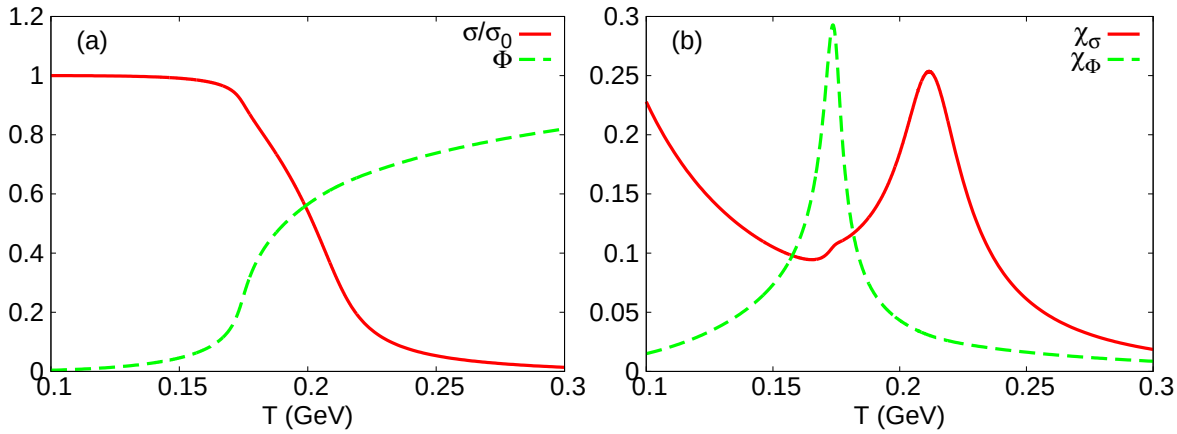

Fig. 1.2 T dependence of order parameter and susceptibility at $\mu_{\rm u} = \mu_{\rm d}$ obtained by the 2-flavor PNJL model. The σ is normalized by $\sigma_0 = -0.0302(\mathrm{GeV}^3)$, and χ_σ is multiplied by 10^{-2}.

(ε) are obtained as

$$s = \frac{\partial P}{\partial T}, \tag{1.58}$$

$$n_f = \frac{\partial P}{\partial \mu_f}, \quad (f = \mathrm{u}, \mathrm{d}), \tag{1.59}$$

$$\varepsilon = -P + Ts + \mu_{\rm u} n_{\rm u} + \mu_{\rm d} n_{\rm d}. \tag{1.60}$$

For later convenience, quark number density $(n_{\rm q})$ and isospin number density $(n_{\rm I})$ are defined as

$$n_{\rm q} = n_{\rm u} + n_{\rm d}, \tag{1.61}$$

$$n_{\rm I} = n_{\rm u} - n_{\rm d}. \tag{1.62}$$

The corresponding chemical potential $\mu_{\rm q}$ and $\mu_{\rm I}$ are then obtained by

$$\mu_{\rm q} = \frac{\mu_{\rm u} + \mu_{\rm d}}{2}, \tag{1.63}$$

$$\mu_{\rm I} = \frac{\mu_{\rm u} - \mu_{\rm d}}{2}, \tag{1.64}$$

which satisfy the thermodynamic relations, $\partial\Omega/\partial\mu_{\rm q} = n_{\rm q}$ and $\partial\Omega/\partial\mu_{\rm I} = n_{\rm I}$. Trace anomaly (Δ) is defined by

$$\Delta = \varepsilon - 3P. \tag{1.65}$$

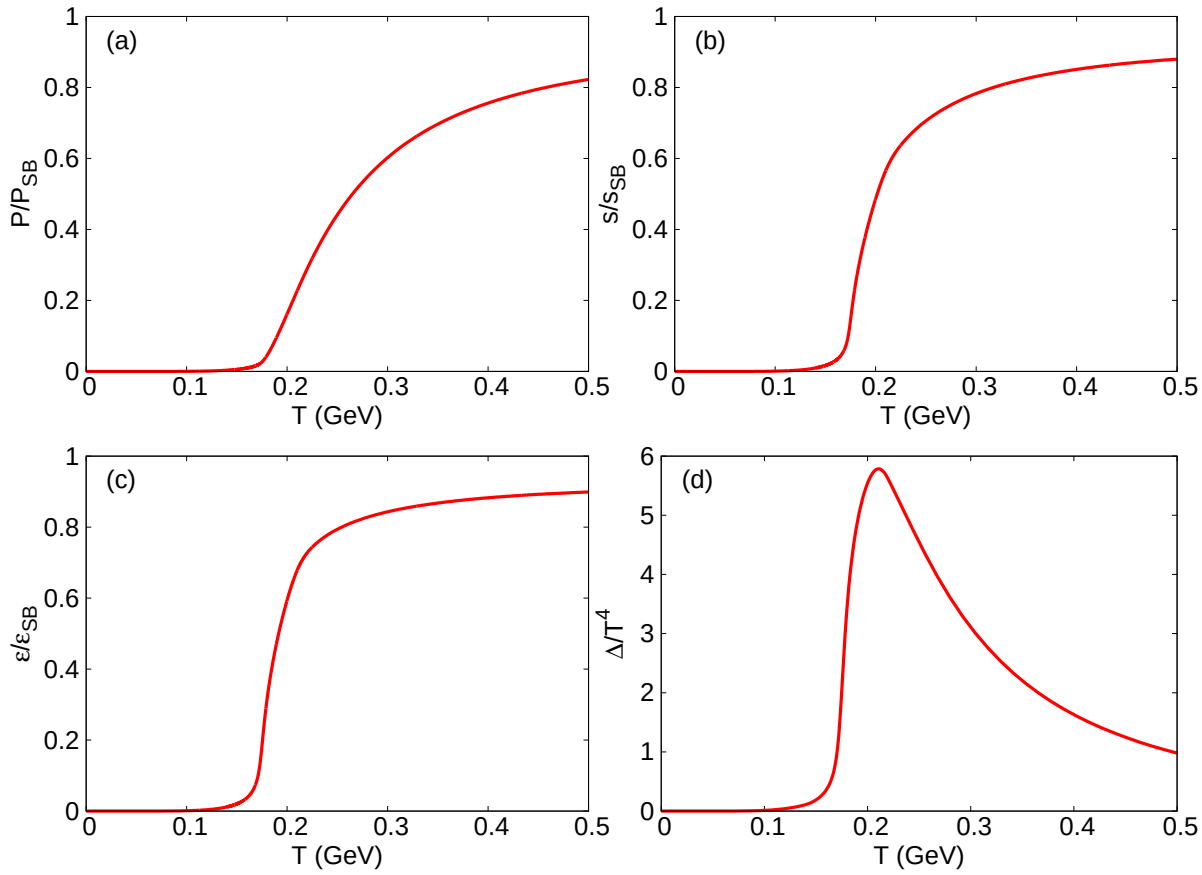

Fig. 1.3 T dependence of P, s, ε, and Δ at $\mu_{\rm u} = \mu_{\rm d} = 0$ obtained by the 2-flavor PNJL model

Figure 1.3 shows T dependence of (a) pressure, (b) entropy density, (c) energy density, and (d) trace anomaly at $\mu_{\rm u} = \mu_{\rm d} = 0$. Note that $n_f = 0$ ($f = {\rm u}, {\rm d}$) there. P, s, and ε are normalized by the values in the Stephan-Boltzmann (SB) limit,

$$P_{\rm SB} = d_{\rm QGP} \frac{\pi^2}{90} T^4 \tag{1.66}$$

at $\mu_{\rm u} = \mu_{\rm d} = 0$, for the degrees of freedom ($d_{\rm QGP}$)

$$d_{\rm QGP} = d_{\rm g} + \frac{7}{8} d_{\rm q} \tag{1.67}$$

with

$$d_{\rm g} = 2_{\rm spin} \times (N_{\rm c}^2 - 1), \tag{1.68}$$

$$d_{\rm q} = 4_{\rm Dirac} \times N_{\rm c} \times N_{\rm f}. \tag{1.69}$$

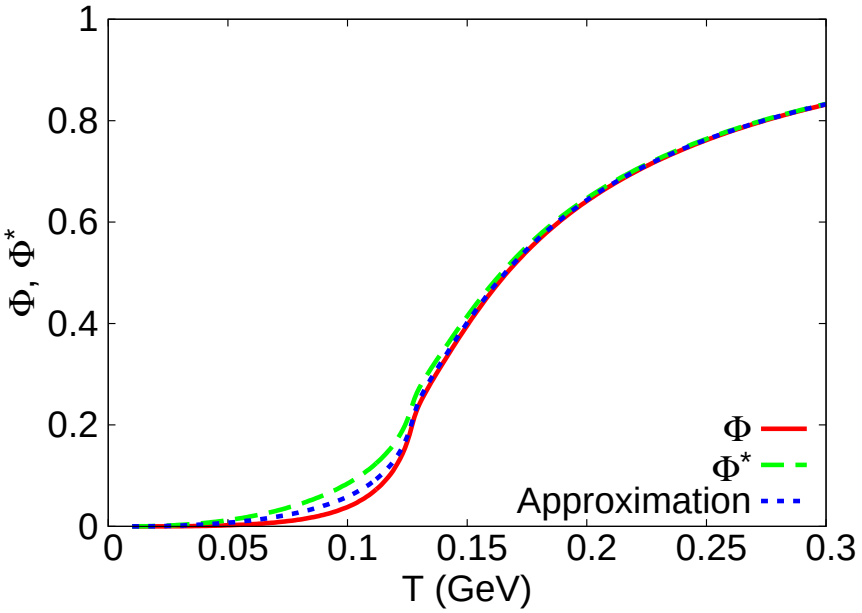

Fig. 1.4 T dependence of the Polyakov loop at $\mu_{\rm q} = 300$ MeV obtained by the 2-flavor PNJL model

For real $\mu_{\rm q}$, Φ^* is not complex conjugate to Φ, but they becomes different real numbers [59]. However one can take the approximation $\Phi = \Phi^*$ [102]. This approximation reduces numerical tasks. Figure 1.4 shows the validity of the approximation for $\mu_{\rm q} = 300$ MeV and $\mu_{\rm I} = 0$. The solid and dashed lines denote Φ and Φ^* before the approximation, respectively, and the dotted line stands for both Φ and Φ^* after the approximation. Even at large chemical potential, the approximation $\Phi = \Phi^*$ thus works well.

Figure 1.5 and 1.6 represent contour plots of σ and Φ in T-$\mu_{\rm q}$ plane at $\mu_{\rm I} = 0$, respectively. One can see smooth crossovers at $\mu_{\rm q} = 0$, but they becomes steep at large $\mu_{\rm q}$. Eventually, they become the first order transitions at $T = 0$. Hence there is a critical endpoint (CEP) of the first order transition.

Figure 1.7 shows the phase diagram of the PNJL model in T-$\mu_{\rm q}$ plane at $\mu_{\rm I}$. The solid line denotes the first-order transition line, while the dashed (dotted) line is the chiral (deconfinement) crossover. The closed circle shows the CEP at $(T, \mu_{\rm q}) = (106\ \text{MeV}, 320\ \text{MeV})$. The first order transition is defined by the discontinuity of the order parameters, σ and Φ.

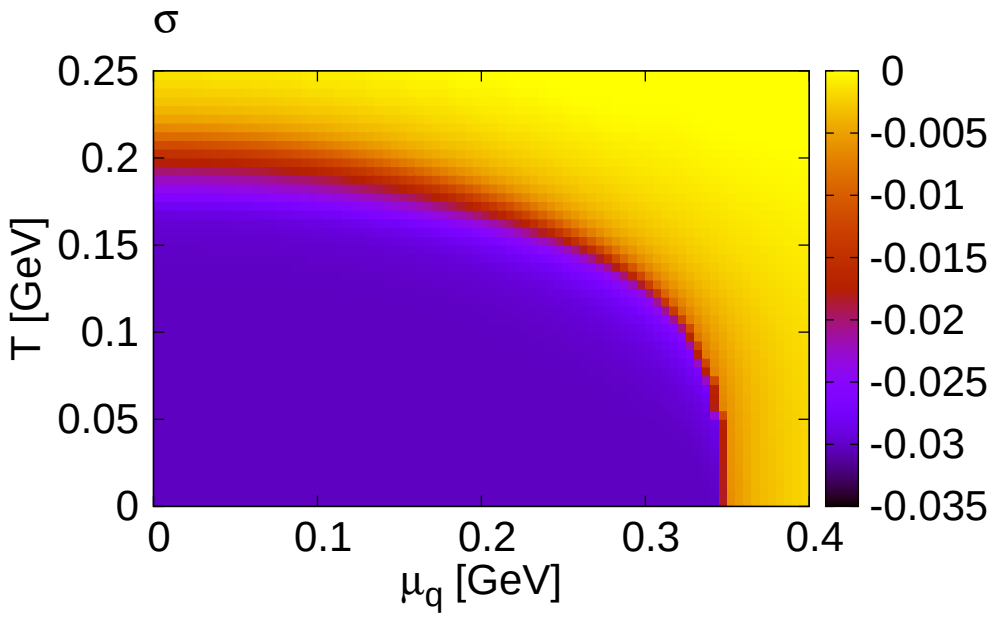

Fig. 1.5 T and $\mu_{\rm q}$ dependence of chiral condensate (σ) obtained by the 2-flavor PNJL model.

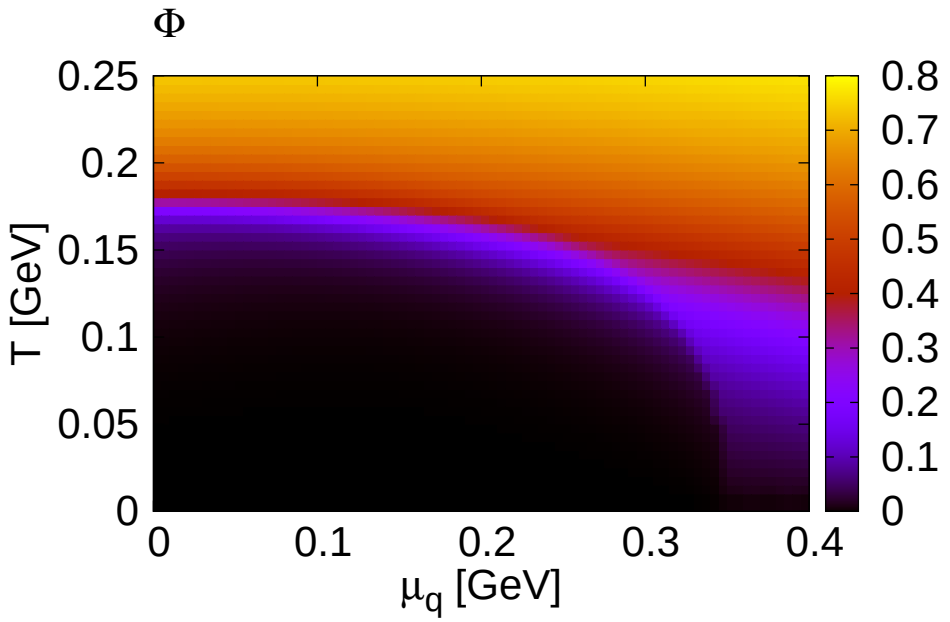

Fig. 1.6 T and $\mu_{\rm q}$ dependence of Polyakov loop (Φ) obtained by the 2-flavor PNJL model.

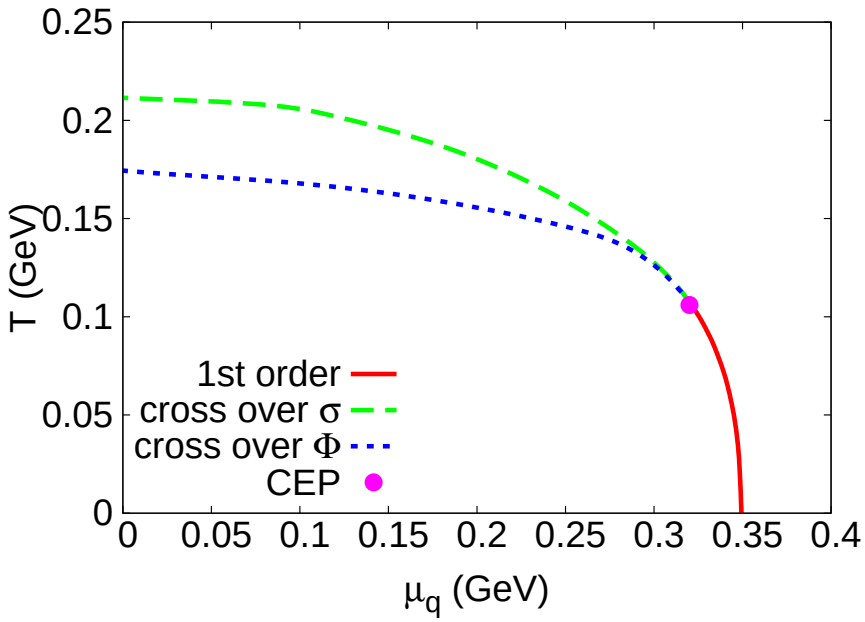

Fig. 1.7 Phase diagram of T-$\mu_{\rm q}$ plane obtained by the 2-flavor PNJL model

1.5 Strategy

Our aim is to understand phase structure of QCD matter for finite T and $\mu_{\rm q}$, that is QCD phase diagram. At present, the phase structure for finite $\mu_{\rm q}$ is almost unknown because first-principle LQCD simulations have the sign problem. Hence, we investigate phase structure with the PNJL model that is one of effective models of low energy QCD and treat confinement and spontaneously breaking of chiral symmetry simultaneously.

Even though LQCD is time consuming and difficult to apply for finite density, it is a only successful and promised method to analyze the QCD phase transition. The mission of the effective model approach is as follows:

(1) Constructing an effective model which can reproduce LQCD data,
(2) Applying the effective model in a broad region and giving a guideline for the future plan of LQCD simulations,
(3) Understanding the regions where LQCD is not feasible.

Theoretically, one can put QCD matter in the presence of external fields to amplify some nonperturbative features of QCD vacuum. If LQCD is applicable, one can observe behaviors of QCD itself. We accomplish the subjects (1), (2), and (3) under such conditions in this thesis.

In chapter 2, we will analyze mass dependence of QCD phase structure for pure-imaginary quark chemical potential, and accomplish the subjects (1) and (2). At finite imaginary chemical potential, $\mathbb{Z}_3$ symmetry as an underlying property of confinement appears as a periodicity of the phase structure. As quark mass varies, the phase transition becomes from crossover to first order. This enables us to describe the phase transition clearly. We will compare the EPNJL and LQCD results to improve reliability of EPNJL model and yield a bird's-eye view analysis for mass dependence of phase transition.

In chapter 3, we will analyze QCD phase transitions at finite θ, and accomplish subjects (2) and (3). The θ parameter can be considered as a external field which

amplify the topological properties of QCD vacuum. Unfortunately, LQCD is not applicable for finite θ because of the sign problem. We first analyze the phase structure for finite θ with the 2 + 1 flavor EPNJL model which is confirmed in Chap.2 to be consistent with LQCD simulations. Finally, we will discuss applicability of LQCD method to finite θ.

LQCD is the most successful method but its reliability is limited for $\mu_{\rm q}/T < 1$ because of the sign problem. Alternatively, neutron star observations can give information on the phase structure for large $\mu_{\rm q}$. In chapter 4, we will analyze QCD phase transition for large $\mu_{\rm q}$ and $T = 0$ by using the observations, and accomplish subjects (1) and (3). We will try to construct the effective model that is consistent with LQCD for $\mu_{\rm q}/T = 0$ and neutron star observation for $\mu_{\rm q}/T = \infty$, and investigate the whole structure of phase diagram including is intermediate $\mu_{\rm q}/T$.

Chapter 2

Quark mass dependence of RW transition

We draw the three-flavor phase diagram as a function of light- and strange-quark masses for both zero and imaginary quark-number chemical potentials using the PNJL and the EPNJL models. The model prediction is qualitatively consistent with 2 + 1 flavor LQCD results at zero chemical potential and with degenerate three-flavor LQCD results at imaginary chemical potential.

2.1 Columbia plot and imaginary chemical potential

2.1.1 Columbia plot

It is important to determine the order of phase transitions appearing in QCD. The result affects the cosmic evolution or the inner core of NSs. The chiral and deconfinement transitions are believed to be crossover at zero chemical potential, when light and strange quark masses, m_l and m_s, have physical values [41]. This crossover nature makes it more difficult to investigate critical behavior and universality of the phase transitions. The order of the transitions is sensitive to the number of flavors,

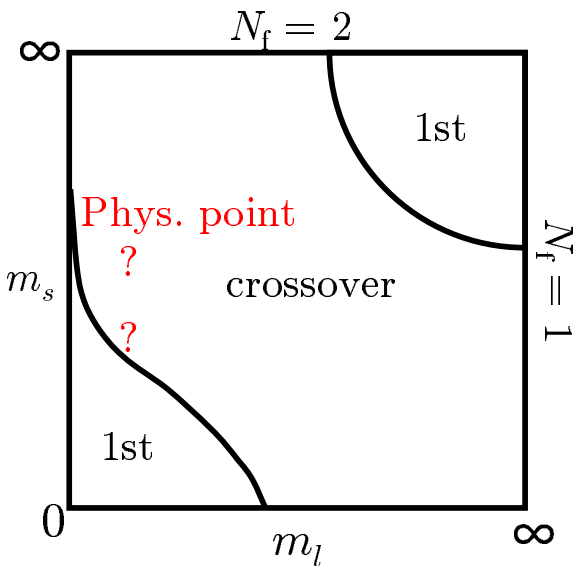

Fig. 2.1 Sketch of the three-flavor phase diagram in the m_l-m_s plane for the chiral transition at $\mu = 0$. The solid line denotes the second-order chiral transition line.

N_f, and the values of m_l and m_s. A sketch of the three-flavor phase diagram is plotted in Fig. 2.1 as a function of m_l and m_s for the case of zero chemical potential (μ) [134], and it is sometimes called the Columbia plot. The physical point lies near the second-order transition line (solid line), where the term "physical point" means that one can reproduce the experimental values of m_π and m_K with this parameter set. In some regions of this plot, one can give clear statement by using exact symmetry and universality class of phase transition.

In the heavy quark limit, i.e. in the pure gauge limit, the system has Z_3 symmetry exactly, and the confinement-deconfinement transition is governed by the symmetry and then described by the order parameter of the symmetry [15]. As a conclusive result in the limit, it is found by LQCD simulations that the transition is the first-order [124, 135–138]. Since the order is rather stable against symmetry-breaking sources such as the quark-mass term, there is the first order transition region at large values of $m_{\rm l}$ and $m_{\rm s}$. The transition becomes crossover at moderate quark masses , and the transition line is investigated by LQCD simulation [139] and the PNJL model [84,86].

In the case of finite quark mass, one can expect that there exists a phase transition governed by chiral symmetry. The chiral transition was investigated by the renormalization group method for massless two-flavor quarks [140–142]. For the case of massless two quarks, i.e. at $(m_l, m_s) = (0, \infty)$, the transition becomes the second order if it belongs to the same universality class as $O(4)$ Heisenberg model and becomes the first order if the $U(1)_{\rm A}$ anomaly is weak around the transition temperature. In Fig. 2.1, we show the second-order case. For massless three-flavor quarks,i.e. at $(m_l, m_s) = (0, 0)$, the renormalization group method shows that the transition should be the first order, because one cannot identify the case with any model having second-order transition. Hence, there is the first-order transition region in the vicinity of the massless three-flavor limit, and the boundary of this region is expected to be the second order. The second order transition line is investigate by LQCD simulations [143], the renormalization group method [140–142], and effective models such as NJL [144–146] and PNJL models [76, 78, 90, 106].

As μ increases from zero, the chiral crossover at the physical point is expected to become the first order. In the case, there appears a critical endpoint (CEP) of the first-order transition line, and the transition becomes the second order on the CEP [127, 147–150]. However, clear evidence of the behavior is not shown yet by LQCD because of the sign problem at real μ. Since current quark masses are not observable, careful attention should be paid for quantitative discussion. In this thesis, we compare the PNJL results with the LQCD ones qualitatively.

2.1.2 QCD with imaginary chemical potential

As shown in Sec. 1.5, LQCD is feasible for pure-imaginary quark chemical potential $\mu_{\rm q} = i\theta_{\rm q} T$, where $\theta_{\rm q}$ represents the dimensionless chemical potential. QCD has a periodicity of $2\pi/3$ in $\theta_{\rm q}$. This is now called the Roberge-Weiss (RW) periodicity [151]. Again, we consider the $\mathbb{Z}_3$ transformation defined in Sec. 1.1.1 for dynamical quarks. The QCD partition function at finite T and $\theta_{\rm q}$ is written by

$$Z(\theta_{\rm q}) = \int \mathcal{D}\bar{q}\mathcal{D}q\mathcal{D}A \ \exp\left[-\int d^4x \left(\bar{q}(\gamma_\mu D_\mu - \hat{m}_0 - i\gamma_4\theta_{\rm q}T)q - \frac{1}{4}F^a_{\mu\nu}F^a_{\mu\nu}\right)\right] \quad (2.1)$$

with the periodic (anti-periodic) boundary condition for gluon (quark) field. Under the $\mathbb{Z}_3$ transformation (1.8),

$$A_\mu \to A'_\mu(x) = V(x)(A_\mu(x) + i\partial_\mu)V^\dagger(x), \tag{2.2}$$

$$V(\tau+\beta,\vec{x}) = z_n V(\tau,\vec{x}), \tag{2.3}$$

$$z_n = e^{i\frac{2\pi}{3}n}, \tag{2.4}$$

the partition function (2.1) becomes

$$Z(\theta_{\rm q}) = \int' \mathcal{D}\bar{q}'\mathcal{D}q' \int \mathcal{D}A' \ \exp\left[-\int d^4x \left(\bar{q}'(\gamma_\mu D_\mu - \hat{m}_0 - i\gamma_4\theta_{\rm q}T)q' - \frac{1}{4}F^a_{\mu\nu}F^a_{\mu\nu}\right)\right]. \tag{2.5}$$

In the functional integral $\int' \mathcal{D}\bar{q}\mathcal{D}q$, the boundary condition for quark fields are not anti-periodic but

$$q'(\tau,\vec{x}) = -z_n^{-1}q'(0,\vec{x}). \tag{2.6}$$

To change this boundary condition, we perform the transformation,

$$q(\tau,\vec{x})' \to q''(\tau,\vec{x}) = (z_n)^{-\tau T}q'(\tau,\vec{x}), \tag{2.7}$$

this changes the partition function (2.5) into

$$\begin{aligned} &Z(\theta_{\rm q}) \\ &= \int \mathcal{D}\bar{q}''\mathcal{D}q''\mathcal{D}A' \ \exp\left[-\int d^4x \left(\bar{q}''(\gamma_\mu D_\mu - \hat{m}_0 - i\gamma_4(\theta_{\rm q} - \frac{2\pi}{3}n)T)q'' - \frac{1}{4}F^a_{\mu\nu}F^a_{\mu\nu}\right)\right] \\ &= Z(\theta_{\rm q} - 2\pi n/3) \end{aligned} \tag{2.8}$$

for $n = 0, 1, 2$. We thus conclude that $Z(\theta_{\rm q})$ is periodic with period $2\pi/3$.

The QCD partition function (2.1) is invariant under the sequential transformations, (2.4) and (2.7), and the shift of

$$\theta_{\rm q} \to \theta'_{\rm q} = \theta_{\rm q} - \frac{2\pi}{3}n, \tag{2.9}$$

This series of transformation are referred as the extended $\mathbb{Z}_3$ transformation [97]. QCD and its effective models should have this extended $\mathbb{Z}_3$ symmetry.

At $\theta = \pi/3 \bmod 2\pi/3$, there appears a first-order transition at T higher than some temperature $T_{\rm RW}$. The transition is now called the RW transition [151]. On the RW

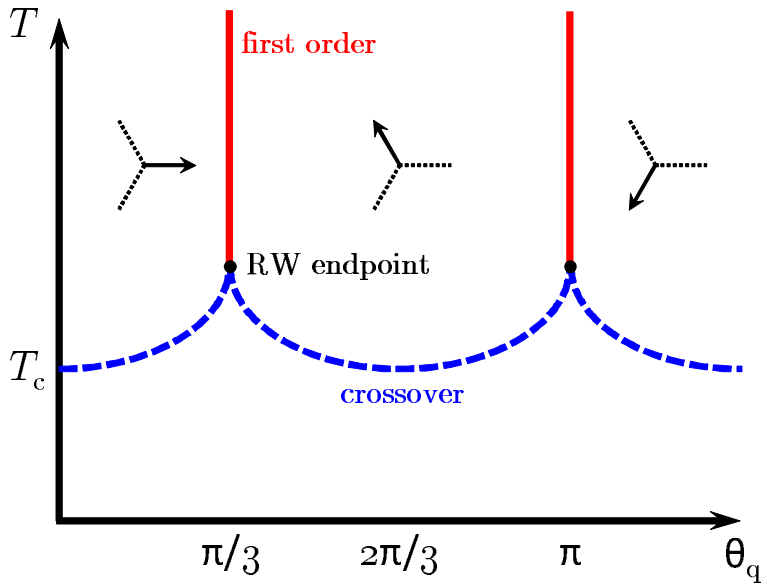

Fig. 2.2 A schematic phase diagram on θ_q-T plane. The solid line denotes the firs-order RW transition line and the dashed line stands for the crossover deconfinement transition line. The arrows indicate the corresponding phases of the Polyakov loop.

transition line starting from the endpoint $(\theta, T) = (\pi, T_{\rm RW})$, the spontaneous breaking of C symmetry occurs [87, 88]. Figure 2.2 shows a schematic phase diagram on θ_q-T plane. The solid line denotes the firs-order RW transition line, and the dashed line corresponds to the crossover deconfinement transition line. On the RW transition line, the Polyakov loop changes the phase, indicating a transition from a $\mathbb{Z}_3$ sector to another sector.

2.1.3 Columbia plot of RW endpoint

Very recently, the order of C symmetry breaking at the RW endpoint was analyzed by two-flavor LQCD simulations [128] and degenerate three-flavor LQCD simulations [152]. For both the cases, the order is the first order at small and large quark masses, but the second order for intermediate masses. Figure 2.3 shows a schematic graph for quark-mass dependence of the phase diagram. For light or heavy quark masses, the

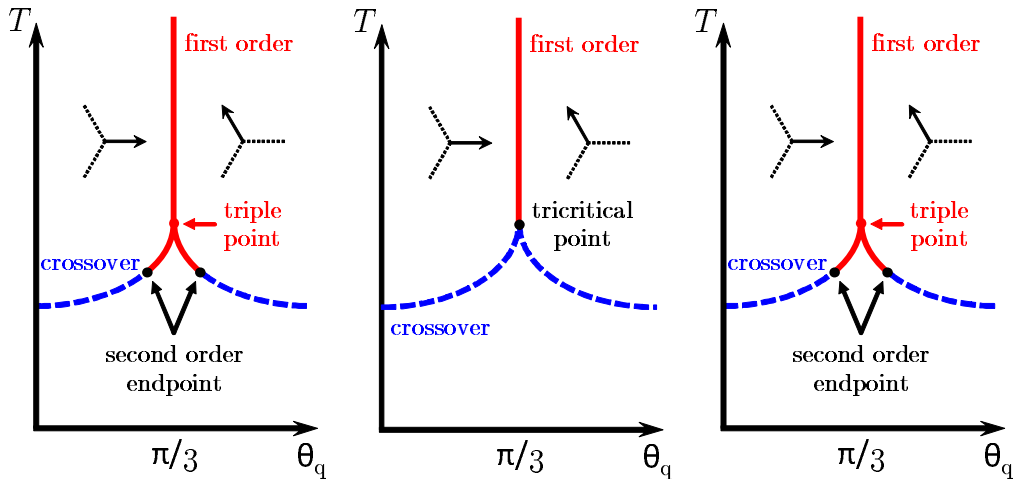

Fig. 2.3 A schematic graph for quark-mass dependence of the phase diagram in $\theta_{\rm q}$-T plane. The solid line denotes the firs-order RW transition line, whereas the dashed line corresponds to the crossover deconfinement transition line. The arrows indicate the corresponding phases of the Polyakov loop.

RW endpoint is a triple point. This means that there is a critical endpoint somewhere in the region $0 < \theta_{\rm q} < \pi/3$, and the crossover at $\theta_{\rm q} = 0$ is changed into the first order above the point. At intermediate quark masses, the RW endpoint is the second order. The deconfinement transition is then always crossover in the region $0 \leq \theta_{\rm q} < \pi/3$, whereas it becomes the second order at $\theta_{\rm q} = \pi/3$. Figure 2.4 is a sketch based on LQCD results for the RW phase transition at the endpoint. Most of the region is unknown at the present stage.

2.2 Model setting

We start with the three-flavor PNJL model mentioned in Sec. 1.4 with imaginary quark chemical potential $\mu_{\rm q} = i\theta_{\rm q}T$,

$$\mathcal{L}_{\rm PNJL} = \bar{q}(\gamma_\nu D_\nu + \hat{m}_0 - i\gamma_4\theta_{\rm q}T)q - G_{\rm S}\sum_{a=0}^{8}\left[(\bar{q}\lambda_a q)^2 + (\bar{q}i\gamma_5\lambda_a q)^2\right]$$
$$+G_{\rm D}\left[\det_{ij}\bar{q}_i(1+\gamma_5)q_j + \det_{ij}\bar{q}_i(1-\gamma_5)q_j\right] - \mathcal{U}(\Phi[A],\bar{\Phi}[A],T), \quad (2.10)$$

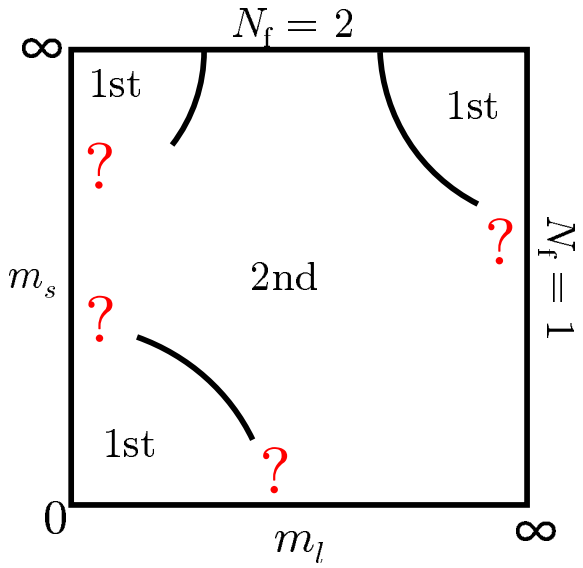

Fig. 2.4 A sketch of the three-flavor phase diagram in the m_l-m_s plane for the RW transition at the endpoint $(T, \theta) = (T_{\rm RW}, \pi/3)$. The solid line means the boundary between the first- and second-order transition regions. The figure is based on two-flavor [128] and degenerate three-flavor [152] LQCD results that the RW transition at the endpoint is the first order for light and heavy quark masses, but the second order for intermediate masses.

where $D^\nu = \partial^\nu + iA^\nu = \partial^\nu + i\delta^\nu_0 g A^0_a \lambda_a/2$ with the gauge coupling g and the Gell-Mann matrices λ_a. Three-flavor quark fields $q = (q_u, q_d, q_s)$ have current quark masses $\hat{m}_0 = \mathrm{diag}(m_u, m_d, m_s)$.

Same as the 2-flavor PNJL model, we introduce the entanglement interaction to the 2+1 flavor PNJL model (2.10),

$$\mathcal{L}_{\rm EPNJL} = \bar{q}(\gamma_\nu D_\nu + \hat{m}_0 - i\gamma_4\theta_{\rm q}T)q - G_{\rm S}(\Phi)\sum_{a=0}^{8}\left[(\bar{q}\lambda_a q)^2 + (\bar{q}i\gamma_5\lambda_a q)^2\right]$$
$$+G_{\rm D}\left[\det_{ij}\bar{q}_i(1+\gamma_5)q_j + \det_{ij}\bar{q}_i(1-\gamma_5)q_j\right] - \mathcal{U}(\Phi[A], \bar{\Phi}[A], T), \quad (2.11)$$
$$G_{\rm S}(\Phi) = G_{\rm S}[1 - \alpha_1\Phi\Phi^* - \alpha_2(\Phi^3 + \Phi^{*3})]. \quad (2.12)$$

In principle, $G_{\rm D}$ can depend on Φ, too. However, we found that Φ-dependence of $G_{\rm D}$ yields qualitatively the same effect on the phase diagram as that of $G_{\rm S}$. As a simple setup, we then neglect Φ-dependence of $G_{\rm D}$. In the present analysis, therefore,

Φ-dependence of $G_{\rm D}$ is renormalized in that of $G_{\rm S}$.

Using the mean field approximation to the quark-quark interactions in (2.11), one can get the thermodynamic potential (per volume):

$$\begin{aligned}\Omega = &\mathcal{U} - 4G_{\rm D}\sigma_{\rm u}\sigma_{\rm d}\sigma_{\rm s} + \sum_{f=u,d,s} 2G_{\rm S}(\Phi)\sigma_f^2 - 2N_{\rm c}\int_\Lambda \frac{d^3\vec{p}}{(2\pi)^3}E_f \\ &+\frac{1}{\beta}\int\frac{d^3\vec{p}}{(2\pi)^3}\Big[\ln[1+3\Phi e^{i\theta_{\rm q}}e^{-\beta E_f}+3\Phi^* e^{2i\theta_{\rm q}}e^{-2\beta E_f}+e^{3i\theta_{\rm q}}e^{-3\beta E_f}] \\ &+\ln[1+3\Phi^* e^{-i\theta_{\rm q}}e^{-\beta E_f}+3\Phi e^{-2i\theta_{\rm q}}e^{-2\beta E_f}+e^{-3i\theta_{\rm q}}e^{-3\beta E_f}]\Big] \end{aligned} \tag{2.13}$$

where $\sigma_f \equiv \langle\bar{q}_f q_f\rangle$ and $E_f \equiv \sqrt{\vec{p}^{\,2}+{M_f}^2}$ for $f = u, d, s$. The dynamical quark mass M_f is defined by

$$M_{\rm u} = m_{\rm u} - 4G_{\rm S}(\Phi)\sigma_{\rm u} + 2G_{\rm D}\sigma_{\rm d}\sigma_{\rm s}, \tag{2.14}$$

$$M_{\rm d} = m_{\rm d} - 4G_{\rm S}(\Phi)\sigma_{\rm d} + 2G_{\rm D}\sigma_{\rm s}\sigma_{\rm u}, \tag{2.15}$$

$$M_{\rm s} = m_{\rm s} - 4G_{\rm S}(\Phi)\sigma_{\rm s} + 2G_{\rm D}\sigma_{\rm u}\sigma_{\rm d}. \tag{2.16}$$

The variables Φ, Φ^*, $\sigma_l(\equiv \sigma_{\rm u} = \sigma_{\rm d})$ and $\sigma_{\rm s}$ are determined by the stationary condition. Although the chemical potential are pure imaginary, one can prove that the thermodynamic potential is real and thermodynamics is well defined. The thermodynamics potential (2.13) can be rewritten into the form that is real explicitly,

$$\begin{aligned}\Omega = &\mathcal{U} - 4G_{\rm D}\sigma_{\rm u}\sigma_{\rm d}\sigma_{\rm s} + \sum_{f=u,d,s} 2G_{\rm S}\sigma_f^2 - 2N_{\rm c}\int_\Lambda \frac{d^3\vec{p}}{(2\pi)^3}E_f \\ &+\frac{1}{\beta}\int\frac{d^3\vec{p}}{(2\pi)^3}\Big[\ln[1+e^{-6\beta E_f}+A(e^{-\beta E_f}+e^{-5\beta E_f}) \\ &+B(e^{-2\beta E_f}+e^{-4\beta E_f})+Ce^{-3\beta E_f}]\Big]\end{aligned} \tag{2.17}$$

with

$$A = 6{\rm Re}(\Phi e^{i\theta_{\rm q}}), \tag{2.18}$$

$$B = 9|\Phi|^2 + 6{\rm Re}(\Phi e^{-2i\theta_{\rm q}}), \tag{2.19}$$

$$C = 2\cos(3\theta_{\rm q}) + 18{\rm Re}(\Phi^2 e^{-i\theta_{\rm q}}). \tag{2.20}$$

The three-flavor PNJL model has five parameters $G_{\rm S}$, $G_{\rm D}$, m_l, m_s and Λ. We use the parameter set of Table 1.4. Parameters of $\mathcal{U}$ are determined to reproduce LQCD data at finite T in the pure gauge limit [94], and they are summarized in Table 1.2. The original value of T_0 is 270 MeV, but the deconfinement temperature T_c determined by the EPNJL model with this value of T_0 is much larger than $T_c \approx 160$ MeV predicted by full LQCD [44, 153–155]. Therefore, we rescale T_0 to 150 MeV so that the EPNJL model can reproduce $T_c = 160$ MeV.

The parameters α_1 and α_2 in (2.12) are so determined as to reproduce two results of LQCD at finite T. The first is a result of 2+1 flavor LQCD at $\mu = 0$ [41] that the chiral transition is crossover at the physical point. The second is a result of degenerate three-flavor LQCD at $\theta_{\rm q} = \pi/3$ [143] that the order of the RW endpoint is first order for small and large quark masses but second-order for intermediate quark masses. The parameter set (α_1, α_2) satisfying these conditions is located in the triangle region

$$\{-1.5\alpha_1 + 0.3 < \alpha_2 < -0.86\alpha_1 + 0.32,\ \alpha_2 > 0\}. \tag{2.21}$$

Here, we take $\alpha_1 = 0.25,\ \alpha_2 = 0.1$ as a typical example.

2.3 Numerical results

Figure 2.5 shows T dependence of light- and strange-quark condensates, σ_l and σ_s, and the Polyakov loop Φ at $\mu_{\rm q} = 0$. In the PNJL model of panel (a), σ_l and σ_s rapidly decrease at $T \approx 180$ MeV as T increases, after Φ rapidly increases at $T \approx 130$ MeV as T increases. Thus, the pseudo-critical temperature of the chiral crossover is much higher than that of the deconfinement crossover. The same property is also seen in the two-flavor case [100]. In the EPNJL model of panel (b), meanwhile, the pseudo-critical temperatures of the chiral and the deconfinement crossover almost coincide at $T \approx 160$ MeV.

Figure 2.6 shows the order of the chiral-transition in the m_l-m_s plane at $\mu = 0$. This figure corresponds to the small m_l and m_s part of Fig.2.1(a). The second-order chiral-transition line is drawn for three cases, the PNJL result (dotted line) and the EPNJL result (solid line) and LQCD data (+ symbols) [143]. For each of the three

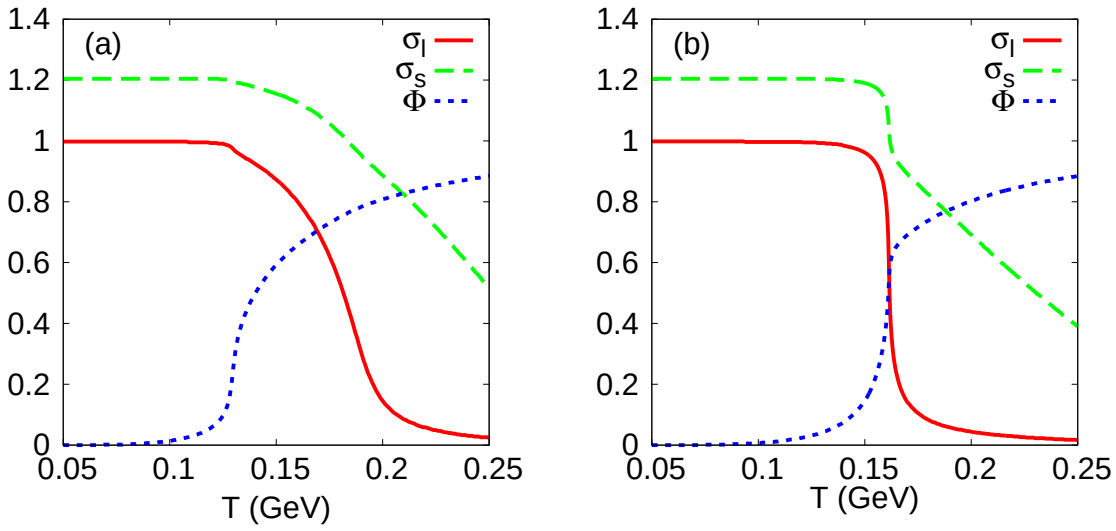

Fig. 2.5 T dependence of the light- and strange-quark condensates and the Polyakov loop at $\mu = 0$. The quark condensates are normalized by $\sigma_l = -0.0142$ [GeV^3] at $T = \mu = 0$. Panels (a) and (b) represent results of the PNJL and EPNJL models, respectively.

cases, there are the first-order region below the second-order line and the crossover region above the line. The second-order line predicted by the EPNJL model is close to that by LQCD data particularly near the physical point. Meanwhile, the first-order region predicted by the PNJL model is much smaller than that by LQCD data. Thus, the EPNJL model yields much better agreement with LQCD prediction than the PNJL model.

The deconfinement transitions predicted by the PNJL and EPNJL models are crossover in the whole region shown in Fig. 2.6. In the EPNJL model, the crossover deconfinement transition almost coincides with the chiral transition, even if the chiral transition is crossover.

Now we consider the C symmetry breaking at $\theta_{\rm q} = \pi/3$ for the case of three degenerate flavors ($m_s = m_l$). Figure 2.7 represents the imaginary part of Ψ as a function of m_l and T predicted by the three-flavor EPNJL model. When m_l is large, the system is close to the pure gauge limit and hence the C-symmetry breaking is first-order. When m_l is small, meanwhile, the system is nearly chirally-symmetric and

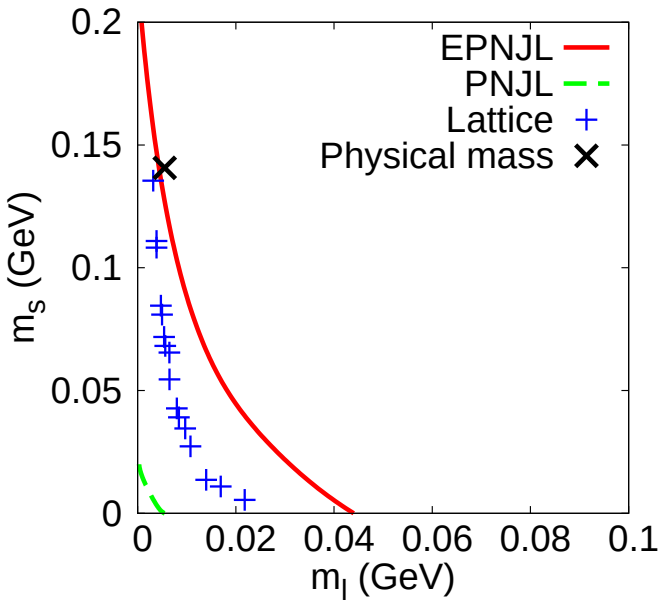

Fig. 2.6 The order of the chiral transition in the m_l-m_s plane at $\mu = 0$. Solid and dotted lines and + symbols represent the second-order chiral-transition lines predicted by the PNJL and EPNJL models and LQCD [143]), respectively.

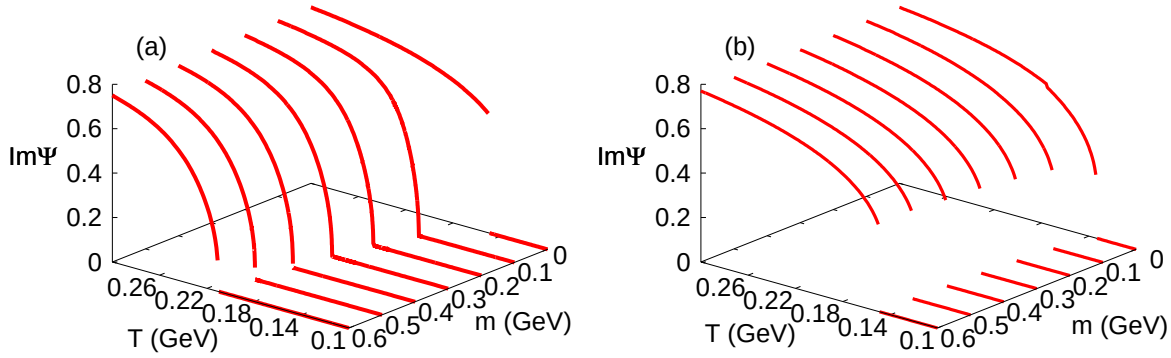

Fig. 2.7 The imaginary part of the modified Polyakov loop at $\theta_q = \pi/3$ in the m_l-T plane predicted by the EPNJL model with $m = m_l = m_s$.

therefore the transition is first-order. In the intermediate mass region, the transition is second order. The result is consistent with the LQCD data [152].

Figure 2.8 shows the phase diagram for the C-symmetry breaking at the RW end-point predicted by the EPNJL model. The diagram is plotted as a function of m_l and m_s up to Λ, the upper limit for the present model to be applicable. The two

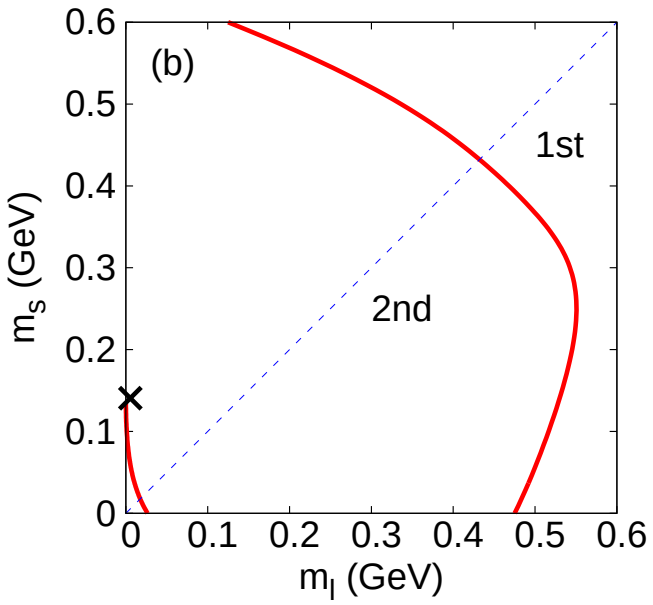

Fig. 2.8 The order of C symmetry breaking at the RW endpoint predicted by the EPNJL model. The transition is first-order below (above) the lower (upper) line, while it is second-order between the two lines. The dotted line stands for a line of $m_l = m_s$, that is, the case of three degenerate flavors, whereas the $\times$ symbol means the physical mass.

solid lines represent boundaries between the first- and second-order transition regions. Below (above) the lower (upper) boundary, the transition is first-order. The dotted line of $m_l = m_s$ corresponds to the case of $N_f = 3$. On the dotted line, the order is first-order for small and large masses but second-order for intermediate masses, as expected. At the physical point, the order is second-order for the present parameter set. However, the order can become first-order at the physical point, if we take other parameter sets belonging to the region (2.21). In the PNJL model, meanwhile, the transition is always first-order in the entire region of the m_l-m_s plane.

In Figs. 2.7 and 2.8, the EPNJL prediction is shown for small and large current quark masses m_q $(q = l, s)$. The applicability of the NJL-type model to large m_q, however, is an open question. In fact it was pointed out that m_q-dependence of the chiral transition temperature is not consistent with the corresponding LQCD results [156, 157]; as m_q increases, the chiral transition temperature goes up sizably in the NJL-type model but hardly changes in the LQCD results. In the EPNJL

model, the chiral transition temperature almost coincides with the deconfinement one that hardly depends on m_q, so that the EPNJL result is consistent with the LQCD result for the transition temperature. It was also pointed out that for large m_q the pion mass m_π calculated with the NJL-type model is larger than the corresponding LQCD result [82]. In the NJL-type model the hadron mass calculation is questionable for large m_q, particularly when the calculated hadron mass is bigger than the cutoff Λ. Therefore, the EPNJL predictions shown in Fig. 2.7 and 2.8 should be regarded as qualitative ones for the $m_q > 100$MeV region where the calculated pion mass is bigger than Λ. However, the fact that there is the second-order region at intermediate m_q (< 100MeV) shows that there exists a boundary between the first- and second-order regions at large m_q. In this qualitative sense, the phase diagram of Fig. 2.8 is reasonable for large m_q.

Figure 2.9 presents the phase diagram in the $\theta_{\rm q}$-T plane predicted by the PNJL and EPNJL models, where m_l and m_s have physical values. In the PNJL model of panel (a), a first-order RW transition (solid) line is connected at the RW endpoint to two first-order deconfinement (dashed) lines. Hence, the RW endpoint is a triple point. In the EPNJL model of panel (b), the RW transition is second-order at the endpoint, so that there is no first-order deconfinement line connected to the first-order RW transition line. For other parameter sets in the parameter region (2.21), the transition is weak first-order at the endpoint and hence the first-order RW transition line is connected at the RW endpoint to two very-short first-order deconfinement lines.

2.4 Short summary

The imaginary chemical potential region and the Columbia plot are good testing grounds to confirm reliability of effective models with comparing its result with that of LQCD. In addition to that, the two regions have important information an realistic QCD. On the Columbia plot, one can give clear statement for exact phase transitions, and realistic crossover transition may be considered as a remnant of it. For finite chemical potential, QCD has remarkable feature called the RW periodicity. Moreover, the canonical partition function of realistic QCD is obtained by the

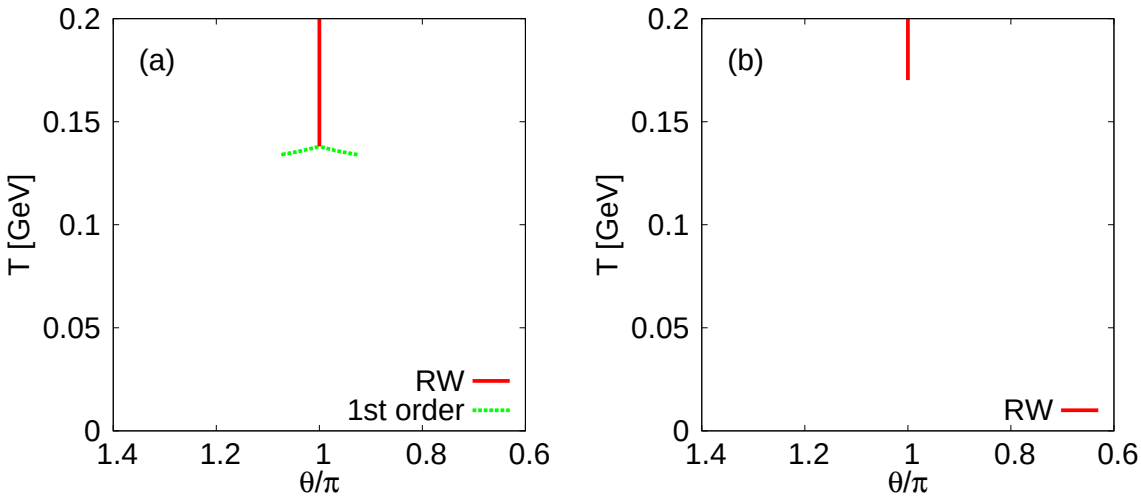

Fig. 2.9 The phase diagram in the θ-T plane predicted by (a) the PNJL model and (b) the EPNJL model. Here, physical values of m_l and m_s are taken. The solid line stands for the first-order RW transition line, while the dashed line corresponds to the first-order deconfinement line.

Fourier transformation of grand canonical partition function for imaginary chemical potential.

We have extended the three-flavor PNJL model by introducing an entanglement vertex $G_{\rm S}(\Phi)$. The entanglement PNJL (EPNJL) model is consistent with 2+1 flavor LQCD data for the chiral transition at $\mu = 0$ and degenerate three-flavor LQCD data for the RW endpoint calculated very lately. The three-flavor phase diagram for the RW endpoint is first drawn in the m_l-m_s plane by the EPNJL model justified above.

Chapter 3

Theta vacuum and QCD phase diagram

We investigate theta-vacuum effects on the QCD phase diagram for the realistic $2+1$ flavor system, using the three-flavor PNJL and EPNJL models. The theta-vacuum effects make the chiral transition sharper. For large theta-vacuum angle the chiral transition becomes first order even if the quark number chemical potential is zero, when the entanglement coupling between the chiral condensate and the Polyakov loop is taken into account. Moreover, we propose a way of circumventing the sign problem on lattice QCD with finite theta, and investigate its availability. We consider the reweighting method for the QCD Lagrangian after the $U(1)_{\rm A}$ transformation. In the Lagrangian, the P-odd mass term as a cause of the sign problem is minimized. In order to find a good reference system in the reweighting method, we estimate the average reweighting factor by using the two-flavor PNJL model and eventually find a good reference system.

3.1 Introduction: Theta vacuum and its appearance

For T higher than the QCD scale Λ_{QCD}, there is a possibility that θ is effectively varied to finite values depending on spacetime coordinates (t, x), since sphalerons are so activated as to jump over the potential barrier between the different degenerate ground states [158]. If this happens, P and CP symmetries can be violated locally in high-energy heavy-ion collisions or the early universe at $T \approx \Lambda_{QCD}$. Actually, it is argued in Refs. [159–161] that θ may be of order one at the epoch of the QCD phase transition in the early universe, whereas it vanishes at the present epoch [162–166]. This finite value of θ could be a new source of large CP violation in the early universe and may be a crucial missing element for solving the puzzle of baryogenesis.

In the early stage of heavy-ion collision, the magnetic field is formed, while the effective $\theta(t, x)$ deviates the total number of particles plus antiparticles with right-handed helicity from those with left-handed helicity. As a consequence of this fact, an electromagnetic current is generated along the magnetic field, since particles with right-handed helicity move opposite to antiparticles with right-handed helicity. This is the so-called chiral magnetic effect [77, 79, 159, 167]. The chiral magnetic effect may explain the charge separations observed in the recent STAR results [168, 169]. The thermal system with nonzero θ is thus quite interesting.

For vacuum with no temperature (T) and no quark-number chemical potential (μ), parity P is preserved when $\theta = 0$ [170], but is spontaneously broken when $\theta = \pi$ [171,172]. The P violation, called the Dashen mechanism, is essentially nonperturbative, but the first-principle lattice QCD (LQCD) is not applicable for the case of finite θ because of the sign problem. Temperature (T) and/or quark-number chemical potential (μ) dependence of the mechanism has then been analyzed by effective models such as the chiral perturbation theory [160,173–177], the Nambu-Jona-Lasinio (NJL) model [178–181] and the Polyakov-loop extended Nambu-Jona-Lasinio (PNJL) model [88, 104].

Using the two-flavor NJL model [117, 118, 127, 147, 150], Fujihara, Inagaki and Kimura made a pioneering work on the P violation at $\theta = \pi$ [181] and Boer and

Boomsma studied this issue extensively [178,179]. In the previous works [88,104], we extended the formalism to the two-flavor PNJL and EPNJL models and investigated effects of the theta vacuum on the QCD phase diagram. Very recently similar analyses were made for the realistic case of 2+1 flavors by using the NJL model [180]. It is then highly expected that the finite-θ effect is investigated in the 2+1 flavor case by using the PNJL and EPNJL models that are more reliable than the NJL model.

In this chapter, we investigate the QCD phase structure for finite θ. In Secs. 3.2 and 3.3, the phase structure is investigated by the realistic 2 + 1 flavor PNJL and EPNJL models discussed in Chap. 2. In Secs. 3.4 and 3.5, we propose a reweighting method for LQCD simulations with finite θ and analyze its availability by calculating the average reweighting factor with the 2-flavor PNJL model. Section 3.5 is devoted to short summary.

3.2 Model setting

The three-flavor PNJL Lagrangian with the θ-dependent anomaly term is obtained in Euclidean spacetime by

$$\begin{aligned}\mathcal{L} = &\bar{q}(\gamma_\nu D_\nu + \hat{m}_0 - \gamma_4\hat{\mu})q - G_{\rm S}(\Phi)\sum_{a=0}^{8}[(\bar{q}\lambda_a q)^2 + (\bar{q}i\gamma_5\lambda_a q)^2] \\ &+G_{\rm D}\left[e^{i\theta}\det_{ij}\bar{q}_i(1-\gamma_5)q_j + e^{-i\theta}\det_{ij}\bar{q}_i(1+\gamma_5)q_j\right] + \mathcal{U}(\Phi[A],\Phi^*[A],T). \quad (3.1)\end{aligned}$$

Since the θ parameter is related to the $U_{\rm A}(1)$ anomaly, it appears in the KMT determinant interaction [182]. With the chiral transformation,

$$q_l = q'_l e^{i\gamma_5(\theta/4)}q_l,, \quad (3.2)$$

$$q_{\rm s} = q'_{\rm s}, \quad (3.3)$$

for $l = {\rm u}, {\rm d}$, Lagrangian (3.1) can be rewritten into

$$\begin{aligned}\mathcal{L} = &\bar{q}'(\gamma_\nu D_\nu + \hat{m}_{0+} + i\hat{m}_{0-}\gamma_5 - \gamma_4\hat{\mu})q' - G_{\rm S}\sum_{a=0}^{8}[(\bar{q}'\lambda_a q')^2 + (\bar{q}'i\gamma_5\lambda_a q')^2] \\ &+G_{\rm D}\left[\det_{ij}\bar{q}'_i(1-\gamma_5)q'_j + \det_{ij}\bar{q}'_i(1+\gamma_5)q'_j\right] + \mathcal{U}(\Phi[A],\Phi^*[A],T) \quad (3.4)\end{aligned}$$

with

$$\begin{aligned}\hat{m}_{0+} &= \mathrm{diag}(m_{u+}, m_{d+}, m_{s+}) \\ &= \mathrm{diag}\left(\cos\left(\tfrac{\theta}{2}\right)m_u,\ \cos\left(\tfrac{\theta}{2}\right)m_d,\ m_s\right), \qquad (3.5)\\ \hat{m}_{0-} &= \mathrm{diag}(m_{u-}, m_{d-}, m_{s-}) \\ &= \mathrm{diag}\left(\sin\left(\tfrac{\theta}{2}\right)m_u,\ \sin\left(\tfrac{\theta}{2}\right)m_d,\ 0\right). \qquad (3.6)\end{aligned}$$

In this form, θ dependence does not appear in the determinant interaction, but appears in the mass term.

The present three-flavor PNJL model has eighteen scalar and pseudoscalar condensates of quark-antiquark pair, but flavor off-diagonal condensates vanish for the system with flavor symmetric chemical potentials only [88, 104, 178, 179]. Since the quark-number chemical potential considered in this thesis is flavor-diagonal, we can concentrate our discussion on flavor-diagonal condensates. Under the chiral transformation (3.2) and (3.3), the flavor-diagonal quark-antiquark condensates, $\sigma_f \equiv \langle \bar{q}_f q_f \rangle$ and $\eta_f \equiv \langle \bar{q}_f i\gamma_5 q_f \rangle$, are transformed into $\sigma'_f = \langle \bar{q}'_f q'_f \rangle$ and $\eta'_f \equiv \langle \bar{q}'_f i\gamma_5 q'_f \rangle$ as

$$\sigma_l = \cos\left(\tfrac{\theta}{2}\right)\sigma'_l + \sin\left(\tfrac{\theta}{2}\right)\eta'_l, \qquad (3.7)$$

$$\eta_l = -\sin\left(\tfrac{\theta}{2}\right)\sigma'_l + \cos\left(\tfrac{\theta}{2}\right)\eta'_l, \qquad (3.8)$$

$$\sigma_{\mathrm{s}} = \sigma'_{\mathrm{s}}, \qquad (3.9)$$

$$\eta_{\mathrm{s}} = \eta'_{\mathrm{s}}. \qquad (3.10)$$

Making the mean-field approximation, one can obtain the mean-field Lagrangian as

$$\mathcal{L}_{\mathrm{MF}} = \bar{q}'(\gamma_\nu D_\nu + M'_f + i\gamma_5 N'_f - \gamma_4\hat{\mu})q' + U_M + \mathcal{U}(\Phi[A], \Phi^*[A], T), \qquad (3.11)$$

where

$$M'_{\rm u} = m_{\rm u+} - 4G_{\rm S}\sigma'_{\rm u} + 2G_{\rm D}(\sigma'_{\rm d}\sigma'_{\rm s} - \eta'_{\rm d}\eta'_{\rm s}), \tag{3.12}$$

$$M'_{\rm d} = m_{\rm d+} - 4G_{\rm S}\sigma'_{\rm d} + 2G_{\rm D}(\sigma'_{\rm s}\sigma'_{\rm u} - \eta'_{\rm s}\eta'_{\rm u}), \tag{3.13}$$

$$M'_{\rm s} = m_{\rm s+} - 4G_{\rm S}\sigma'_{\rm s} + 2G_{\rm D}(\sigma'_{\rm u}\sigma'_{\rm d} - \eta'_{\rm u}\eta'_{\rm d}), \tag{3.14}$$

$$N'_{\rm u} = m_{\rm u-} - 4G_{\rm S}\eta'_{\rm u} - 2G_{\rm D}(\sigma'_{\rm d}\eta'_{\rm s} + \eta'_{\rm d}\sigma'_{\rm s}), \tag{3.15}$$

$$N'_{\rm d} = m_{\rm d-} - 4G_{\rm S}\eta'_{\rm d} - 2G_{\rm D}(\sigma'_{\rm s}\eta'_{\rm u} + \eta'_{\rm s}\sigma'_{\rm u}), \tag{3.16}$$

$$N'_{\rm s} = m_{\rm s-} - 4G_{\rm S}\eta'_{\rm s} - 2G_{\rm D}(\sigma'_{\rm u}\eta'_{\rm d} + \eta'_{\rm u}\sigma'_{\rm d}), \tag{3.17}$$

and

$$U_M = 2G_{\rm S}\sum_{f=u,d,s}({\sigma'_f}^2 + {\eta'_f}^2) - 4G_{\rm D}\sigma'_u\sigma'_d\sigma'_s + 4G_{\rm D}(\sigma'_u\eta'_d\eta'_s + \eta'_u\sigma'_d\eta'_s + \eta'_u\eta'_d\sigma'_s). \tag{3.18}$$

Performing the path integral over the quark field, one can obtain the thermodynamic potential Ω (per volume) for finite T and $\mu_{\rm q}$:

$$\begin{aligned}\Omega = U_M + \mathcal{U}(\Phi, \Phi^*, T) - 2N_{\rm c}\sum_{f=u,d,s}\int_\Lambda \frac{d^3\vec{p}}{(2\pi)^3}E_f \\ -2\sum_{f=u,d,s}\int\frac{d^3\vec{p}}{(2\pi)^3}\Big[\frac{1}{\beta}\ln\ [1 + 3\Phi e^{-\beta(E_f-\mu)} + 3\Phi^* e^{-2\beta(E_f-\mu)} + e^{-3\beta(E_f-\mu)}] \\ +\frac{1}{\beta}\ln\ [1 + 3\Phi^* e^{-\beta(E_f+\mu)} + 3\Phi e^{-2\beta(E_f+\mu)} + e^{-3\beta(E_f+\mu)}]\Big]\end{aligned} \tag{3.19}$$

with $E_f = \sqrt{\vec{p}^{\,2} + {M'_f}^2 + {N'_f}^2}$.

3.3 Numerical results

In this section we show numerical results for the original condensates (σ_f, η_f, Φ), since this makes our discussion transparent. Under the parity transformation, σ_f, η_f and Φ are transformed into σ_f, $-\eta_f$ and Φ, respectively. This means that η_f is θ-odd while σ_f and Φ are θ-even, since the Lagrangian is invariant under the combination of the parity transformation and the transformation $\theta \to -\theta$. Thus η_f is an order parameter of the spontaneous parity breaking, while σ_f and Φ are approximate order parameters of the chiral and the deconfinement transitions, respectively. As an approximate order parameter of the chiral transition, σ_l is more proper than σ_s since $m_l \ll m_s$.

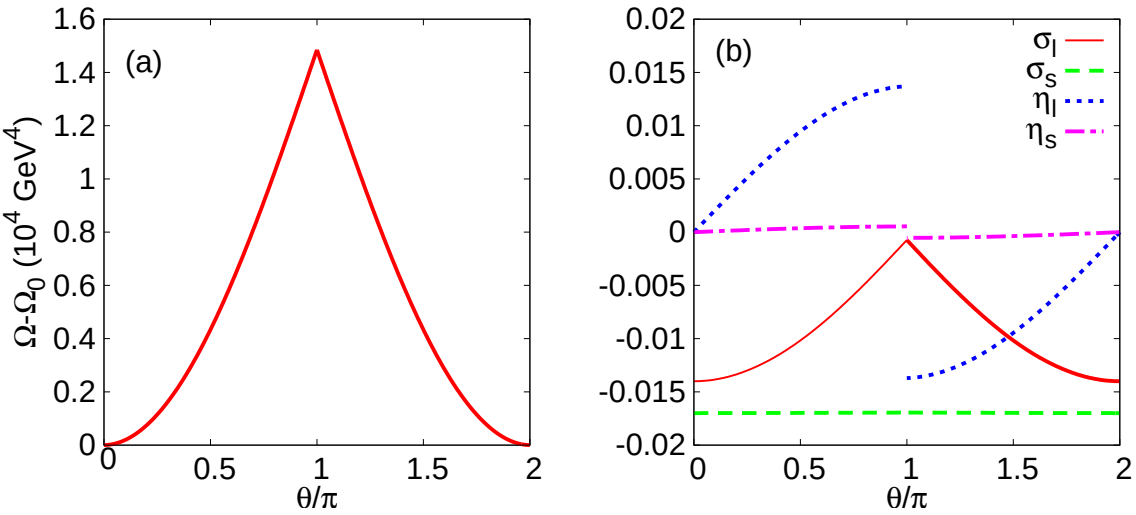

Fig. 3.1 θ dependence of (a) Ω and (b) the order parameters at $T = \mu_{\rm q} = 0$ in the EPNJL model. In panel (a), $\Omega_0 \equiv \Omega(\theta = 0)$ is subtracted from Ω. See the legend for the definition of lines.

3.3.1 Thermodynamics at $\mu_{\rm q} = 0$

In this subsection, we consider the case of $\mu_{\rm q} = 0$ where charge conjugation symmetry (C) is exact. Meanwhile, parity symmetry (P) is exact only at $\theta = 0, \ \pm\pi$, since $e^{i\theta}$ agrees with $e^{-i\theta}$ in (3.1) when $\theta = 0, \ \pm\pi$.

Figure 3.1 shows θ dependence of Ω and the order parameters at $T = \mu_{\rm q} = 0$ in the EPNJL model; note that the EPNJL model agrees with the PNJL model at $T = 0$, since $G_{\rm S}(\Phi) = G_{\rm S}$ there because of $\Phi = 0$. As shown in panel (a), Ω is θ-even and has a cusp at $\theta = \pi$. This indicates that a first-order phase transition takes place at $T = \mu_{\rm q} = 0$ and $\theta = \pi$. As shown in panel (b), meanwhile, the η_f are θ-odd, while σ_f and Φ are θ-even. The condensate η_l and η_s have jumps at $\theta = \pi$, indicating that the first-order transition mentioned above is the spontaneous parity breaking. This is nothing but the Dashen phenomena [171].

Figure 3.2 shows θ dependence of the order parameters and the effective quark mass $\Pi_f \equiv \sqrt{M_f'^2 + N_f'^2}$ at $T = 163$ MeV and $\mu_{\rm q} = 0$ in the EPNJL model. For this higher temperature, the Dashen phenomena do not take place at $\theta = \pi$. Actually η_l and η_s

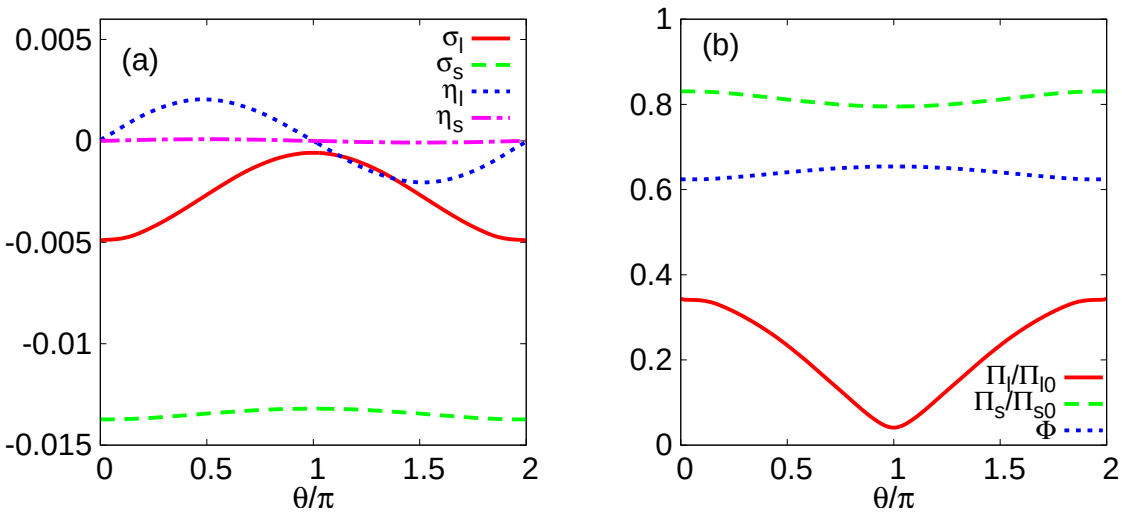

Fig. 3.2 θ dependence of (a) the order parameters and (b) the effective quark mass Π_f at $T = 163$ MeV and $\mu_{\rm q} = 0$ in the EPNJL model. In panel (b), Π_f is normalized by the value at $T = \mu = \theta = 0$ and the normalized Π_f is compared with the Polyakov loop Φ. See the legend for the definition of lines.

vanish there, although they become finite at $\theta \neq 0,\ \pi,\ 2\pi$ where P is not an exact symmetry. The other order parameters, σ_f and Φ, are smooth periodic functions of θ. The Polyakov loop Φ becomes maximum at $\theta = \pi$, since the effective quark mass Π_f becomes minimum and the thermal factor $\exp(-\beta E_f)$ is maximized in (3.19).

Figure 3.3 shows T dependence of the order parameters at $\theta = \pi$ and $\mu_{\rm q} = 0$. Comparing this figure with Fig. 2.5, one can also see θ dependence of the order parameters. In the PNJL model of panel (a), $|\eta_l|$ and $|\eta_s|$ are finite below the critical temperature $T_P = 194$ MeV and vanish above T_P. Thus the P symmetry is broken at smaller T, but restored at higher T. In the two-flavor PNJL model, this P restoration is second order [104]. This is the case also for the present 2+1 flavor PNJL model. The second order P restoration induces cusps in $|\sigma_l|$ and $|\sigma_s|$ when $T = T_P$, although the cusp is weak in $|\sigma_s|$. This propagation of the cusp can be understood by the extended discontinuity theorem of Ref. [83]. In the EPNJL model of panel (b), the P restoration occurs at $T_P = 158$ MeV as the first-order transition. The same property is seen in the two-flavor EPNJL model [104]. The first-order P restoration generates gaps in $|\sigma_l|$ and $|\sigma_s|$ when $T = T_P$, although the gap is tiny in $|\sigma_s|$. This propagation

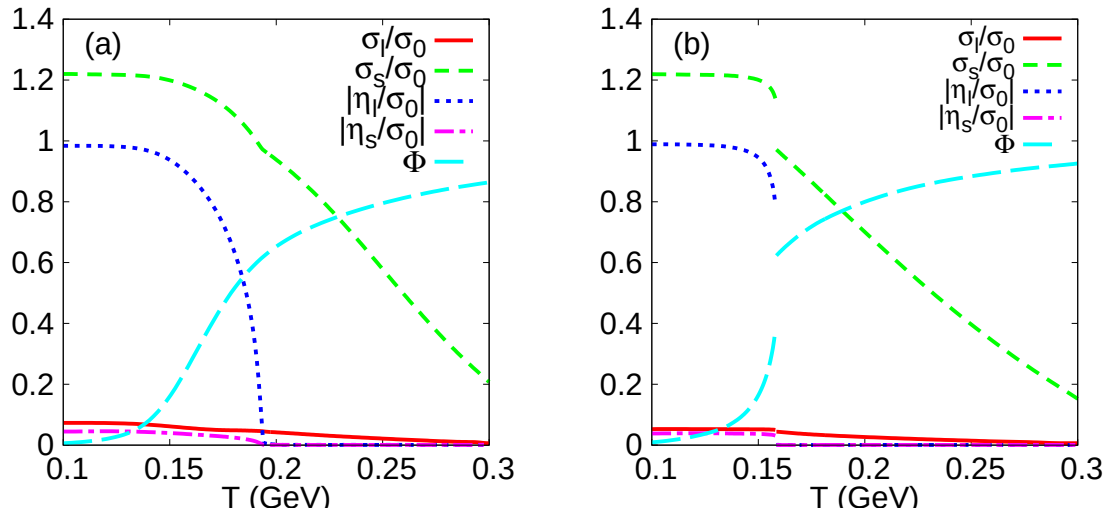

Fig. 3.3 T dependence of the order parameters at $\theta = \pi$ and $\mu_q = 0$ in (a) the PNJL model and (b) the EPNJL model. See the legend for the definition of lines.

Model	$\theta = 0$	$\theta = \pi$
NJL	177 (crossover)	170 (2nd order)
PNJL	200 (crossover)	194 (2nd order)
EPNJL	162 (crossover)	158 (1st order)

Table. 3.1 Theoretical prediction on the critical temperature of the chiral transition at $\theta = 0$ and $\mu_q = 0$ and the P restoration at $\theta = \pi$ and $\mu_q = 0$. The values are shown in units of MeV.

of the gap can be understood by the discontinuity theorem by Barducci, Casalbuoni, Pettini and Gatto [183]. Thus the Dashen phenomena are seen only at lower T, and the order of the P violation at the critical temperature T_P depends on the effective model taken.

Theoretical prediction on the critical temperature of the chiral transition at $\theta = 0$ and $\mu_q = 0$ and the P restoration at $\theta = \pi$ and $\mu_q = 0$ is tabulated in Table 3.1. At $\theta = 0$, the chiral transition is crossover in all of the NJL, PNJL, and EPNJL models At $\theta = \pi$, the order of the P restoration is first order in the EPNJL model, but it is second order in the PNJL and NJL models.

Figure 3.4 shows θ dependence of transition temperatures at $\mu_q = 0$. The dashed

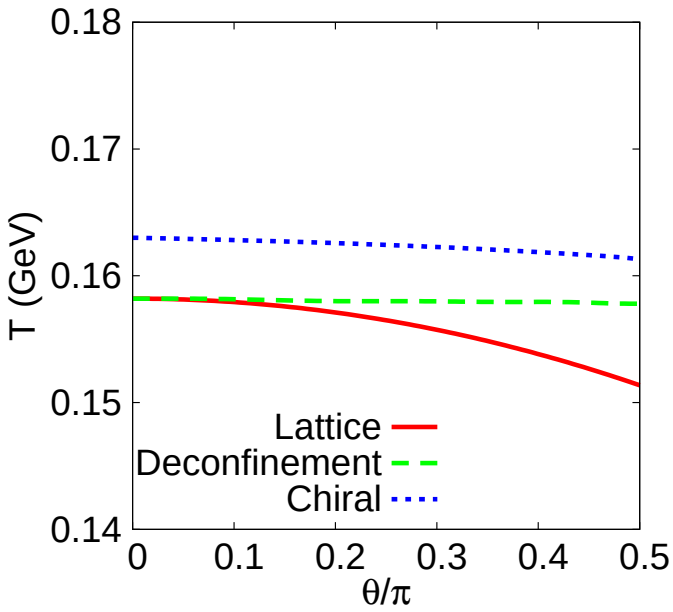

Fig. 3.4 θ dependence of the critical temperature at $\mu_{\rm q} = 0$ calculated by EPNJL model and pure-gauge LQCD simulation [184].

and dotted lines show EPNJL model results for the deconfinement and the chiral transition temperature, respectively. Solid line shows a result of lattice simulations [184]:

$$\frac{T_{\rm c}(\theta)}{T_c(0)} = 1 - R_\theta \theta^2 + O(\theta^4), \tag{3.20}$$

$$R_\theta = 0.0175(7). \tag{3.21}$$

The coefficient R_θ has been determined from lattice simulations of pure Yang-Mills theory with imaginary θ parameter, and the constant $T_{\rm c}(0)$ is fixed to that of the EPNJL model. Compared with the lattice result, the model result has weaker θ dependence . This result shows that lattice simulations with dynamical quarks are crucial to investigate theta vacuum effects.

3.3.2 Thermodynamics at $\mu_{\rm q} > 0$

In this subsection, we consider the case of $\mu_{\rm q} > 0$ where C symmetry is not exact. In general, the relation $\Phi = \Phi^*$ is not satisfied for finite $\mu_{\rm q}$, although Φ and Φ^* are real [59]. This situation makes numerical calculations quite time-consuming. How-

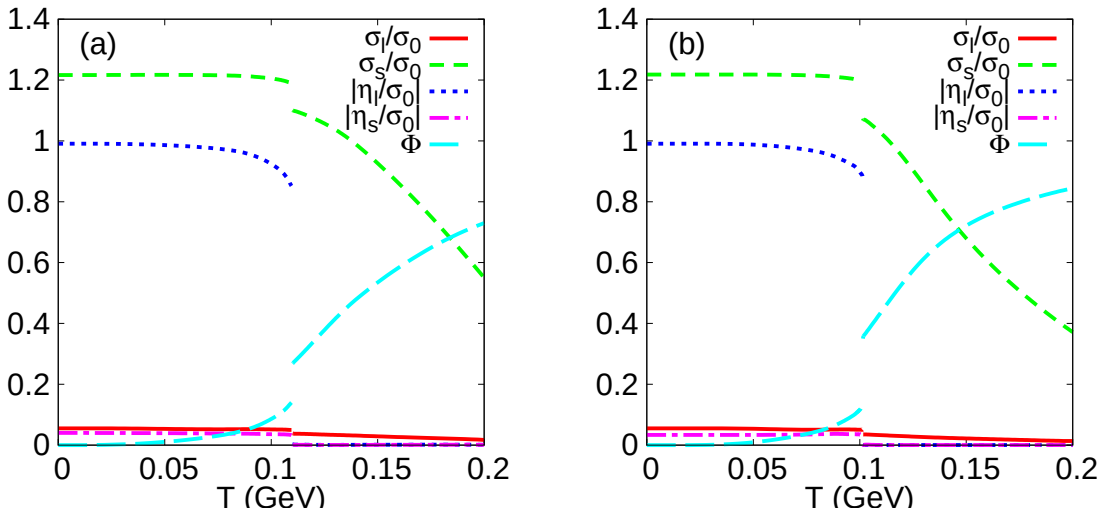

Fig. 3.5 T dependence of the order parameters at $\theta = \pi$ and $\mu_{\rm q} = 300$ MeV in (a) the PNJL model and (b) the EPNJL model. See the legend for the definition of lines.

ever, the deviation $\Phi - \Phi^*$ is known to be very small [102]. For this reason, the assumption $\Phi = \Phi^*$ has been used in many papers. Therefore we use the assumption also in this thesis.

Figure 3.5 represents T dependence of the order parameters at $\theta = \pi$ and $\mu_{\rm q} = 300$ MeV in the PNJL and EPNJL models. The P restoration takes place at high T, since η_l and η_s are zero there. The critical temperature of the P restoration is $T_P = 110$ MeV for the PNJL model and $T_P = 99$ MeV for the EPNJL model. For $\mu_{\rm q} = 300$ MeV, the order of the P restoration at $T = T_P$ is first order in both the PNJL and EPNJL models. Thus the quark-number chemical potential $\mu_{\rm q}$ lowers T_P and makes the P restoration sharper.

Figure 3.6 shows the phase diagram of the chiral transition in the $\mu_{\rm q}$-θ-T space. The diagram is mirror symmetric with respect to the $\mu_{\rm q}$-T plane at $\theta = 0$, so the diagram is plotted only at $\theta \geq 0$. Panels (a) and (b) correspond to results of the PNJL and EPNJL models, respectively. In the $\mu_{\rm q}$-T plane at $0 \leq \theta < \pi$, the solid line stands for the first-order chiral transition, while the dashed line represents the chiral crossover. The meeting point between the solid and dashed lines is a critical endpoint (CEP) of second order. Point C is a CEP in the $\mu_{\rm q}$-T plane at $\theta = 0$ [147–149]. For both the

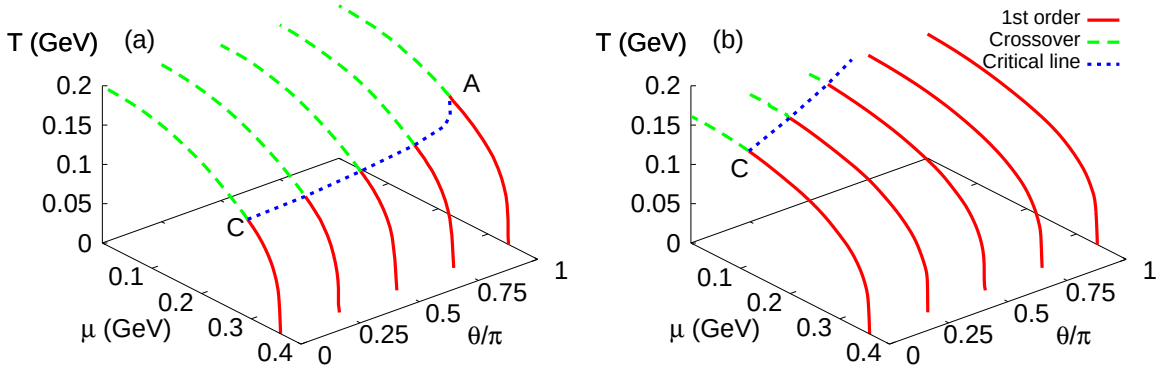

Fig. 3.6 Phase diagram of the chiral transition in the μ_q-θ-T space. Panel (a) shows a result of the PNJL model and panel (b) corresponds to a result of the EPNJL model.

PNJL and EPNJL models, the location of CEP in the μ_q-T plane moves to higher T and lower μ_q as θ increases from 0 to π.

In the μ_q-T plane at $\theta = \pi$, P symmetry is exact and hence we can consider the spontaneous breaking of P symmetry in addition to the chiral transition. For the PNJL model of panel (a), both the first-order chiral transition and the first-order P restoration take place simultaneously, and the second-order P restoration and the chiral crossover coincide with each other. The first-order and the second-order P transition line are depicted by the solid and dashed lines, respectively. The meeting point A is a tricritical point (TCP) of the P-restoration transition. For the EPNJL model of panel (b), the chiral and the P restoration transition are always first order and hence there is no TCP.

In the PNJL model of panel (a), the dotted line from point C to point A is a trajectory of CEP as θ increases from 0 to π. Thus the second-order chiral transition line ends up with point A. This means that the CEP (point C) at $\theta = 0$ is a remnant of the TCP (point A) of P restoration at $\theta = \pi$. In the EPNJL model of panel (b), no TCP and then no CEP appears in the μ_q-T plane at $\theta = \pi$. The second-order chiral-transition line (dashed line) starting from point C never reaches the μ_q-T plane at $\theta = \pi$.

Figure 3.7 snows the projection of the second-order chiral-transition line in the μ_q-

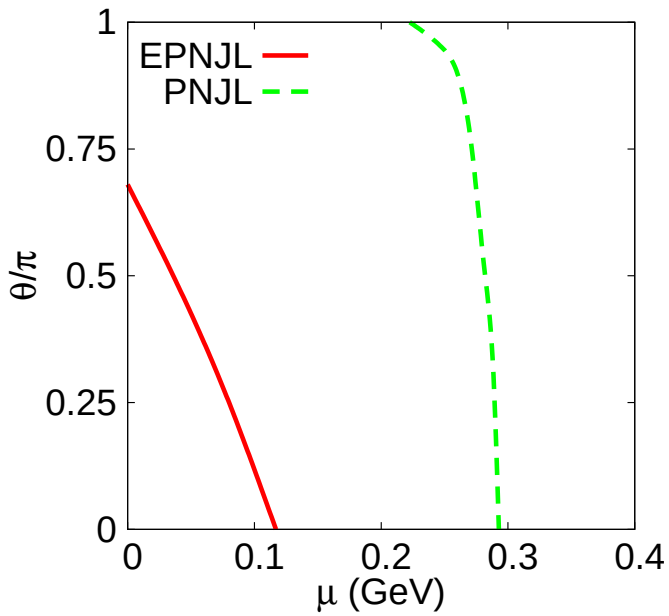

Fig. 3.7 The projection of the second-order chiral-transition line in the $\mu_{\rm q}$-θ-T space on the $\mu_{\rm q}$-θ plane. See the legend for the definition of line.

θ-T space on the $\mu_{\rm q}$-θ plane. The solid (dashed) line stands for the projected line in the EPNJL (PNJL) model. The first-order transition region exists on the right-hand side of the line, while the left-hand side corresponds to the chiral crossover region. The first-order transition region is much wider in the EPNJL model than in the PNJL model. In the EPNJL model, eventually, the chiral transition becomes first order even at $\mu_{\rm q} = 0$ when θ is large.

3.3.3 The sign problem on LQCD with finite θ

In the PNJL Lagrangian (3.4) after the transformation (3.2) and (3.3), θ dependence appears only at the light quark mass terms, $m_l \cos(\theta/2)$ and $m_l \sin(\theta/2)$. These terms are much smaller than Λ_{QCD} as a typical scale of QCD. This means that the condensates, σ_l', σ_s', η_l' and η_s', have weak θ dependence. This statement is supported by the results of the PNJL calculations shown in Fig. 3.8.

The sign problem is induced by the θ-odd $m_l \sin(\theta/2)$ term. The θ-odd (P-odd) condensates, η_l' and η_s', are generated by the θ-odd mass term. One can see in Fig. 3.8 that the θ-odd condensates are much smaller than the θ-even condensates, σ_l' and σ_s'.

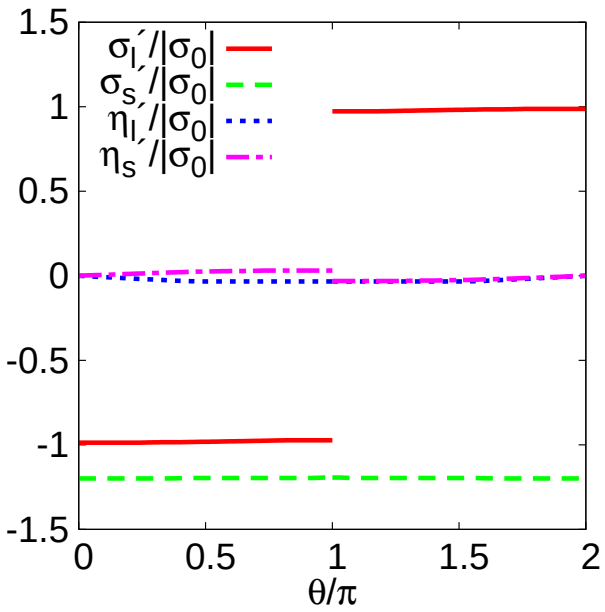

Fig. 3.8 θ dependence of the order parameters, σ_l', σ_s', η_l' and η_s', at $T = \mu_{\rm q} = 0$ calculated with the EPNJL model. See the legend for the definition of lines.

This fact indicates that effects of the θ-odd mass term are negligible. Actually, if the term is neglected, the θ-even condensates change only within the thickness of line, while the θ-odd condensates vanish. The neglect of the θ-odd mass is thus a good approximation.

The validity of the approximation can be shown more explicitly in the following way. The θ-odd (P-odd) condensates, η_l' and η_s', are zero at $\theta = 0$, since the θ-odd mass vanishes there. The weak θ dependence of η_l' and η_s' guarantees that η_l' and η_s' are small for any θ. Setting $\eta_l' = \eta_s' = 0$ in M_l' and N_l' leads to

$$M_l' = \cos\left(\tfrac{\theta}{2}\right) m_l - 4G_{\rm S}\sigma_l' + 2G_{\rm D}\sigma_s'\sigma_l', \tag{3.22}$$

$$N_l' = \sin\left(\tfrac{\theta}{2}\right) m_l, \tag{3.23}$$

where $M_l' \approx \Lambda_{\rm QCD}$ and $N_l' \approx m_l$. Since the thermodynamic potential is a function of $M_l'^2 + N_l'^2$, the term $N_l'^2$ is negligible compared with $M_l'^2$.

In LQCD, the vacuum expectation value of operator $\mathcal{O}$ is obtained by

$$\langle \mathcal{O} \rangle = \int \mathcal{D}A \mathcal{O} \left(\det \mathcal{M}_l(\theta)\right)^2 \det \mathcal{M}_s e^{-S_g} \tag{3.24}$$

$$= \int \mathcal{D}A \mathcal{O}' \left(\det \mathcal{M}_l'(\theta)\right)^2 \det \mathcal{M}_s e^{-S_g} \tag{3.25}$$

with the gluon part S_g of the QCD action and

$$\mathcal{O}' \equiv \mathcal{O}\frac{\left(\det\mathcal{M}_l(\theta)\right)^2}{\left(\det\mathcal{M}'_l(\theta)\right)^2}, \tag{3.26}$$

where $\det\mathcal{M}'_l(\theta)$ is the Fermion determinant in which the θ-odd mass is neglected and hence has no sign problem. As mentioned above, one can assume that

$$\frac{\det\mathcal{M}_l(\theta)}{\det\mathcal{M}'_l(\theta)} \approx 1. \tag{3.27}$$

Thus the reweighting method defined by (3.25) may work well. In the θ-even mass, $m_l\cos(\theta/2)$, the limit of $\theta = \pi$ corresponds to the limit of $m_l = 0$ with m_s fixed. Although the limit is hard to reach, one can analyze the dynamics at least at small and intermediate θ.

3.4 Introduction: Lattice QCD simulation with theta term

In the previous section, we proposed a way of minimizing the sign problem on LQCD with finite θ. The proposal is as follows. For simplicity, we consider two-flavor QCD. The QCD Lagrangian (1.1) is transformed into

$$\mathcal{L}_{QCD} = \bar{q}'\mathcal{M}(\theta)q' + \frac{1}{4g^2}F^a_{\mu\nu}F^a_{\mu\nu} \tag{3.28}$$

with

$$\mathcal{M}(\theta) \equiv \gamma_\nu D_\nu + m\cos\left(\theta/2\right) + mi\gamma_5\sin\left(\theta/2\right) \tag{3.29}$$

by using the $U_{\rm A}(1)$ transformation

$$q = e^{i\gamma_5\frac{\theta}{4}}q', \tag{3.30}$$

where the quark field $q = (q_u, q_d)$ has been redefined by the new one q'. The determinant $\mathcal{M}(\theta)$ satisfies

$$\det\mathcal{M}(\theta) = \left[\det\mathcal{M}(-\theta)\right]^*, \tag{3.31}$$

indicating that the sign problem is induced by the P-odd (θ-odd) term, $mi\gamma_5\sin\left(\theta/2\right)$. The difficulty of the sign problem is minimized in (3.28), since the P-odd term with

the light quark mass m is much smaller than the dynamical quark mass of order $\Lambda_{\rm QCD}$. Actually, it was found that the P-even condensates $\sigma'_f = \langle \bar{q}'_f q'_f \rangle$ is much larger than the P-odd condensates $\eta'_f = \langle \bar{q}'_f i\gamma_5 q'_f \rangle$. The P-even condensates little change even if the θ-odd mass term is neglected.

We then proposed the following reweighting method. The vacuum expectation value of operator $\mathcal{O}$ is calculated by

$$\langle \mathcal{O} \rangle = \int \mathcal{D}A \mathcal{O} \det\mathcal{M}(\theta) e^{-S_g} \tag{3.32}$$

$$= \int \mathcal{D}A \mathcal{O}' \det\mathcal{M}_{\rm ref}(\theta) e^{-S_g} \tag{3.33}$$

with the gluon part S_g of the QCD action and

$$\mathcal{O}' \equiv R(\theta)\mathcal{O}, \tag{3.34}$$

$$R(\theta) \equiv \frac{\det\mathcal{M}(\theta)}{\det\mathcal{M}_{\rm ref}(\theta)}, \tag{3.35}$$

where $R(\theta)$ is the reweighting factor and $\det \mathcal{M}_{\rm ref}(\theta)$ is the Fermion determinant of the reference theory that has no sign problem. The simplest candidate of the reference theory is the theory in which the θ-odd mass is neglected. We refer this reference theory to as reference A in this thesis. As discussed in Sec. 3.3, reference A may be a good reference theory for small and intermediate θ, but not for large θ near π. In reference A, the limit of $\theta = \pi$ corresponds to the chiral limit that is hard for LQCD simulations to reach.

The expectation value of $R(\theta)$ in the reference theory is obtained by

$$\langle R(\theta) \rangle = \frac{Z}{Z_{\rm ref}} \tag{3.36}$$

where Z ($Z_{\rm ref}$) is the partition function of the original (reference) theory. The average reweighting factor $\langle R(\theta) \rangle$ is a good index for the reference theory to be good; the reference theory is good when $\langle R(\theta) \rangle = 1$.

3.5 Model setting

The two-flavor PNJL Lagrangian with the θ-dependent anomaly term is obtained in Euclidean spacetime by

$$\begin{aligned}\mathcal{L} = &\bar{q}(\gamma_\nu D_\nu + m_0)q - G_1 \sum_{a=0}^{3} \left[(\bar{q}\tau_a q)^2 + (\bar{q} i\gamma_5 \tau_a q)^2\right] \\ &-8G_2 \left[e^{i\theta}\mathrm{det}\bar{q}_\mathrm{R} q_\mathrm{L} + e^{-i\theta}\mathrm{det}\bar{q}_\mathrm{L} q_\mathrm{R}\right] + \mathcal{U}(T, \Phi, \Phi^*). \end{aligned} \tag{3.37}$$

Under the $U_A(1)$ transformation (3.30), the quark-antiquark condensates are transformed as

$$\sigma \equiv \langle \bar{q} q \rangle = \cos(\theta/2)\sigma' + \sin(\theta/2)\eta', \tag{3.38}$$

$$\eta \equiv \langle \bar{q} i\gamma_5 q \rangle = -\sin(\theta/2)\sigma' + \cos(\theta/2)\eta', \tag{3.39}$$

$$a_i \equiv \langle \bar{q} \tau_i q \rangle = \cos(\theta/2)a_i' + \sin(\theta/2)\pi_i', \tag{3.40}$$

$$\pi_i \equiv \langle \bar{q} i\gamma_5 \tau_i q \rangle = -\sin(\theta/2)a_i' + \cos(\theta/2)\pi_i', \tag{3.41}$$

where the condensates $\{\sigma', \eta', a_i', \pi_i'\}$ are defined by the same form as $\{\sigma, \eta, a_i, \pi_i\}$ but q is replaced by q'. The Lagrangian density is then rewritten with q' as

$$\begin{aligned}\mathcal{L} = &\bar{q}'(\gamma_\nu D_\nu + m(\theta))q' - G_1 \sum_{a=0}^{3} \left[(\bar{q}'\tau_a q')^2 + (\bar{q}' i\gamma_5 \tau_a q')^2\right] \\ &-8G_2 \left[\mathrm{det}\bar{q}_\mathrm{R}' q_\mathrm{L}' + \mathrm{det}\bar{q}_\mathrm{L}' q_\mathrm{R}'\right] + \mathcal{U} \end{aligned} \tag{3.42}$$

$$\begin{aligned}= &\bar{q}'(\gamma_\nu D_\nu + m(\theta))q' - G_+ \left[(\bar{q}' q')^2 + (\bar{q}' i\gamma_5 \vec{\tau} q')^2\right] \\ &-G_- \left[(\bar{q}' \vec{\tau} q')^2 + (\bar{q}' i\gamma_5 q')^2\right] + \mathcal{U}, \end{aligned} \tag{3.43}$$

where $G_\pm = G_1 \pm G_2$ and

$$m(\theta) = m_0 \cos(\theta/2) + m_0 i\gamma_5 \sin(\theta/2). \tag{3.44}$$

Making the mean field approximation and the path integral over the quark field, one can obtain the thermodynamic potential Ω (per volume) for finite T:

$$\begin{aligned}\Omega = U + \mathcal{U} - 2N_{\rm c}\sum_{\pm}\int_{\Lambda}\frac{d^3p}{(2\pi)^3}E_{\pm} \\ -2\sum_{\pm}\int\frac{d^3p}{(2\pi)^3}\Big[T\ln\left[1+3\Phi e^{-\beta E_{\pm}}+3\Phi^* e^{-2\beta E_{\pm}}+e^{-3\beta E_{\pm}}\right] \\ +T\ln\left[1+3\Phi^* e^{-\beta E_{\pm}}+3\Phi e^{-2\beta E_{\pm}}+e^{-3\beta E_{\pm}}\right]\Big]. \end{aligned} \tag{3.45}$$

with

$$E_{\pm} = \sqrt{\vec{p}^{\,2} + C \pm 2\sqrt{D}}, \tag{3.46}$$

$$C = M^2 + N^2 + A^2 + P^2, \tag{3.47}$$

$$D = (M\vec{A} + N\vec{P})^2 + (\vec{A}\times\vec{P})^2 \geq 0, \tag{3.48}$$

$$M = m_0\cos(\theta/2) - 2G_+\sigma', \tag{3.49}$$

$$N = m_0\sin(\theta/2) - 2G_-\eta', \tag{3.50}$$

$$\vec{A} = -2G_-\vec{a}', \quad \vec{P} = -2G_+\vec{\pi}', \tag{3.51}$$

$$A = \sqrt{\vec{A}\cdot\vec{A}}, \quad P = \sqrt{\vec{P}\cdot\vec{P}}, \tag{3.52}$$

$$U = G_+(\sigma'^2 + \vec{\pi}'^2) + G_-(\eta'^2 + \vec{a}'^2), \tag{3.53}$$

where the momentum integral is regularized by the three-dimensional momentum cutoff Λ. Following Refs. [178, 179], we introduce a parameter c as $G_1 = (1-c)G_+$ and $G_2 = cG_+$, where $0 \leq c \leq 0.5$ and $G_+ > 0$. The present model thus has four parameters of m_0, λ, G_+ and c. Assuming $m_0 = 5.5$ MeV, we have determined Λ and G_+ from the pion decay constant $f_\pi = 93$ MeV and the pion mass $M_\pi = 138$ MeV at vacuum. Although c is an unknown parameter, we set $c = 0.2$ here, since it is known from the model analysis on the $\eta - \eta'$ splitting that $c \approx 0.2$ is favorable [185].

For finite θ, parity is broken explicitly, so it is not a good quantum number anymore. Hence P-even and P-odd modes are mixed with each other for each meson. The "pion" mass $\tilde{M}_\pi$ is defined by the lowest pole mass of the inverse propagator in the isovector channel. It agrees with the ordinary pion mass when $\theta = 0$. Under the random phase

approximation [186], the inverse propagator is described by

$$\det[1 - 2G\Pi(\tilde{M}_\pi^2)] = 0, \tag{3.54}$$

where

$$G = \begin{pmatrix} G_- & 0 \\ 0 & G_+ \end{pmatrix}, \tag{3.55}$$

$$\Pi(\omega^2) = \begin{pmatrix} \Pi^{SS}(\omega^2) & \Pi^{SP}(\omega^2) \\ \Pi^{PS}(\omega^2) & \Pi^{PP}(\omega^2) \end{pmatrix} \tag{3.56}$$

with

$$\Pi^{PP} = 4N_f N_c I_1 - 2N_f N_c (q^2 - 4N^2) I_2(\omega^2), \tag{3.57}$$

$$\Pi^{SS} = 4N_f N_c I_1 - 2N_f N_c (q^2 - 4M^2) I_2(\omega^2), \tag{3.58}$$

$$\Pi^{SP} = \Pi^{PS} = -8N_f N_c M N I_2(\omega^2), \tag{3.59}$$

$$I_1 = \int_\Lambda \frac{d^3p}{(2\pi)^3} \frac{1 - f_\Phi^+(E_p) - f_\Phi^-(E_p)}{2E_p}, \tag{3.60}$$

$$I_2(\omega^2) = \int_\Lambda \frac{d^3p}{(2\pi)^3} \frac{1 - f_\Phi^+(E_p) - f_\Phi^-(E_p)}{E_p(\omega^2 - 4E_p^2)}, \tag{3.61}$$

and

$$f_\Phi^+ = \frac{(\Phi^* + 2\Phi e^{-\beta E_p})e^{-\beta E_p} + e^{-3\beta E_p}}{1 + 3(\Phi^* + \Phi e^{-\beta E_p})e^{-\beta E_p} + e^{-3\beta E_p}}, \tag{3.62}$$

$$f_\Phi^- = \frac{(\Phi + 2\Phi^* e^{-\beta E_p})e^{-\beta E_p} + e^{-3\beta E_p}}{1 + 3(\Phi + \Phi^* e^{-\beta E_p})e^{-\beta E_p} + e^{-3\beta E_p}}. \tag{3.63}$$

In this form, we can set $\vec{a}' = \vec{\pi}' = 0$, since we do not consider the isospin chemical potential.

Applying the saddle-point approximation to the path integral in the partition function, one can get

$$\langle R(\theta) \rangle \approx \sqrt{\frac{\det H_{\rm ref}}{\det H}} e^{-\beta V(\Omega - \Omega_{\rm ref})} \tag{3.64}$$

where $\beta = 1/T$, Ω ($\Omega_{\rm ref}$) is the thermodynamic potential of the original (reference) theory in the mean-field level, and H ($H_{\rm ref}$) is the Hessian matrix in the original

(reference) theory defined by [102, 187]

$$H_{ij} = \frac{\partial^2 \Omega}{\partial \phi'_i \partial \phi'_j}, \tag{3.65}$$

$$\{\phi_i\} = \{\sigma', \eta', a'_i, \pi'_i, \Phi, \Phi^*\}. \tag{3.66}$$

For later convenience, the average reweighting factor $\langle R(\theta) \rangle$ is divided into two factors R_H and R_Ω:

$$\langle R(\theta) \rangle = R_H R_\Omega \tag{3.67}$$

with

$$R_H = \sqrt{\frac{\det H_{\rm ref}}{\det H}}, \tag{3.68}$$

$$R_\Omega = e^{-\beta V(\Omega - \Omega_{\rm ref})}. \tag{3.69}$$

For an $N_x^3 \times N_\tau$ lattice, the four-dimensional volume βV is obtained by

$$\beta V = \left(\frac{N_x}{N_\tau}\right)^3 \frac{1}{T^4}. \tag{3.70}$$

Here we consider $N_x/N_\tau = 4$ as a typical example, following Refs. [102, 187].

We consider the following reference theory that has no sign problem:

$$\mathcal{L} = \bar{q}'(\gamma_\nu \partial_\nu + m_{\rm ref}(\theta))q' - G_+ \left[(\bar{q}'q')^2 + (\bar{q}' i\gamma_5 \vec{\tau} q')^2\right] - G_- \left[(\bar{q}'\vec{\tau}q')^2 + (\bar{q}' i\gamma_5 q')^2\right] + \mathcal{U}.$$

Here $m_{\rm ref}(\theta)$ is θ-even mass defined below. We consider three examples as $m_{\rm ref}(\theta)$.

A. The first example is reference A defined by

$$m_{\rm ref}(\theta) \equiv m_{\rm A}(\theta) = m_0 \cos(\theta/2). \tag{3.71}$$

In this case, the P-odd mass is simply neglected from the original Lagrangian (3.43).

B. The second example is reference B defined by

$$\begin{aligned} m_{\rm ref}(\theta) &\equiv m_{\rm B}(\theta) \\ &= m_0 \cos(\theta/2) + \frac{1}{\alpha} \left\{m_0 \sin(\theta/2)\right\}^2. \end{aligned} \tag{3.72}$$

In this case, we have added the m_0^2-order correction due to the P-odd quark mass. Here α is a parameter with mass dimension, so we simply choose $\alpha = M_\pi$. The coefficient of the correction term is $m_0^2/M_\pi = 0.129$ MeV.

C. The third case is reference C defined by

$$\begin{aligned} m_{\rm ref}(\theta) &\equiv m_{\rm C}(\theta) \\ &= m_0 \cos(\theta/2) + \frac{m_0 M_\pi^2}{M_{\eta'}^2} \sin^2(\theta/2), \end{aligned} \tag{3.73}$$

This case also has the m_0^2-order correction, but α is different from reference B. The coefficient of the correction term is $m_0 M_\pi^2/M_{\eta'}^2 = 0.114$ MeV.

Reference C is justified as follows. The pion mass $\tilde{M}_\pi(\theta)$ at finite θ is estimated from the chiral Lagrangian as [160, 161]:

$$\tilde{M}_\pi^2(\theta) = \frac{m_0|\sigma_0|}{f_\pi^2}|\cos(\theta/2)| + \frac{2l_7 m_0^2 \sigma_0^2}{f_\pi^6}\sin^2(\theta/2), \tag{3.74}$$

where σ_0 is the chiral condensate at $T = \theta = 0$ and the coefficient l_7 is evaluated by the $1/N_c$ expansion as

$$l_7 \approx \frac{f_\pi^2}{2M_{\eta'}^2}. \tag{3.75}$$

The right-hand side of (3.74) is reduced to

$$\tilde{M}_\pi^2(\theta) = \frac{|\sigma_0|}{f_\pi^2}\left[m_0|\cos(\theta/2)| + \frac{m_0 M_\pi^2}{M_{\eta'}^2}\sin^2(\theta/2)\right]. \tag{3.76}$$

Equation (3.76) supports (3.73).

3.6 Numerical results

3.6.1 Mean field approximation

If some reference system satisfies the condition that $\langle R(\theta)\rangle \approx 1$, one can say that the reference system is good. As a typical example of the condition, we consider the case of $0.5 \lesssim \langle R(\theta)\rangle \lesssim 2$. This condition seems to be the minimum requirement. The discussion made below is not changed qualitatively, even if one takes a stronger condition.

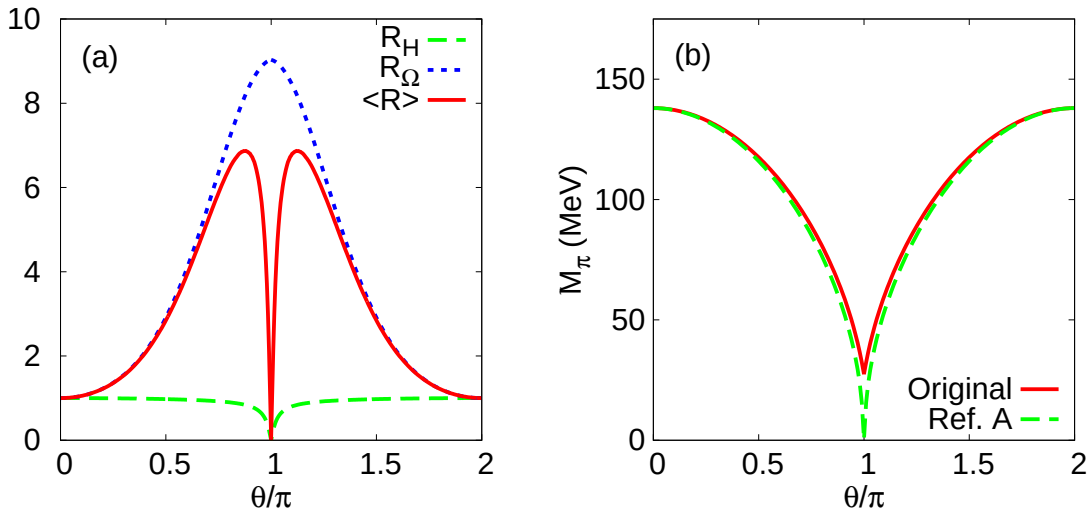

Fig. 3.9 θ dependence of (a) the average reweighting factor and (b) $\tilde{M}_\pi$ at $T = 100$ MeV for the case of reference A.

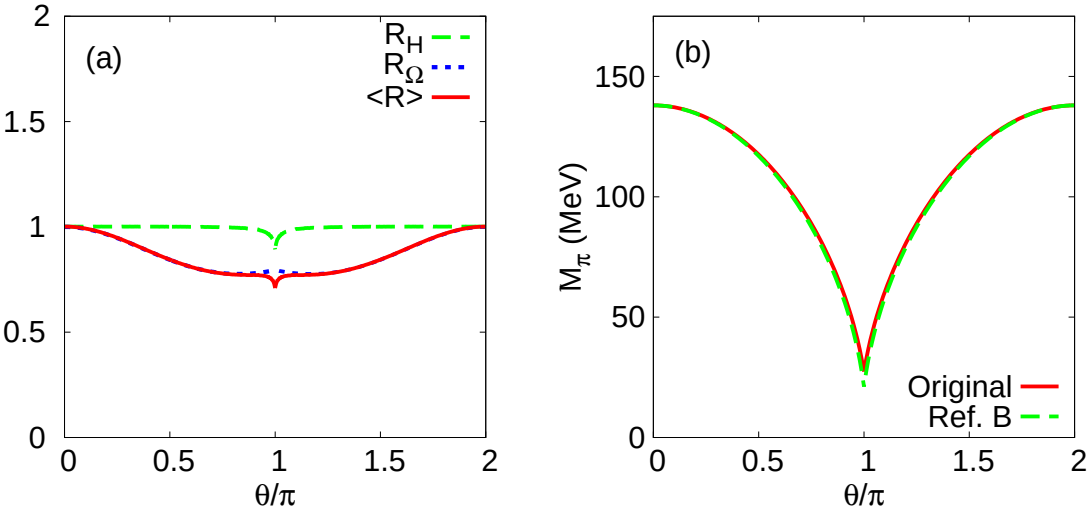

Fig. 3.10 θ dependence of (a) the average reweighting factor and (b) $\tilde{M}_\pi$ at $T = 100$ MeV for the case of reference B.

First we consider reference A. Figure 3.9(a) shows θ dependence of $\langle R(\theta)\rangle$ at $T = 100$ MeV. The solid line stands for $\langle R(\theta)\rangle$, while the dashed (dotted) line corresponds to R_H (R_Ω). This temperature is lower than the chiral transition temperature in the original theory that is 212 MeV at $\theta = 0$ and 204 MeV at $\theta = \pi$. As θ increases from zero, $\langle R(\theta)\rangle$ also increases and exceeds 2 at $\theta \approx 1.2$. Reference A is thus good for $\theta \lesssim 1.2$. The increase of $\langle R(\theta)\rangle$ stems from that of R_Ω that depends on T. This means

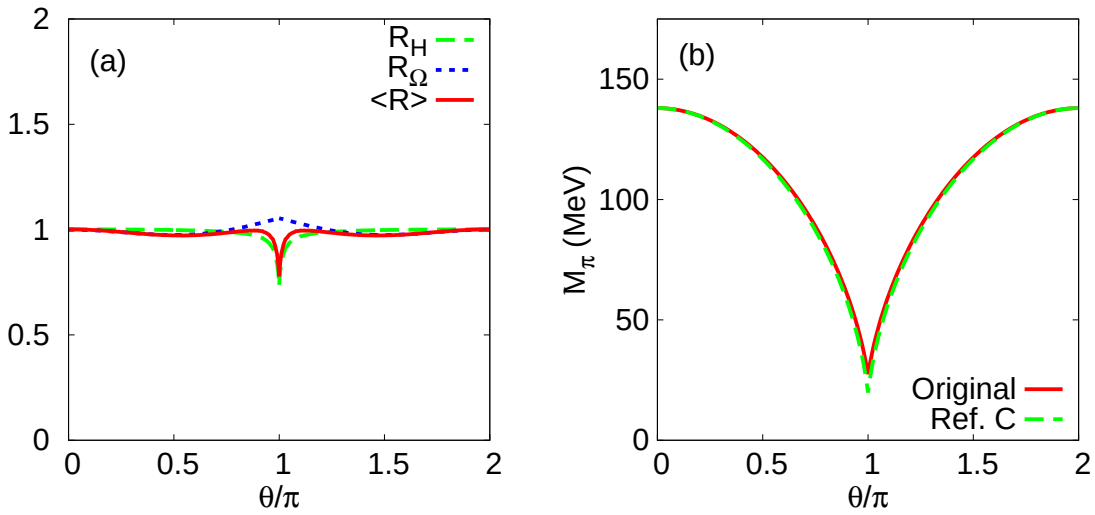

Fig. 3.11 θ dependence of (a) the average reweighting factor and (b) $\tilde{M}_\pi$ at $T = 100$ MeV for the case of reference C.

that the reliable θ region in which $0.5 \lesssim \langle R(\theta) \rangle \lesssim 2$ becomes large as T increases.

Figure 3.9(b) shows θ dependence of $\tilde{M}_\pi$ at $T = 100$ MeV. The solid (dashed) line denotes $\tilde{M}_\pi$ in the original (reference A) system. At $\theta = \pi$, $\tilde{M}_\pi$ is finite in the original system, but zero in reference A. As a consequence of this property, R_H and $\langle R(\theta) \rangle$ vanish at $\theta = \pi$; see Fig. 3.9(a). This indicates that reference A breaks down at $\theta = \pi$, independently of T.

The same analysis is made for reference B in Fig. 3.10. $\tilde{M}_\pi$ in reference B well reproduces that in the original theory for any θ, and $\langle R(\theta) \rangle$ satisfies the condition $0.5 \lesssim \langle R(\theta) \rangle \lesssim 2$ for all θ. Since $R_H \sim 1$ in the most region of θ, $\langle R(\theta) \rangle$ is governed by R_Ω. Around $\theta = \pi$, R_H becomes small but still has a nonzero value because $\tilde{M}_\pi \neq 0$ even at $\theta = \pi$ in reference B. Therefore, the simple estimation for $m_{\rm ref}(\theta)$ (3.72) gives available reference.

Finally we consider reference C through Fig. 3.11. $\tilde{M}_\pi$ in reference C well simulates that in the original theory, and $\langle R(\theta) \rangle$ satisfies the condition $0.5 \lesssim \langle R(\theta) \rangle \lesssim 2$ for all θ. This result is better than that in reference B. Therefore we can think that reference C is a good reference system for any θ. This is true for any temperature larger than 100 MeV.

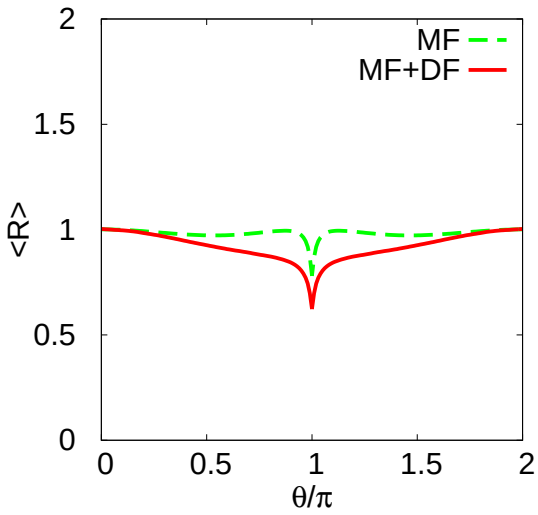

Fig. 3.12 θ dependence of the average reweighting factor at $T = 100$ MeV for the case of reference C. Solid and dashed lines correspond to the result with and without dynamical pion fluctuation respectively.

3.6.2 Effect of mesonic fluctuation

Beyond the mean field approximation, we estimate an effect of dynamical pion fluctuations by modifying the thermodynamic potential to

$$\Omega = \Omega_{\rm MF} + \Omega_{\rm DF}, \tag{3.77}$$

where $\Omega_{\rm MF}$ is the thermodynamic potential (3.45) with the mean-field level. $\Omega_{\rm DF}$ is the potential due to dynamical pion fluctuations [102],

$$\Omega_{\rm DF} = 3 \int \frac{d^3p}{(2\pi)^3} T \ln\left(1 - e^{-\beta E_\pi}\right), \tag{3.78}$$

where $E_\pi = \sqrt{\vec{p}^{\,2} + \tilde{M}_\pi^2}$, with $\tilde{M}_\pi$ determined by solving (3.54).

Figure 3.12 shows θ dependence of $\langle R(\theta)\rangle$ at $T = 100$ MeV for the case of reference C. The solid and dashed lines correspond to results with and without dynamical pion fluctuations, respectively. The effect makes $\langle R\rangle$ a little smaller and hence the reference C becomes slightly worse. However, the modification is small , indicating that $\langle R\rangle$ is well evaluated by the mean-field approximation

3.7 Short summary

The θ term in the QCD Lagrangian is an interesting subject, because it is related to topologically nontrivial structure of QCD vacuum. Although θ is small from experiments, the topological structure itself is important from $U(1)_{\rm A}$ anomaly. The θ term has been investigated as an external field to QCD, because it can be a useful probe to observe non-perturbative properties of QCD vacuum. However, QCD phase structure with finite θ parameter is still unknown because the first-principle LQCD simulation is not feasible. Hence, we have performed the following two kinds of analyses with effective models.

First, we have investigated effects of the theta vacuum on the QCD phase diagram for the realistic 2+1 flavor system, using the three-flavor PNJL and EPNJL models. The effects can be easily understood by the $SU_{\rm A}(3) \otimes U_{\rm A}(1)$ transformation, (3.2) and (3.3). After the transformation, the θ-odd mass, $m_l \sin(\theta/2)$, little affects the dynamics, so that the dynamics is mainly governed by the θ-even mass, $m_l \cos(\theta/2)$. In the θ-even mass, the increase of θ corresponds to the decrease of m_l with m_s fixed. This means that the chiral transition becomes strong as θ increases. This is true in the results of both PNJL and EPNJL calculations. Particularly in the EPNJL model that is more reliable than the PNJL model, the transition becomes first-order even at $\mu = 0$ when θ is large. This result is important. If the chiral transition becomes first order at $\mu = 0$, it will change the scenario of cosmological evolution. For example, the first-order transition allows us to think the inhomogeneous Big-Bang nucleosynthesis model or a new scenario of baryogenesis.

Secondary, we have investigated a way of circumventing the sign problem in LQCD simulations with finite θ, using the PNJL model. We have considered the reweighting method for the transformed Lagrangian (3.28). In the Lagrangian, the sign problem is minimized, since the P-odd mass is much smaller than the dynamical quark mass of order $\Lambda_{\rm QCD}$. Another key is which kind of reference system satisfies the condition $\langle R(\theta) \rangle \approx 1$. We have then estimated $\langle R(\theta) \rangle$ by using the two-flavor PNJL model and have found that reference C may be a good reference system in the reweighting

method. We have performed a similar analysis with a more simplified model, the NJL model [188]. The analysis gave qualitatively similar results, and it shows that the dynamics is mostly dominated by chiral dynamics.

Since the present proposal is based on the model analysis, it is then not obvious whether the proposal really works in lattice simulations. Therefore the proposal should be directly tested by lattice simulations. A similar test was made for two-flavor QCD with finite quark chemical potential μ [102,189] where lattice simulations have the sign problem. The average reweighting factor, i.e., the average phase factor was evaluated by lattice simulations at $\mu/T < 1$ for T around the critical temperature of the deconfinement transition [189]. The PNJL model well reproduces the lattice result, when the dynamical correction due to mesonic fluctuations is made to the mean-field model calculation [102]. It is thus interesting that the present proposal is directly tested by lattice simulations.

Chapter 4

QCD phase diagram based on LQCD and NS measurement

We determine the quark-hadron transition line in the whole region of the T-$\mu_{\rm B}$ plane from LQCD results and neutron-star (NS) mass measurements, making the quark-hadron hybrid model that is consistent with the two solid constraints. The quark part of the hybrid model is the EPNJL model that reproduces LQCD results at $\mu_{\rm B}/T = 0$, while the hadron part is the hadron resonance gas model with volume-exclusion effects that reproduces NS mass measurements and the neutron-matter equation of state calculated from the two- and three-nucleon forces based on the chiral effective field theory. The lower bound of the critical $\mu_{\rm B}$ of the quark-hadron transition at zero T is $\mu_{\rm B} \sim 1.6$ GeV for the isospin symmetric matter. The interplay between the heavy-ion collision physics around $\mu_{\rm B}/T = 6$ and the NS physics at $\mu_{\rm B}/T = 1$ is discussed.

4.1 Introduction: Neutron star and equation of state

The phase diagram of QCD is a key to understanding not only natural phenomena such as compact stars and the early Universe but also laboratory experiments such as relativistic heavy-ion collisions [35, 36, 38, 41, 56, 125]. The first-principle LQCD simulation as a quantitative analysis of the phase diagram [41, 56, 125], however, has the severe sign problem at middle and large $\mu_{\rm B}/T$, where T is temperature and $\mu_{\rm B}$ is baryon-number chemical potential. Therefore the QCD phase diagram is still unknown particularly at $\mu_{\rm B}/T \gtrsim 1$, although many possibilities are proposed by effective models there. A steady way of approaching the middle and large $\mu_{\rm B}/T$ regions is gathering solid information from different regions and extracting a consistent picture from the information.

LQCD simulations are quite successful at $\mu_{\rm B}/T \lesssim 1$ [41–43, 56, 125, 190–192]. They are providing high-precision results for the realistic 2+1 flavor system at the present day, for example the transition temperature, the equation of state (EoS), and fluctuations of conserved charges [42, 43, 191, 192]. As a way of extending the understanding to the $\mu_{\rm B}/T \gtrsim 1$ region, we can consider effective models such as the PNJL model. Actually, some improved versions of the PNJL model yield desirable results consistent with LQCD simulations at $\mu_{\rm B}/T \lesssim 1$ [36, 71, 72, 74, 101, 106]. However, the model approach has still various ambiguity at large $\mu_{\rm B}/T$.

A key issue in the large $\mu_{\rm B}/T$ limit, i.e. at finite $\mu_{\rm B}$ but vanishing T, is the EoS of nuclear matter. It is one of the most important subjects in nuclear physics to understand properties of symmetric nuclear matter and neutron matter microscopically from realistic baryon-baryon interactions. Various theoretical frameworks have been developed to study the subject. The results seem to be reliable because most of them are now converging a common result, but the common result cannot reproduce empirical saturation properties properly if one starts with realistic two-nucleon forces (2NF). This insufficiency is probably due to the lack of including three-nucleon forces (3NF). Recent development of the chiral effective field theory (Ch-EFT) [193, 194] provides a way of determining 2NF and 3NF systematically from symmetries of un-

derlying QCD. Although the Ch-EFT interaction is, by construction, to be applied at low and normal nuclear densities, the standard many-nucleon calculation using the Ch-EFT 2NF and 3NF at these densities should provide the predictive base for considering the neutron-matter EoS at higher densities. The combination of this new constraint and the experimental constraint [195] evaluated from the heavy-ion collision measurements is considered to be useful to determine the nuclear-matter EoS solidly.

The mass-radius (MR) relation of neutron star (NS) is sensitive to the nuclear-matter EoS [196]. In this sense, astrophysical observations are another valuable source of information to provide a strong constraint on the EoS. Recent observations suggest the existence of massive NSs ($\sim 2M_\odot$), which seems to exclude the possibility of soft EoS [197, 198]. However, there exists uncertainties on the radius of NSs from various observations. Steiner *et al.* have adopted the statistical approach to constrain this uncertainty, and have provided the best fitting against various observations on the MR relation [199].

There is a possibility that the quark-hadron phase transition occurs in NSs. The observations on the MR relation yield a strong constraint on both the quark and hadron phases, while the nuclear-matter EoS determined from the Ch-EFT 2NF and 3NF and the heavy-ion collision measurements does on the hadron phase. Therefore, the combination of the solid constraints may answer an important question, whether the quark-hadron phase transition occurs in NSs and further what is the critical chemical potential of the transition if it occurs. This is nothing but to clarify the QCD phase diagram in the large $\mu_{\rm B}/T$ limit.

In this chapter, we determine the QCD phase diagram in the whole region from $\mu_{\rm B}/T = 0$ to infinity, constructing a reliable quark-hadron hybrid model. The quark part of the hybrid model is the Polyakov-loop extended Nambu-Jona-Lasinio (PNJL) model with entanglement vertex that reproduces LQCD data at finite imaginary $\mu_{\rm B}$, finite real- and imaginary-isospin chemical potentials, small real $\mu_{\rm B}$ [101, 106], and strong magnetic field [81]. The hadron part of the hybrid model is the hadron resonance gas (HRG) model with volume-exclusion effect that reproduces the NS observations and the nuclear-matter EoS evaluated from the Ch-EFT 2NF and 3NF and the

heavy-ion collision measurements. The volume-exclusion effect is necessary to reproduce the repulsive nature of the nuclear-matter EoS. The EoS provided by the hybrid model preserves the causality even at high $\mu_{\rm B}$. In order to construct the nuclear-matter EoS from the Ch-EFT 2NF and 3NF, we employ the lowest-order Brueckner theory (LOBT) in pure neutron matter with the Jülich N^{3}LO interaction [200]. The lower bound of the critical $\mu_{\rm B}$ of the quark-hadron transition at $T = 0$ is found to be $\mu_{\rm B} \sim 1.6$ GeV for the isospin symmetric matter. We also investigate the interplay between the heavy-ion collision physics around $\mu_{\rm B}/T = 6$ and the NS physics at $\mu_{\rm B}/T = \infty$.

4.2 Model setting

We consider a two-phase model to treat the quark-hadron phase transition by assuming that the transition is the first order [113, 114, 201–205]. For the quark phase, we use the 2-flavor EPNJL model [101, 105, 106] which yields consistent results with LQCD data for finite imaginary $\mu_{\rm B}$, finite real- and imaginary-isospin chemical potentials, small real $\mu_{\rm B}$ [101,106], and strong magnetic field [81]. For the hadron phase, we use the HRG model. The model is successful in reproducing the QCD EoS below the transition temperature at $\mu_{\rm B}/T = 0$ [42, 43, 191, 192]. This model is extended for the baryon part to include the volume-exclusion effect. The effect is necessary to reproduce the repulsive nature of the nuclear-matter EoS. The volume-exclusion radius is fitted to reproduce the nuclear-matter EoS determined from the Ch-EFT 2NF and 3NF and the heavy-ion collision measurements.

In this work, we consider the 2-flavor system and do not take into account the existence of hyperons [206]. Even with hyperons, the fraction of hyperons is suppressed by the existence of quarks in NS [207]. Hence, the possibility of the appearance of quarks is first discussed in this thesis. The possibility of the appearance of hyperons will be discussed in a forthcoming paper.

4.2.1 Quark phase

We first consider the quark phase with the two-flavor EPNJL model. The Lagrangian density is obtained in Euclidean spacetime by

$$\mathcal{L}_{\rm EPNJL} = \bar{q}(\gamma_\nu D_\nu + \hat{m}_0 - \gamma_4\hat{\mu})q - G(\Phi)[(\bar{q}q)^2 + (\bar{q}i\gamma_5\vec{\tau}q)^2] + \mathcal{U}(\Phi[A], \Phi^*[A], T), \quad (4.1)$$

where $D_\nu = \partial_\nu - i\delta_{\nu 4}A_4^a\lambda_a/2$ with the Gell-Mann matrices λ_a. The two-flavor quark fields $q = (q_{\rm u}, q_{\rm d})$ have masses $\hat{m}_0 = {\rm diag}(m_{\rm u}, m_{\rm d})$, and the quark-number chemical potential matrix $\hat{\mu}$ is defined by $\hat{\mu} = {\rm diag}(\mu_{\rm u}, \mu_{\rm d})$. For simplicity, we assume isospin symmetry for u and d masses: $m_l \equiv m_{\rm u} = m_{\rm d}$.

Performing the mean-field approximation and the path integral over the quark field, one can obtain the thermodynamic potential Ω (per volume):

$$\begin{aligned}\frac{\Omega}{V} &= G(\Phi)\sigma^2 + \mathcal{U} - 2N_{\rm c}\sum_{f={\rm u,d}}\int_\Lambda \frac{d^3p}{(2\pi)^3}E_f \\ &\quad -\frac{2N_{\rm c}}{\beta}\sum_{f={\rm u,d}}\int\frac{d^3p}{(2\pi)^3}\Big\{\ln\Big[1 + 3\Phi e^{-\beta(E_f-\mu_f)} + 3\Phi^* e^{-2\beta(E_f-\mu_f)} + e^{-3\beta(E_f-\mu_f)}\Big] \\ &\quad + \ln\Big[1 + 3\Phi^* e^{-\beta(E_f+\mu_f)} + 3\Phi e^{-2\beta(E_f+\mu_f)} + e^{-3\beta(E_f+\mu_f)}\Big]\Big\} \end{aligned} \quad (4.2)$$

with

$$E_f = \sqrt{\vec{p}^{\,2} + M_f^2}, \quad M_f = m_0 - 2G(\Phi)\sigma, \quad \sigma \equiv \langle\bar{q}q\rangle\,. \quad (4.3)$$

The quark-number densities $n_{\rm u}$ and $n_{\rm d}$ are obtained by

$$n_f = -\frac{\partial}{\partial\mu_f}\left(\frac{\Omega}{V}\right) \quad (4.4)$$

for $f = {\rm u, d}$ and pressure P is defined as $P = -(\Omega + \Omega_0)/V$, where Ω_0 is thermodynamic potential at $T = \mu_{\rm u} = \mu_{\rm d} = 0$.

The classical variables $X = \Phi$, Φ^* and σ are determined by the stationary conditions

$$\frac{\partial\Omega}{\partial X} = 0. \quad (4.5)$$

The solutions to the stationary conditions do not give the global minimum of Ω necessarily. They may yield a local minimum or even a maximum. We then have

checked that the solutions yield the global minimum when the solutions $X(T, \mu_{\rm u}, \mu_{\rm d})$ are inserted into Eq. (4.2). In this work, we employ an approximation $\Phi = \Phi^*$ for numerical simplicity, because the approximation is good and hence sufficient for the present analysis [102].

Repulsive forces among quarks are crucial to account for the $2M_\odot$-NS observation [113, 114, 208], since they harden the EoS of quark matter. We then introduce the vector-type four-body interaction to the EPNJL model [99],

$$\mathcal{L}_{\rm EPNJL} \;\rightarrow\; \mathcal{L}_{\rm EPNJL} + G_{\rm V}(\bar{q}\gamma_\mu q)^2. \tag{4.6}$$

The corresponding thermodynamic potential is obtained by the replacement,

$$\mu_f \rightarrow \mu_f - 2G_{\rm V} n_{\rm q}, \tag{4.7}$$

$$G(\Phi)\sigma^2 \rightarrow G(\Phi)\sigma^2 - G_{\rm V} n_{\rm q}^2 \tag{4.8}$$

with $n_{\rm q} \equiv \langle q^\dagger q \rangle$. Here, $n_{\rm q}$ is determined in a self-consistent manner to satisfy the thermodynamic relation (4.4). The parameter $G_{\rm V}$ is treated as a free parameter in this thesis. $G_{\rm V}$ dependence of the quark-hadron phase transition will be discussed in Sec. 4.3.

4.2.2 Hadron phase

Now we consider the hadron phase by using the HRG model and its extension. The pressure of the HRG model is composed of meson and baryon parts,

$$P_{\rm H} = P_{\rm M} + P_{\rm B} \tag{4.9}$$

where $P_{\rm H}, P_{\rm M}$ and $P_{\rm B}$ are pressures of hadronic, mesonic and baryonic matters, respectively.

In the quark phase, the u- and d-quark chemical potentials, $\mu_{\rm u}$ and $\mu_{\rm d}$, are described by the baryon-number and electric chemical potentials, $\mu_{\rm B}$ and $\mu_{\rm Q}$, as

$$\mu_{\rm u} = \mu_{\rm B}/3 + \frac{2}{3}\mu_{\rm Q}, \tag{4.10}$$

$$\mu_{\rm d} = \mu_{\rm B}/3 - \frac{1}{3}\mu_{\rm Q}. \tag{4.11}$$

In the hadron phase, meanwhile, the chemical potentials of proton, neutron and the ith meson with electric charge Q_i are expressed by $\mu_{\rm B}$ and $\mu_{\rm Q}$ as

$$\mu_{\rm p} = \mu_{\rm B} + \mu_{\rm Q}, \tag{4.12}$$

$$\mu_{\rm n} = \mu_{\rm B}, \tag{4.13}$$

$$\mu^i_{\rm M} = Q_i \mu_{\rm Q}, \tag{4.14}$$

respectively. For the QCD phase diagram, we consider only the case of the symmetric-nuclear matter with $\mu_{\rm Q} = 0$. In the NSs at zero T, meanwhile, there exist protons, neutrons, mesons and electrons. For simplicity, however, we neglect electrons and the Bose-Einstein condensation of mesons. This approximation is numerically confirmed to be valid; further analyses will be made in the forthcoming paper. In this case, the nuclear matter becomes the neutron matter because of the β equilibrium, i.e., $\mu_{\rm p} = 0$ and $\mu_{\rm n} = \mu_{\rm B} > 0$.

For the meson sector, we use the HRG model with no extension:

$$P_{\rm M} = \sum_i d_i T \int \frac{d^3p}{(2\pi)^3} \ln\left(1 - e^{-\beta(E_i - \mu^i_M)}\right), \tag{4.15}$$

$$E_i = \sqrt{\vec{p}^{\,2} + M_i^2}, \tag{4.16}$$

where the i summation is taken over all meson species constituted by u and d quarks in the quark model. Here, M_i, d_i and μ_i are mass, degeneracy and chemical potential of the ith meson, respectively. At $T = 0$, this simple formula yields the Bose-Einstein condensate when $\mu^i_{\rm M} > M_i$. However we neglect the effect by assuming $\mu^i_{\rm M} < M_i$ in order to reproduce the $2M_\odot$-NS observation. This assumption is justified, if the M_i increase at high densities and keep $\mu^i_{\rm M} < M_i$ by the mechanism such as the chiral symmetry restoration. The assumption leads to $P_{\rm M} = 0$ in the NSs at $T = 0$, that is, mesons do not directly contribute to the NS physics under the assumption.

The baryon sector is described by proton and neutron gases with the volume-exclusion effect [105,209,210] in order to reproduce the repulsive nature of the nuclear-matter EoS determined from the Ch-EFT 2NF and 3NF and the heavy-ion collision measurements that will be shown later in Sec. 4.2.3.

We consider the system of protons and neutrons having a finite volume v that is

characterized by the thermodynamic variables $(T, V, \mu_{\rm p}, \mu_{\rm n})$. Here, we assume that v is isospin symmetric; see the next section for the concrete expression of v. Following Refs. [105, 209, 210], we approximate the system of the finite-volume particles by the mimic system of point particles with $(T, \tilde{V}, \tilde{\mu}_{\rm p}, \tilde{\mu}_{\rm n})$ defined by

$$\tilde{V} = V - vN_{\rm B}, \tag{4.17}$$

$$\tilde{\mu}_i = \mu_i - vP_{\rm B}, \tag{4.18}$$

where $N_{\rm B}$ is the total baryon number. The $P_{\rm B}$ and $N_{\rm B}$ should be the same between the original and mimic systems. The chemical potential $\tilde{\mu}_i (i = {\rm p}, {\rm n})$ of the mimic system is determined to preserve the thermodynamic consistency. The pressure of the mimic system is obtained by

$$P_{\rm B} = \frac{2}{\beta} \sum_{i={\rm p,n}} \int \frac{d^3p}{(2\pi)^3} \left[\ln \left(1 + e^{-\beta(E_i - \tilde{\mu}_i)} \right) + \ln \left(1 + e^{-\beta(E_i + \tilde{\mu}_i)} \right) \right] \tag{4.19}$$

with $E = \sqrt{p^2 + M_i^2}$, $M_{\rm p} = 938$ MeV, and $M_{\rm n} = 940$ MeV [2]. The entropy density (s) and the number densities $(n_{\rm p}, n_{\rm n})$ in the original system are obtained from those in the mimic system as

$$s = \frac{\tilde{s}}{1 + v\tilde{n}_{\rm B}}, \quad n_i = \frac{\tilde{n}_i}{1 + v\tilde{n}_{\rm B}}, \tag{4.20}$$

where $\tilde{n}_{\rm B} = \tilde{n}_{\rm p} + \tilde{n}_{\rm n}$ and

$$\tilde{n}_i = \frac{\partial P_{\rm B}}{\partial \tilde{\mu}_i} \tag{4.21}$$

with $i = {\rm p}, {\rm n}$.

In the present formalism, the antiparticles have negative volumes, but the effects are negligible at both low and high densities. At low densities, the baryon number is small and hence the volume exclusion effect does not become relevant. At high densities, the particle number is much larger than the antiparticle number, and hence the net volume of antiparticles is negligibly small compared with that of particles.

4.2.3 LOBT calculation with Ch-EFT interactions

The Brueckner theory is a standard framework to describe nuclear matter starting from realistic 2N interactions. The reaction matrix G, defined by the G-matrix equa-

tion

$$G_{12} = v_{12} + v_{12}\frac{Q}{\omega - (t_1 + U_1 + t_2 + U_2)}G_{12}, \tag{4.22}$$

properly deals with short range (high momentum) singularities of the 2N potential v_{12}. The self-consistent determination of the single-particle (s.p.) potential U,

$$\langle i|U|i\rangle \equiv \sum_{j}^{\text{occupied}} \langle ij|G_{12}|ij - ji\rangle \tag{4.23}$$

corresponds to the inclusion of a certain class of higher-order correlations. In the above expression, Q stands for the Pauli exclusion, t_i is a kinetic energy operator, and ω is a sum of the initial two-nucleon s.p. energies. The reliability of the lowest-order calculation in the Brueckner theory has been demonstrated by the estimation of the smallness of the contribution of higher-order correlations on the one hand and by the consistency with the results from other methods such as variational framework [211].

The Ch-EFT provides a systematic determination of 2NF and 3NF. It is prohibitively hard, at present, to do full many-body calculations for infinite matter with including 3NF. The effects can be estimated by introducing a density-dependent effective 2N force $v_{12(3)}$ obtained by folding the third nucleon in infinite matter considered:

$$\begin{aligned}&\langle \boldsymbol{k}_1'\sigma_1'\tau_1', \boldsymbol{k}_2'\sigma_2'\tau_2'|v_{12(3)}|\boldsymbol{k}_1\sigma_1\tau_1, \boldsymbol{k}_2\sigma_2\tau_2\rangle_A \\ &= \sum_{\boldsymbol{k}_3\sigma_3\tau_3} \langle \boldsymbol{k}_1'\sigma_1'\tau_1', \boldsymbol{k}_2'\sigma_2'\tau_2', \boldsymbol{k}_3\sigma_3\tau_3|v_{123}|\boldsymbol{k}_1\sigma_1\tau_1, \boldsymbol{k}_2\sigma_2\tau_2, \boldsymbol{k}_3\sigma_3\tau_3\rangle_A,\end{aligned} \tag{4.24}$$

where σ and τ stand for the spin and isospin indices, and two-remaining nucleons are assumed to be in the center-of-mass frame, namely $\boldsymbol{k}_1' + \boldsymbol{k}_2' = \boldsymbol{k}_1 + \boldsymbol{k}_2$. The suffix A denotes an antisymmetrized matrix element. The G-matrix equation is set up for the two-body interaction $v_{12} + \frac{1}{3}v_{12(3)}$. The factor $\frac{1}{3}$ is necessary for properly taking into account the combinatorial factor in evaluating the total energy. The LOBT G-matrix calculation in this approximation turns out to give quantitatively satisfactory description for the fundamental properties of nucleon many-body systems, namely saturation and strong spin-orbit field: the latter is essential for accounting for nuclear shell structure. These results were briefly reported in Ref. [212].

In neutron matter, the contact c_E term of the Ch-EFT 3NF vanishes and the c_D term contributes negligibly. This means that the 3NF contributions in neutron matter

are determined by the parameters that are fixed in the 2NF sector. Thus ambiguities concerning the 3NF contributions are minimal with the use of the Ch-EFT, in contrast to past studies in which phenomenological regulations were often applied. Because many-body correlation effects are expected not to be large because of the absence of strong tensor-force correlations in the ^{3}E channel, the LOBT energies should be reliable in neutron matter.

Calculated energies of neutron matter with and without 3NF are shown in Fig. 4.1, where the cutoff energy $\Lambda_{\rm EFT}$ of the Ch-EFT 2NF and 3NF is 550 MeV. The solid and dashed curves are results using the Ch-EFT interactions with and without 3NF, respectively. The energy curve without 3NF is very close to that of the standard modern 2NF, AV18 [213]. For comparison, energies from the variational calculation by Illinois group [214] are included, which are frequently referred to as the standard EoS for discussing NS properties although their 3NF is phenomenological to some extent. It is interesting that the present prediction based on the Ch-EFT shows good correspondence to those energies.

In the application of the Ch-EFT, an estimation of theoretical uncertainties due to the uncertainties of the low-energy constants is customarily presented. As for the neutron-matter EoS, it is instructive to consult the estimation by Krüger *et al.* [215]. They show, in their Hatree-Fock type calculations, that the neutron-matter energy at saturation density is in a range of $14 \sim 17$ MeV for the Ch-EFT potential of the Jülich group [200] with the cutoff parameter of $450 \sim 700$ MeV from uncertainties of coupling constants and cutoff parameters as well as many-body theoretical treatment. Following this estimation, we add the shaded are to indicate possible uncertainties, simply assuming the ± 8 % of the potential contribution, which is -18.6 MeV at saturation density.

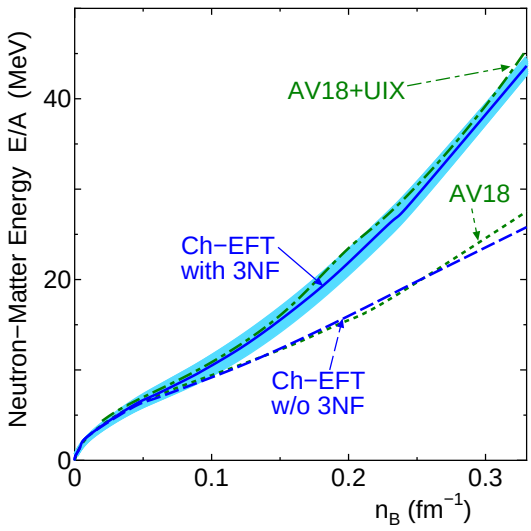

Fig. 4.1 Neutron-matter energies as a function of the density $n_{\rm B}$. The solid and dashed curves are results of the Ch-EFT interactions with and without 3NF, respectively. The shaded area shows possible uncertainties mentioned in the text. The dotted curve shows results of the AV18 2NF [213]. The typical result of the variational method by the Illinois group [214] is included by a dot-dashed curve, in which the Urbana 3NF is used together with the AV18.

4.3 Numerical results

4.3.1 Zero temperature

At zero temperature, the present hybrid model becomes simpler. Mesons do not contribute to the pressure, and the quark phase is described by the NJL model, since the EPNJL model is reduced to the NJL model there. In this section, we discuss the MR relation of NS, assuming that the hadron phase is a neutron-matter system.

The NJL model for the quark phase is solved under the condition

$$2n_{\rm u} = n_{\rm d}, \tag{4.25}$$

and the neutron-number density ($n_{\rm n}$) and its chemical potential ($\mu_{\rm n}$) are given by

$$n_{\rm n} = \frac{2n_{\rm d} - n_{\rm u}}{3}, \quad \mu_{\rm n} = \mu_{\rm u} + 2\mu_{\rm d}. \tag{4.26}$$

In the HRG model for the hadron phase, neutrons are assumed to have the exclusion volume v which depends on $\tilde{\mu}_{\rm B} = \tilde{\mu}_n$. The dependence is parameterized as

$$v = \frac{4}{3}\pi r_{\rm excl}^3, \tag{4.27}$$

$$r_{\rm excl}(\tilde{\mu}_{\rm B}) = r_0 + r_1\tilde{\mu}_{\rm B} + r_2\tilde{\mu}_{\rm B}^2. \tag{4.28}$$

Figure 4.2 shows $n_{\rm B}$ dependence of the neutron-matter pressure; note that $n_{\rm B} = n_{\rm n}$ in neutron matter and it is normalized by the normal nuclear density $\rho_0 = 0.17$ (fm^{-3}). Closed squares denote the results of LOBT calculations with the Ch-EFT 2NF and 3NF. The results are plotted in the region of $n_{\rm B} < 2\rho_0$, since the Fermi energy becomes larger than the cutoff energy $\Lambda_{\rm ERT}$ beyond $n_{\rm B} = 2\rho_0$. As shown in panel (a), the result (solid line) of the HRG model with the volume-exclusion effect well reproduces the results of LOBT calculations at $\rho_0 \lesssim n_{\rm B} \lesssim 2\rho_0$, when

$$r_0 = 0.50({\rm fm}), \tag{4.29}$$

$$r_1 = 0.50({\rm fm/GeV}), \tag{4.30}$$

$$r_2 = -0.34({\rm fm/GeV}^2). \tag{4.31}$$

More precisely, the model result needs the small correction $P \to P - 2({\rm MeV/fm}^3)$, but the error is smaller than the theoretical uncertainty of the Ch-EFT EoS estimated in Sec. 4.2.3. For $n_{\rm B} < \rho_0$, the agreement of the extended HRG model with the Ch-EFT EoS is not perfect, so the Ch-EFT EoS itself is used there whenever the MR relation is evaluated.

In panel (b), the neutron-matter pressure is plotted at higher $n_{\rm B}$. The hatching area shows the empirical EoS [195] evaluated from heavy-ion collisions in which the uncertainty coming from the symmetry energy is taken into account. The present HRG model is also consistent with this empirical result.

The speed of sound ($c_{\rm S}$) relative to the speed of light (c) is obtained by

$$\frac{c_{\rm S}}{c} = \sqrt{\frac{dP}{d\varepsilon}} \tag{4.32}$$

with the energy density ε. The ratio $c_{\rm S}/c$ should be smaller than 1 to preserve the causality. As shown in Fig. 4.3 that shows $n_{\rm B}$ dependence of $c_{\rm S}/c$, the present HRG model satisfies the causality even in the high-density region.

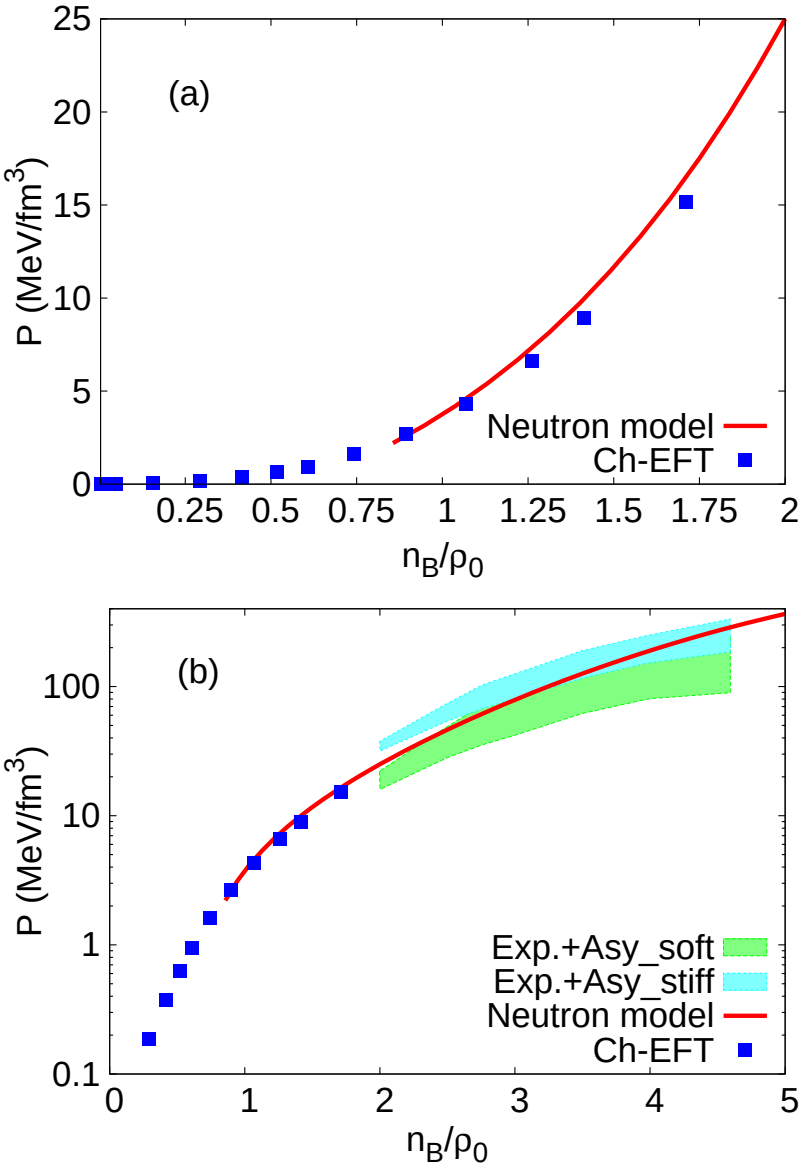

Fig. 4.2 Baryon-number density ($n_{\rm B}$) dependence of pressure (P) for neutron matter. $n_{\rm B}$ is normalized by the normal nuclear density $\rho_0 = 0.17$ (fm^{-3}). In the panel (b), experimental data is taken from Ref. [195].

Figure 4.4 shows $n_{\rm B}$ dependence of the neutron exclusion radius $r_{\rm excl}$. The resulting $r_{\rm excl}$ determined from the Ch-EFT and the empirical EoS has weak $n_{\rm B}$ dependence and the value is around 0.6 fm that is not far from the proton charge radius 0.877 fm [2]. This fact implies that the present model is reasonable as an effective model.

The MR relation of NS is obtained by solving the static and spherically symmetric

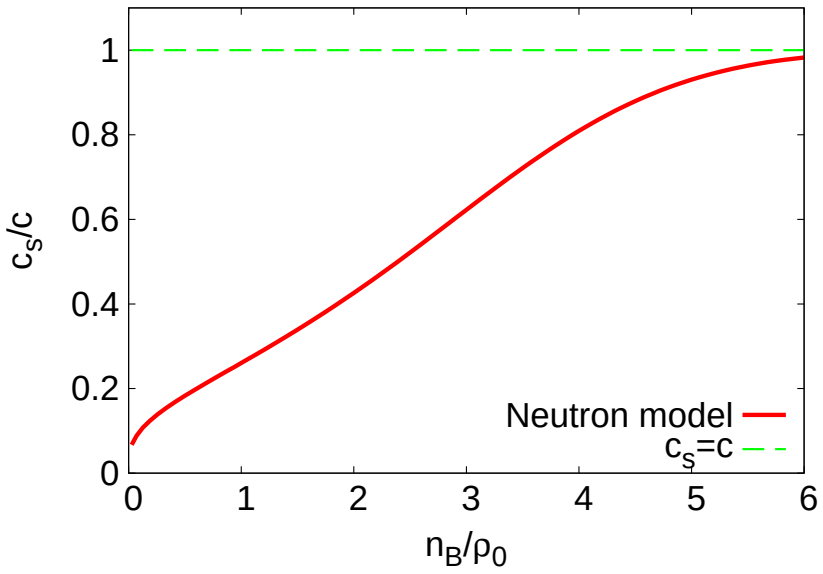

Fig. 4.3 Baryon-number density ($n_{\rm B}$) dependence of the speed of sound ($c_{\rm S}$) in neutron matter.

Einstein equation, i.e., the Tolman-Oppenheimer-Volkoff (TOV) equation,

$$\frac{dP}{dr} = -G_{\rm N}\frac{\varepsilon m}{r^2}\left(1+\frac{P}{\varepsilon}\right)\left(1+\frac{4\pi P r^3}{m}\right)\left(1-\frac{2G_{\rm N}m}{r}\right)^{-1},$$
$$\frac{dm}{dr} = 4\pi r^2\varepsilon \tag{4.33}$$

with $G_{\rm N}$ being the gravitational constant [216], where

$$m(r) = \int_0^r 4\pi r'^2\varepsilon(r')dr' \tag{4.34}$$

corresponds to the gravitational mass of the sphere of radius r. The solutions, $m(r)$ and $P(r)$, can be obtained by integrating the TOV equations numerically, when the EoS, $P = P(\varepsilon)$, is given. The integration stops at $r = R$ where $P(R) = 0$, and the maximum value R is the radius of NS and the mass is given by $M = m(R)$. Here, we adopt the Baym-Pethick-Sutherland (BPS) EoS for the outer crust [217]. Although, for the inner crust, we should consider the non-uniform structures, namely the pasta structures [218], we just connect the outer crust EoS to the Ch-EFT EoS at the subnuclear density smoothly, since this simplification does not affect on the MR relation. Similarly the Ch-EFT EoS is connected to the HRG-model EoS at $n_{\rm B} \sim \rho_0$.

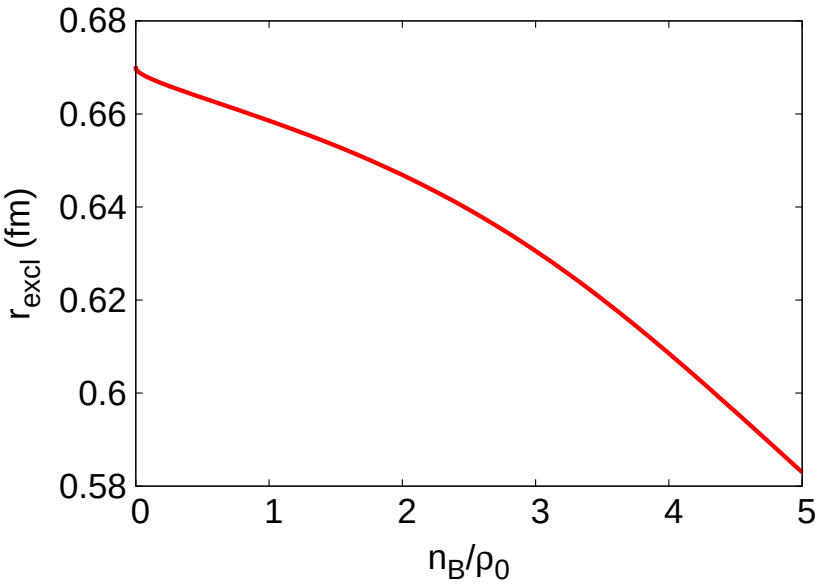

Fig. 4.4 Baryon-number density ($n_{\rm B}$) dependence of neutron exclusion radius ($r_{\rm excl}$).

Figure 4.5(a) shows the whole EoS.

Figure 4.5(b) shows the MR relation obtained by the hadron model mentioned above. The model result (dashed line) is compared with two observation data. The first one obtained by A. W. Steiner *et al.* is the best fitting against various observations on the MR relation [199]. This is not a strong constraint because of the uncertainty of the analysis particularly on X-ray burst phenomena. The second one has been obtained by P. B. Demorest *et al.* from measurements of pulsar J1614-2230 [198]. This yields the lower bound of maximum NS mass, $M = (1.97 \pm 0.04) M_{\odot}$ and is a strong constraint. The present hadron model yields a consistent result with both the observations.

Next, we consider the quark-hadron transition with the Maxwell construction by assuming that the transition is the first-order. The transition occurs, when the two phases satisfy the conditions

$$\mu_{\rm u} + 2\mu_{\rm d} = \mu_{\rm n}, \tag{4.35}$$

$$P_{\rm Q}(\mu_{\rm u}, \mu_{\rm d}) = P_{\rm H}(\mu_{\rm n}). \tag{4.36}$$

Here we do not consider the finite-size effects due to the Coulomb interaction and the

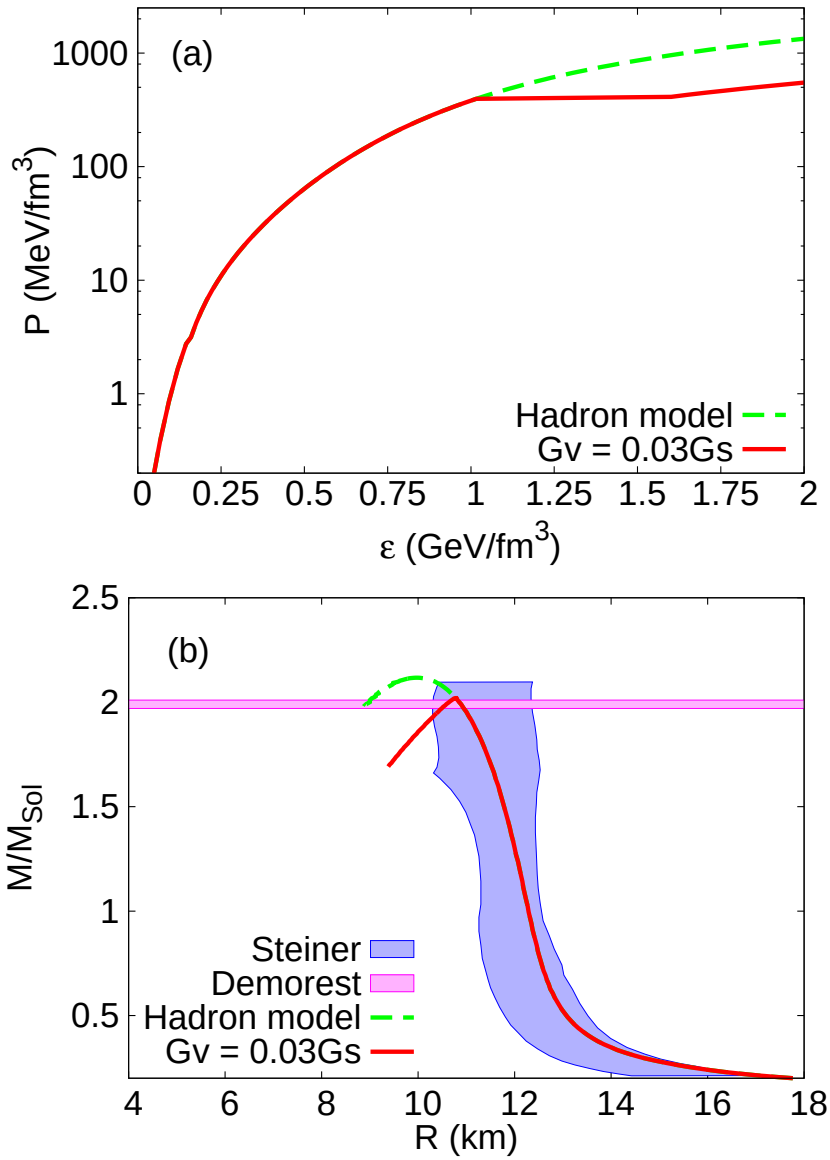

Fig. 4.5 (a) The equation of state and (b) the mass-radius relation obtained by the neutron matter with and without the quark-hadron transition. The two observation data are taken from Ref. [198, 199].

surface tension [219]. We will study these effects on the EoS in the future.

Once the quark phase appears as a consequence of the quark-hadron phase transition, it softens the EoS. The quark-matter part of the EoS depends on the strength of $G_{\rm V}$; more precisely, it becomes hard as $G_{\rm V}$ increases. Hence, the lower bound of $G_{\rm V}$ is determined from the $2M_{\odot}$-NS observation. The lower bound of such $G_{\rm V}$ is $0.03G_{\rm S}$,

as shown below. Figure 4.5 shows (a) the EoS and (b) the MR-relation determined by the present hybrid model. The solid line shows the result of the hybrid model with $G_{\rm V} = 0.03G_{\rm S}$, while the dashed line represents the result of the hadron model, i.e., the hybrid model with $G_{\rm V} = \infty$. The hybrid model is thus consistent with the $2M_\odot$-NS observation, when $G_{\rm V} \geq 0.03G_{\rm S}$.

Strictly speaking, the $\mu_{\rm B}$ dependence of v breaks the thermodynamic consistency

$$\begin{aligned} \frac{\partial P_{\rm B}}{\partial \tilde{\mu}_{\rm B}} &= \tilde{n}_{\rm B} \\ &= \frac{n_{\rm B}}{1 - v n_{\rm B}}, \end{aligned} \tag{4.37}$$

but the breaking effect is small in the present analysis on the MR relation. At $T = 0$ of our interest, the left-hand side of Eq. (4.37) can be rewritten into

$$\begin{aligned} \frac{\partial P_{\rm B}}{\partial \tilde{\mu}_{\rm B}} &= \frac{\partial P_{\rm B}}{\partial \mu_{\rm B}} \frac{\partial \mu_{\rm B}}{\partial \tilde{\mu}_{\rm B}} \\ &= \frac{\partial P_{\rm B}}{\partial \mu_{\rm B}} \left(1 + v\tilde{n}_{\rm B} + \frac{\partial v}{\partial \tilde{\mu}_{\rm B}} P_{\rm B} \right) \end{aligned} \tag{4.38}$$

in Fig. 4.6, the breaking term $A \equiv (\partial v/\partial \tilde{\mu}_{\rm B}) P_{\rm B}$. is plotted as a function of the baryon-number density ($n_{\rm B}$). The term is much smaller than 1 even at high densities and hence the thermodynamic consistency is satisfied with good accuracy.

4.3.2 Finite temperature

In this section, we consider the symmetric matter by setting $\mu_{\rm p} = \mu_{\rm n} = \mu_{\rm B}$ and $\mu_{\rm u} = \mu_{\rm d} = \mu_{\rm B}/3$. Understanding of the symmetric matter at finite T is important to elucidate early universe or heavy-ion collisions.

Figure 4.7 shows T dependence of (a) the pressure and (b) the energy density obtained by the hybrid model in comparison with LQCD results at vanishing chemical potential [190]. Here, T is normalized by the deconfinement transition temperature $T_{\rm c}$. The deconfinement transition is crossover at $\mu_{\rm B} = 0$ in both of LQCD simulations and the EPNJL model. The transition temperature defined by the peak of susceptibility is $T_{\rm c} = 174$ MeV for both the results [101]. The hybrid model (solid line) shows the first-order quark-hadron transition, whereas the LQCD simulations (closed squares) do the crossover transition. Except for the transition temperature $T \approx 1.1T_{\rm c}$ of the

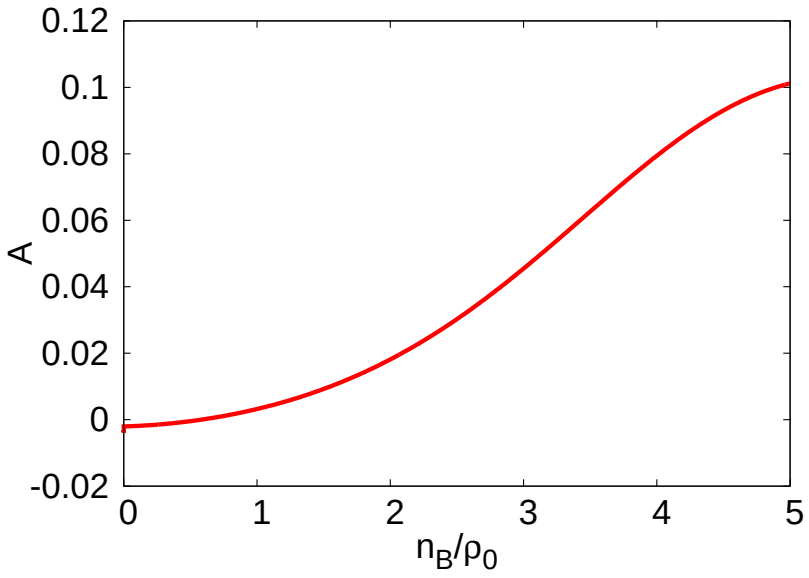

Fig. 4.6 Baryon-number density ($n_{\rm B}$) dependence of the breaking term (A) in Eq. (4.38) for the neutron matter.

first-order quark-hadron transition, the model results almost reproduce the LQCD results.

Figure 4.8 is the phase diagram in the $\mu_{\rm B}$-T plane. The thick solid line is the quark-hadron transition line obtained by the hybrid model with $G_{\rm V} = 0.03G_{\rm S}$. The transition is the first order everywhere. In this sense, this is an approximate result at least at $\mu_{\rm B}/T < 1$, since LQCD simulations show that the deconfinement (quark-hadron) transition is crossover there. As an important result, the first-order quark-hadron transition line is close to the crossover deconfinement transition line (dot-dashed line) obtained by the EPNJL model at $\mu_{\rm B}/T < 1$, where the deconfinement transition line is simply defined as a line satisfying $\Phi = 0.5$. Noting that the EPNJL model well simulates LQCD results at $\mu_{\rm B}/T < 1$, one can see that the present hybrid model is a rather good effective model even at small $\mu_{\rm B}/T$. The dashed and dotted lines correspond to the first-order and crossover chiral transition lines, whereas the closed square is the critical endpoint (CEP) of the chiral transition.

As already mentioned in Sec. 4.3.1, the present hybrid model is consistent with the NS observations at $T = 0$, when $G_{\rm V} \geq 0.03G_{\rm S}$. In the hybrid model with

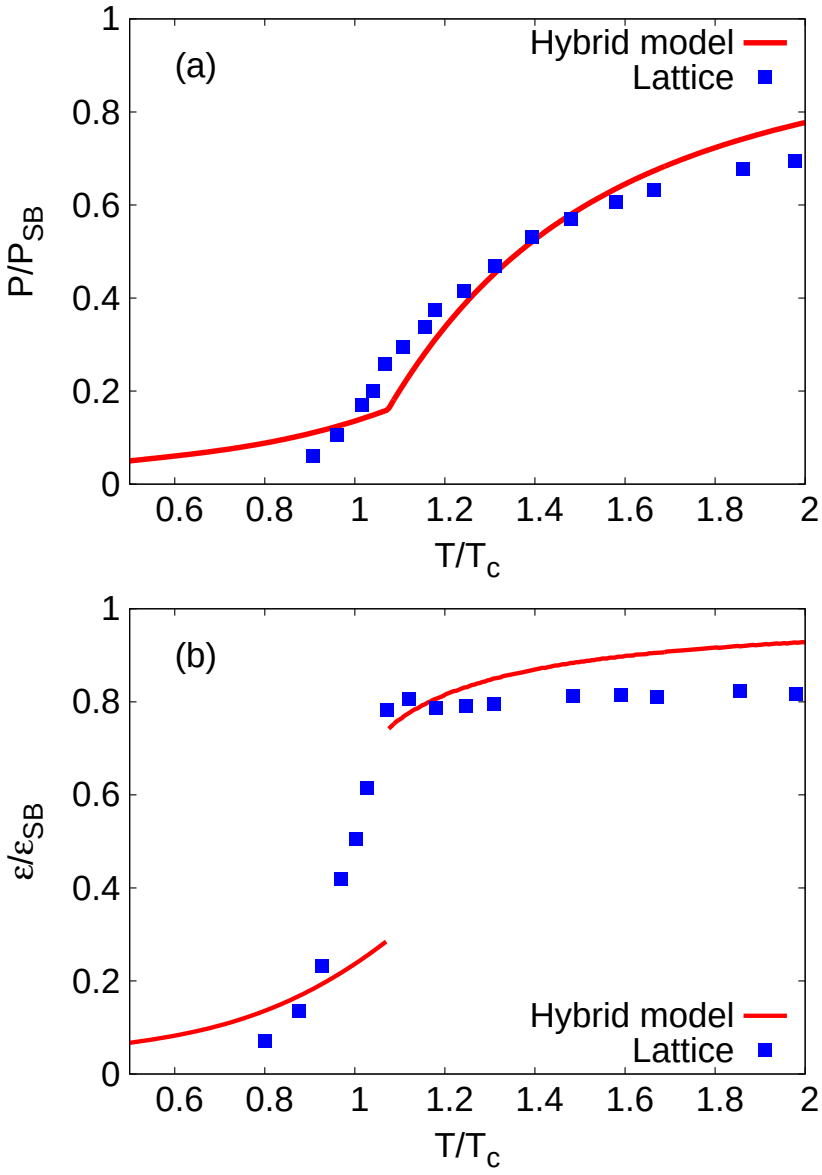

Fig. 4.7 T dependence of (a) the pressure and (b) the energy density obtained by the hybrid model at vanishing chemical potential. The results are normalized by their Stefan-Boltzmann limits. LQCD data is taken from Ref. [190].

$G_{\rm V} = 0.03G_{\rm S}$, the critical baryon-number chemical potential $\mu_{\rm B}^{\rm (c)}$ of the first-order quark-hadron transition at $T = 0$ is 1.6 GeV, as shown in Fig. 4.8. This is the lower bound of $\mu_{\rm B}^{\rm (c)}$, since $G_{\rm V}$ can vary from $0.03G_{\rm S}$ to ∞; actually, $\mu_{\rm B}^{\rm (c)}$ is shifted to higher $\mu_{\rm B}$ as $G_{\rm V}$ increases, as shown later in Fig. 4.9. This is the primary result of the present work. In the EPNJL model, meanwhile, the critical baryon-number chemical

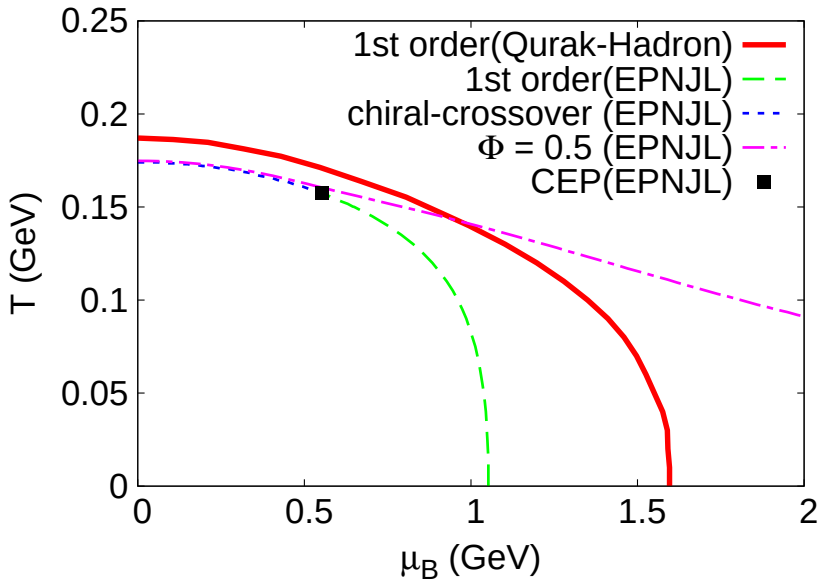

Fig. 4.8 Phase diagram in the $\mu_{\rm B}$-T plane. The solid line represents a quark-hadron transition line given by the hybrid model. The other lines and symbol are obtained by the EPNJL model. The dashed (dotted) line correspond to the first-order (crossover) chiral transition line, and the dot-dashed line is a contour line corresponds to $\Phi = 0.5$. The closed square is the critical endpoint (CEP).

potential of the chiral transition at $T = 0$ is 1 GeV. The point belongs to the hadron phase in the hybrid model. Thus, we do not have any conclusive result on the chiral transition at $T = 0$. This is an important problem to be solved in future.

In principle one can determine the strength of $G_{\rm V}$ from LQCD simulations present at $\mu_{\rm B}/T < 3$, but in practice the strength thus determined has large ambiguity [73,89]. Figure 4.9 shows the phase diagram in the $\mu_{\rm B}$-T plane predicted by the hybrid model with different values of $G_{\rm V}$. The dashed and solid lines correspond to the cases of $G_{\rm V} = 0.03G_{\rm S}$ and $0.2G_{\rm S}$, respectively. The phase transition line is insensitive to the variance of $G_{\rm V}$ at $\mu_{\rm B}/T < 3$, but rather sensitive at $\mu_{\rm B}/T \approx 6$. Thus the physics at $\mu_{\rm B}/T \approx 6$ is strongly related to the NS physics at $\mu_{\rm B}/T = \infty$. If the quark-hadron transition line at $\mu_{\rm B}/T \approx 6$ is determined by LQCD simulations or heavy-ion collision experiments, it will also determine $\mu_{\rm B}^{(\rm c)}$ more strictly.

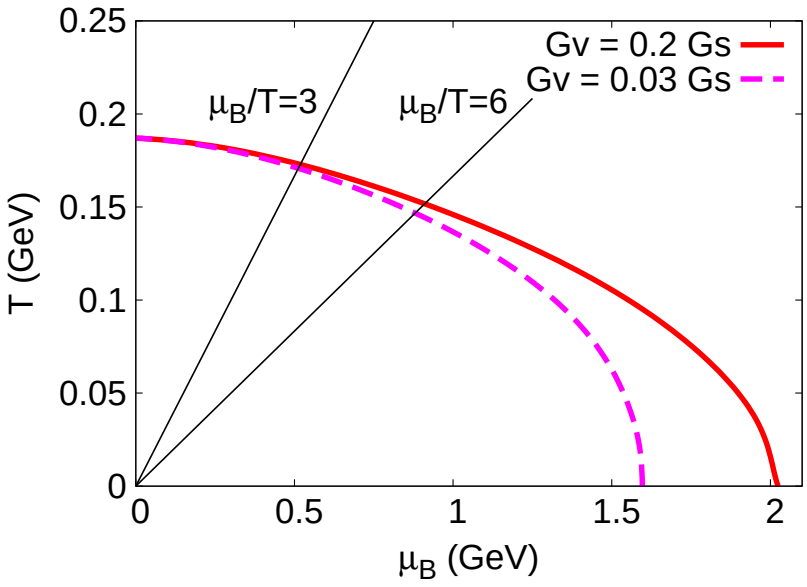

Fig. 4.9 Phase diagram in the $\mu_{\rm B}$-T plane. The dashed line is the result of the hybrid model with $G_{\rm V} = 0.03G_{\rm S}$; the line corresponds to the thick solid line in Fig. 4.8. The thick-solid line corresponds to the case of $G_{\rm V} = 0.2G_{\rm S}$. Two thin-solid lines mean lines of $\mu_{\rm B}/T = 3$ and 6, respectively.

4.4 Short summary

QCD phase diagram for finite $\mu_{\rm B}$ is still unknown because the first-principle LQCD simulation is not feasible there. However, information on this region can be obtained from by Neutron-star observations with the development of observation technique. In particular, the $2M_\odot$-NS measurement should give a strong constraint to the QCD phase transition at $T = 0$.

We have studied the QCD phase diagram in the whole region from $\mu_{\rm B}/T = 0$ to infinity, constructing the quark-hadron hybrid model that is consistent with LQCD results at $\mu_{\rm B}/T = 0$ and with NS observations, the neutron-matter EoS evaluated from the Ch-EFT 2NF and 3NF, and the EoS obtained by the heavy-ion collision measurements at $\mu_{\rm B}/T = \infty$. The EoS provided by the model preserves the causality even at high $n_{\rm B}$. At $n_{\rm B} < 2\rho_0$ the baryon part of the EoS agrees with the neutron-matter EoS constructed from the Ch-EFT 2NF and 3NF with the lowest-order Brueckner

theory (LOBT). The Ch-EFT provides a systematic framework of constructing 2NF and 3NF, and the 3NF yields a significant effect on the EoS at $n_{\rm B} > \rho_0$. In this sense, the use of the Ch-EFT, which respects symmetries of QCD, is inevitable to construct the neutron-matter EoS with no ambiguity.

We have determined the lower bound of the critical chemical potential ($\mu_{\rm B}^{(\rm c)}$) of the quark-hadron transition at $T = 0$ for the isospin-symmetric matter:

$$\mu_{\rm B}^{(\rm c)} \sim 1.6 \text{ GeV}. \tag{4.39}$$

This is the primary result of this work. In the NJL model, the first-order chiral transition occurs at $\mu_{\rm B}^{(\rm c)} = 1$ GeV, when $T = 0$. The point is located in the hadron phase in the hybrid model. The critical chemical potential of the chiral transition at $T = 0$ is thus unknown. In this sense, the NJL model is not good enough at $T = 0$. It is then highly required to introduce baryon degrees of freedom in the effective model.

We have also shown the interplay between the heavy-ion collision physics at $\mu_{\rm B}/T \approx 6$ and the NS physics at $\mu_{\rm B}/T = \infty$. If the vector coupling $G_{\rm V}$ is determined at $\mu_{\rm B}/T \approx 6$ from heavy-ion collision measurements, the information determines the critical chemical potential of the quark-hadron transition at $T = 0$ and hence properties of NS in the inner core. This fact strongly suggests that these two regions should be studied simultaneously.

Chapter 5

Summary

Elucidation of the QCD phase diagram is an important and interesting subject in hadron physics. Rich structure of the phase diagram is relevant to the cosmic evolution and neutron-star structure. Almost all the region of the diagram is still unknown, since the first-principle LQCD simulations are not feasible for finite density because of the sign problem. We have analyzed the QCD phase diagram by using the EPNJL model as a most reliable effective model. The model can treat confinement and spontaneous chiral-symmetry breaking simultaneously and quantitatively. We have applied the EPNJL model to three characteristic subjects:

(1) Quark mass dependence of RW endpoint
(2) θ parameter dependence of QCD phase diagram
(3) QCD phase diagram and NS observations

All the subjects are originated in nonperturbative properties of QCD vacuum.

At pure-imaginary chemical potential discussed in subject (1), LQCD simulations are feasible, since they have no sign problem there. The RW endpoint is a critical endpoint of the first-order RW phase transition that appears at $\theta_{\rm q} = \pi/3$. Quark-mass dependence of the order of the RW endpoint is analyzed by LQCD simulations.

In subject (1), we have extended the three-flavor PNJL model by introducing an entanglement vertex $G_{\rm S}(\Phi)$. The entanglement PNJL (EPNJL) model reproduces 2+1 flavor LQCD data for the chiral transition at $\mu = 0$ and degenerate three-flavor

LQCD data calculated very lately for the ordeer of the RW endpoint. The EPNJL model is thus quite reliable. We have then drawn the three-flavor phase diagram for the RW endpoint in the m_l-m_s plane by using the EPNJL model. This is the first prediction for the phase diagram.

θ parameter discussed in subject (2) is a free parameter of QCD and is related to topological nature of QCD vacuum and $U(1)_{\rm A}$ anomaly. The θ term can be treated as an external field to QCD and is a useful probe to investigate nonperturbative properties of QCD vacuum. However, the QCD phase structure for finite θ is unknown, since LQCD simulations have the sign problem there.

In subject (2), we have investigated effects of the theta vacuum on the QCD phase diagram for the realistic 2+1 flavor system, using the three-flavor PNJL and EPNJL models. The effects can be easily understood through the θ-dependent mass terms. The θ-odd mass, $m_l \sin(\theta/2)$, little affects the dynamics, since m_l is much smaller than $\Lambda_{\rm QCD}$ as a typical scale of QCD. The dynamics is therefore mainly governed by the θ-even mass, $m_l \cos(\theta/2)$. In the θ-even mass, the increase of θ corresponds to the decrease of m_l with m_s fixed. This means that the chiral transition becomes strong as θ increases. This is realized in the results of the EPNJL model and the transition becomes the first order even at $\mu = 0$ when θ is large. Moreover, we have proposed a way of circumventing the sign problem in LQCD simulations with finite θ, using the PNJL model. We have estimated the average reweighting factor $\langle R(\theta) \rangle$ by using the two-flavor PNJL model and have found a good reference system in the reweighting method.

For finite $\mu_{\rm B}$ discussed in subject (3), the QCD phase diagram is not known at all, because the first-principle LQCD simulations have the sign problem there. However, information on this region can be obtained from neutron-star (NS) observations through the development of observation technique. In particular, the $2M_\odot$-NS measurement yields a strong constraint on the QCD phase transition at $T = 0$.

In subject (3), we have studied the QCD phase diagram in the whole region from $\mu_{\rm B}/T = 0$ to infinity, constructing the quark-hadron hybrid model that is consistent with LQCD results at $\mu_{\rm B}/T = 0$ and NS observations and heavy-ion collision measurements at $\mu_{\rm B}/T = \infty$. The EoS determined by the model preserves the causality even

at high $n_{\rm B}$. At $n_{\rm B} < 2\rho_0$, the baryon part of the EoS agrees with the neutron-matter EoS constructed from the Ch-EFT 2NF and 3NF with the lowest-order Brueckner theory (LOBT). Here the Ch-EFT is a systematic framework of constructing 2NF and 3NF, and the 3NF yields a significant effect on the EoS at $n_{\rm B} > \rho_0$. In this sense, use of the Ch-EFT, which respects symmetries of QCD, is inevitable to construct the neutron-matter EoS with no ambiguity. We have determined the lower bound of the critical chemical potential of the quark-hadron transition at $T = 0$:

$$\mu_{\rm B}^{\rm (c)} \sim 1.6 \text{ GeV}. \tag{5.1}$$

This is the primary result of this thesis. In the NJL model, the first-order chiral transition occurs at $\mu_{\rm B}^{\rm (c)} = 1$ GeV, when $T = 0$. The point is located in the hadron phase in the hybrid model. The critical chemical potential of the chiral transition at $T = 0$ is thus unknown. In this sense, the NJL model is not good enough at $\mu_{\rm B}/T = \infty$. It is then highly required to introduce baryon degrees of freedom in the effective model.

Throughout all the studies on subjects (1)-(3), we can understand all the regions of the QCD phase diagram by using a common low-energy effective model of QCD, that is the EPNJL model. This indicates that the QCD phase diagram can be described by a single effective model for $T \lesssim 600$ MeV and $\mu_{\rm q} \lesssim 600$ MeV. In particular, the EPNJL model is quite consistency with LQCD data, as shown in Chap.2. This means that the model yields a good picture to understand QCD phase structure at $\mu_{\rm q}/T < 1$. However, as shown in chapter 4, the baryonic degrees of freedom are crucial to describe high-density QCD matter, but not included in the PNJL-type models completely. We should improve the EPNJL model along this line. This is with yield an essential progress to understand QCD dynamics including the confinement mechanism.

Acknowledgments

First of all, I am deeply grateful to the supervisor, Prof. Masanobu Yahiro. He gives me a lot of opportunities of learning and warm encouragement. Without his guidance and persistent help this thesis would not have been possible.

I would like to thank Associate Prof. Hiroaki Kouno who gave me a lot of useful comments and helpful discussions on this thesis. Through many discussions, I was able to obtain much beneficial knowledge. Also, I appreciate the feedback offered by the collaborators, Michio Kohno, Nobutoshi Yasutake, and Junichi Takahashi.

I wish to express my deep appreciation to Associate Prof. Yoshifumi R. Shimizu, Assistant Prof. Kazuyuki Ogata, and Assistant Prof. Takuma Matsumoto. They gave me much important knowledge of nuclear physics through the seminars and discussions. I would like to thank Assistant Prof. Ken-ichi Okumura for her helpful comments in the Front Researcher Development program. I would like to thank my friends in the Nuclear Theory Group and other divisions in Kyushu University.

This work is helped by a lot of Master theses which are not published in any journals. I want to thank the authors, Takanori Kai, Kagayaki Oda, Yasuhiro Saito, and Kunihiro Nagano.

I would like to express the deepest appreciation to Yuki Yamaji, Fumiko Watanabe, Yuko Megumi, Saori Shigematsu, Hiromi Tsuchijima, Megumi Ieda, and Noriko Taguchi for their practical supports.

This work was supported by the Research Fellowships of the Japan Society for the Promotion of Science(JSPS) for Young Scientists.

Finally and most of all, I thank my family for their patient support and encouragement

Bibliography

[1] K. Yagi, T. Hatsuda and Y. Miake, *Quark-Gluon Plasma* (Cambridge, 2010).

[2] J. Beringer, *et al* (Particle Data Group), Phys. Rev. D **86**, 010001 (2012).

[3] A. A. Belavin, A. M. Polyakov, A. S. Schwartz, and Yu. S. Tyupkin, Phys. Lett. B **59**, 85 (1975).

[4] G. 't Hooft, Phys. Rev. Lett. **37**, 8 (1976);

[5] G. 't Hooft, Phys. Rev. D**14**, 3432 (1976); **18**, 2199(E) (1978).

[6] C. G. Callan, R. F. Dashen, and D. J. Gross, Phys. Lett. **B63**, 334 (1976).

[7] J. Jackiw and C. Rabbi, Phys. Rev. Lett. **37**, 172 (1976).

[8] C. A. Baker *et al.*, Phys. Rev. Lett. **97**, 131801 (2006).

[9] V. Baluni, Phys. Rev. D **19**, 2227(1979).

[10] R. Crewther, P. di Vecchia, G. Veneziano and E. Witten, Phys. Lett. **88B**, 123(1979);91B, 487(1980)(E).

[11] K. Kawarabayashi and N. Ohta, Nucl. Phys. B **175**, 477 (1980).

[12] K. Kawarabayashi and N. Ohta, Prog. Theor. Phys. **66**, 1789 (1981).

[13] N. Ohta, Prog. Theor. Phys. **66**, 1408 (1981); [Erratum-ibid. **67** (1982) 993].

[14] L. D. McLerran nd B. Svetitsky, Phys. Rev. D **24**, 450 (1981).

[15] B. Svetitsky and Y. Yaffe, Nucl. Phys. B **210**, 423 (1983).

[16] V. P. Nair, *Quantum Field Theory, A Modern Perspective* (Springer, 2004).

[17] S. Weinberg, *The quantum theory of fields* (Cambridge, 1995).

[18] S. Coleman, *Aspects of symmetry* (Cambridge, 1985).

[19] E. Vicari and H. Panagopoulos, Phys. Rept. **470**, 93 (2009).

[20] H. Quinn, arXiv:0110050 [hep-ph] (2001).

[21] H. Forkel, arXiv:0009136 [hep-ph] (2000).

[22] K. Fujikawa, Phys. Rev. Lett. **42**, 1195 (1979).

[23] K. Fujikawa, Phys. Rev. D **21**, 2848 (1980).

[24] J. C. Collins and M. J. Perry, Phys. Rev. Lett. **34**, 1353 (1975).

[25] N. Cabibbo and G. Parisi, Phys. Lett. B **58**, 67 (1975).

[26] R. Hagedorn, Nouvo Cimento Suppl. **3**, 147 (1965).

[27] R. Hagedorn and J. Ranft, Nouvo Cimento Suppl. **6**, 169 (1968).

[28] J. Cleymans, R. V. Gavai, and E. Suhonen, Phys. Rept. **130**, 217 (1986).

[29] K. Rajagopal, Nucl. Phys. A **661**, 150 (1999).

[30] D. H. Rischke, Prog. Part. Nucl. Phys. **52**, 197 (2004).

[31] M. Stephanov, Prog. Theor. Phys. Suppl. **153**, 139 (2004).

[32] M. Stephanov, Proc. Sci. LATTICE2006, 024 (2006).

[33] L. McLerran, Nucl. Phys. B (Proc. Suppl.) **195**, 275 (2009).

[34] W. Weise, Prog. Theor. Phys. Suppl. **186**, 390 (2010).

[35] K. Fukushima and T. Hatsuda, Rep. Prog. Phys. **74**, 014001 (2011).

[36] K. Fukushima, J. Phys. G: Nucl. Part. Phys. **39**, 013101 (2012).

[37] W. Weise, Prog. Part. Nucl. Phys. **67**, 299 (2012).

[38] K. Fukushima and C. Sasaki, Prog. Part. Nucl. Phys. **72**, 99 (2013).

[39] R. Rapp, T. Schäfer, E. V. Shuryak, and M. Velkovsky, Phys. Rev. Lett. **81**, 53 (1998).

[40] M. G. Alford, K. Rajagopal, and F. Wilczek, Phys. Lett. B **422**, 247 (1998).

[41] Y. Aoki, G. Endrődi, Z. Fodor, S. D. Katz and K. K. Szabó, Nature **443**, 675 (2006).

[42] A. Bazavov, *et al.*, Phys. Rev. D **85**, 054503 (2012).

[43] S. Borsanyi, G. Endrődi, Z. Fodor, A. Jakovác, S. D. Katz, S. Krieg, C. Ratti, and K. K. Szabó, JHEP **1011**, 077 (2010).

[44] S. Borsányi, Z. Fodor, C. Hoelbling, S. D. Katz, S. Krieg, C. Ratti, and K. K. Szabo, J. High Energy Phys. 09 (2010) 073.

[45] S. Borsanyi, G. Endrodi, Z. Fodor, S. D. Katz, S. Krieg, C. Ratti, C. Schroeder, and K. K. Szabó, Proc. Sci. LATTICE2011, 201 (2011).

[46] A. Bazavov, C. Bernard, C. DeTar, J. Foley, S. Gottlieb, U. M. Heller, J. E. Hetrick, J. Laiho, L. Levkova, J. Osborn, R. Sugar, D. Toussaint, R. S. Van de

Water, R. Zhou, Proc. Sci. LATTICE2013, 154 (2013).

[47] *Quark-Gluon Plasma. New Discoveries at RHIC: Case for the Strongly Interacting Quark-Gluon Plasma* Nucl. Phys. A **750** (2005).

[48] E. Shuryak, Prog. Part. Nucl. Phys. **62**, 48 (2009).

[49] E. Shuryak, Nucl. Phys. B (Proc. Suppl.) **195**, 111 (2009).

[50] O. Akerlund and P. de Forcrand, arXiv:1312.1543 [hep-lat] (2013).

[51] Jens O. Andersen, Lars E. Legangera, Michael Strickland, and Nan Suc, Phys. Lett. B **696**, 468 (2011).

[52] P. J. Siemens, Nature **305**, 410 (1983).

[53] G. F. Bertsch and P. J. Siemens, Phys. Lett. B **126**, 9 (1983).

[54] P. Chomaz, arXiv:0410024 [nucl-ex] (2004).

[55] C. E. DeTar and U. M. Heller Eur. Phys. J. A **41**, 405 (2009).

[56] F. Karsch, Lect. Notes Phys. **583**, 209 (2002).

[57] E. Laermann and O. Philipsen, Ann. Rev. Nucl. Part. Sci. **53**, 163 (2003).

[58] S. Muroya, A. Nakamura, C. Nonaka, and T. Takahashi, PTP. Vol. **110** No. 4, 615 (2003).

[59] O. Philipsen, arXiv:1009.4089 [hep-lat] (2010).

[60] K. G. Wilson, Phys. Rev. D **8**, 2445 (1974).

[61] A. Bazavov, *et al.*, Rev. Mod. Phys. **82**, 1349 (2010).

[62] T. Inoue, N. Ishii, A. Aoki, T. Doi, T. Hatsuda, Y. Ikeda, K. Murano, H. Nemura, and K. Sasaki Prog. Theor. Phys. **124**, 591 (2010).

[63] H. S. Chen and X. Q. Luo, Phys. Rev. D **72**, 034504 (2005).

[64] H. S. Chen and X. Q. Luo, arXiv:hep-lat/0702025 (2007).

[65] M. D'Elia and M. P. Lombardo, Phys. Rev. D **67**, 014505 (2003).

[66] M. D'Elia and M. P. Lombardo, Phys. Rev. D **70**, 074509 (2004).

[67] M. D'Elia, F. D. Renzo, and M. P. Lombardo, Phys. Rev. D **76**, 114509 (2007).

[68] P. de Forcrand and O. Philipsen, Nucl. Phys. B **642**, 290 (2002).

[69] P. de Forcrand and O. Philipsen, Nucl. Phys. B **673**, 170 (2003).

[70] D. T. Son and M. A. Stephanov, Phys. Rev. Lett. **86**, 592 (2001).

[71] A. Bhattacharyya, P. Deb, S. K. Ghosh, and R. Ray, Phys. Rev. D **82**, 014021 (2010).

[72] A. Bhattacharyya, P. Deb, A. Lahiri, and R. Ray, Phys. Rev. D **83**, 014011 (2011).

[73] N. Bratovic, T. Hatsuda, and W. Weise, Phys Lett. B **719**, 131 (2013).

[74] G. A. Contrera, A. G. Grunfeld, and D. Blaschke, arXiv:1207.4890 [hep-ph] (2012).

[75] K. Fukushima, Phys. Lett. B **591**, 277 (2004).

[76] K. Fukushima, Phys. Rev. D **77**, 114028 (2008).

[77] K. Fukushima, D. E. Kharzeev, and H. J. Warringa, Phys. Rev. D **78**, 074033 (2008).

[78] K. Fukushima, Phys. Rev. D **78**, 114019 (2008).

[79] K. Fukushima, M. Ruggieri, and R. Gatto, Phys. Rev. D **81**, 114031 (2010).

[80] K. Fukushima and K. Kashiwa, Phys. Lett. B **723**, 360 (2013). arXiv:1206.0685 [hep-ph] (2012).

[81] R. Gatto, and M. Ruggieri, Phys. Rev. D **83**, 034016 (2011).

[82] T. Kähärä and K. Tuominen, Phys. Rev. D **80**, 114022 (2009).

[83] K. Kashiwa, M. Yahiro, H. Kouno, M. Matsuzaki, and Y. Sakai, J. Phys. G: Nucl. Part. Phys. **36**, 105001 (2009).

[84] K. Kashiwa, R. D. Pisarski, and V. V. Skokov, Phys. Rev. D **85**, 114029 (2012).

[85] K. Kashiwa, H. Kouno, and M. Yahiro, Phys. Rev. D **80**, 117901 (2009).

[86] K. Kashiwa, R. D. Pisarski, Phys. Rev. D **87**, 096009 (2013).

[87] H. Kouno, Y. Sakai, K. Kashiwa, and M. Yahiro, J. Phys. G: Nucl. Part. Phys. **36**, 115010 (2009).

[88] H. Kouno, Y. Sakai, T. Sasaki, K. Kashiwa, and M. Yahiro, Phys. Rev. D **83**, 076009 (2011).

[89] O. Lourenço, M. Duta, T. Frederico, A. Delfino, and M.Malheiro, Phys. Rev. D **85**, 097504 (2012).

[90] T. Matsumoto, K. Kashiwa, H. Kouno, K. Oda, and M. Yahiro, Phys. Lett. B **694**, 367 (2011).

[91] E. Megías, E. R. Arriola, and L. L. Salcedo, Phys. Rev. D **74**, 065005 (2006).

[92] P. N. Meisinger and M. C. Ogilvie, Phys. Lett. B **379**, 163 (1996).

[93] C. Ratti, M. A. Thaler, and W.W eise, Phys. Rev. D **73**, 014019 (2006).

[94] S. Rößner, C. Ratti, and W. Weise, Phys. Rev. D **75**, 034007 (2007).

[95] M. C. Ruivo, M. Santos, P. Costa and C. A. de Sousa, Phys. Rev. D **85**, 036001 (2012).

[96] M. C. Ruivo, P. Costa and C. A. de Sousa, Phys. Rev. D **86**, 116007 (2012).

[97] Y. Sakai, K. Kashiwa, H. Kouno, and M. Yahiro, Phys. Rev. D **77**, 051901(R) (2008).

[98] Y. Sakai, K. Kashiwa, H. Kouno, and M. Yahiro, Phys. Rev. D **78**, 036001 (2008).

[99] Y. Sakai, K. Kashiwa, H. Kouno, M. Matsuzaki, and M. Yahiro, Phys. Rev. D **78**, 076007 (2008).

[100] Y. Sakai, K. Kashiwa, H. Kouno, M. Matsuzaki, and M. Yahiro, Phys. Rev. D **79**, 096001 (2009).

[101] Y. Sakai, H. Kouno, and M. Yahiro, J. Phys. G: Nucl. Part. Phys. **37**, 105007 (2010).

[102] Y. Sakai, T. Sasaki, H. Kouno, and M. Yahiro, Phys. Rev. D **82**, 096007 (2010).

[103] Y. Sakai, T. Sasaki, H. Kouno, and M. Yahiro, Phys. Rev. D **82**, 076003 (2010).

[104] Y. Sakai, H. Kouno, T. Sasaki, and M. Yahiro, Phys. Lett. B **705**, 349 (2011).

[105] Y. Sakai, T. Sasaki, H. Kouno, T. Sasaki, and M. Yahiro, J. Phys. G: Nucl. Part. Phys. **39**, 035004 (2012).

[106] T. Sasaki, Y. Sakai, H. Kouno, and M. Yahiro, Phys. Rev. D **84**, 091901(R) (2011).

[107] T. Sasaki, J. Takahashi, Y. Sakai, H. Kouno, and M. Yahiro, Phys. Rev. D **85**, 056009 (2012).

[108] T. Sasaki, H. Kouno, and M. Yahiro, Phys. Rev. D **87**, 056003 (2013).

[109] T. Sasaki, N. Yasutake, M. Kohno, H. Kouno, and M. Yahiro, arXiv:hep-ph/1307.0681.

[110] T. Sasaki, Y. Sakai, H. Kouno, and M. Yahiro, Phys. Rev. D **82**, 116004 (2010).

[111] T. Sasaki, J. Takahashi, Y. Sakai, H. Kouno, and M. Yahiro, Proc. Sci. LATTICE2012 (2012) 076.

[112] B. -J. Schaefer, J. M. Pawlowski, and J.Wambach, Phys. Rev. D **76**, 074023 (2007).

[113] G. Y. Shao, M. Di. Toro, V. Greco, M. Colonna, S. Plumari, B. Liu, and Y. X.

Liu, Phys. Rev. D **84**, 034028 (2011).

[114] G. Y. Shao, M. Colonna, M. Di. Toro, Y. X. Liu, and B. Liu, Phys. Rev. D **87**, 096012 (2013).

[115] K. Yamazaki and T. Matsui Nucl. Phys. A **913**, 19 (2013).

[116] K. Yamazaki and T. Matsui, Nucl. Phys. A **922**, 237 (2014).

[117] Y. Nambu and G. Jona-Lasinio, Phys. Rev. **122**, 345 (1961).

[118] Y. Nambu and G. Jona-Lasinio, Phys. Rev. **124**, 246 (1961).

[119] M. Buballa, Phys. Rept. **407**, 205 (2005).

[120] T. Hatsuda and T. Kunihiro, Phys. Rept. **247**, 221 (1994).

[121] S. P. Klevansky, Rev. Mod. Phys. **64**, 649 (1992).

[122] M. Kobayashi and T. Maskawa, Prog. Theor. Phys. **44**, 1422 (1970).

[123] M. Kobayashi, H. Kondo, and T. Maskawa, Prog. Theor. Phys. **45**, 1955 (1971).

[124] O. Kaczmarek, F. Karsch, P. Petreczky, and Z. Zantow, Phys. Lett. B **543**, 41 (2002).

[125] F. Karsch and E. Laermann, Phys. Rev. D **50**, 6954 (1994)

[126] F. Karsch, E. Laermann, and A. Peikert, Nucl. Phys. B **605**, 579 (2001).

[127] K. Kashiwa, H. Kouno, T. Sakaguchi, M. Matsuzaki, and M. Yahiro, Phys. Lett. B **647**, 446 (2007).

[128] M. D'Elia and F. Sanfilippo, Phys. Rev. D **80**, 111501 (2009).

[129] K. -I. Kondo, Phys. Rev. D**82**, 065024 (2010).

[130] J. Braun, L. M. Haas, F. Marhauser, and J. M. Pawlowski, Phys. Rev. Lett. **106**, 022002 (2011).

[131] J. Braun and A. Janot, Phys. Rev. D **84**, 114022 (2011).

[132] C. Wetterich, Phys. Lett. B **301**, 90 (1991).

[133] P. Rehberg, S. P. Klevansky, and J. Hüfner, Phys. Rev. C **53**, 410 (1996).

[134] F. R. Brown, F. P. Butler, H. Chen, N. H. Christ, Z. Dong, and W. Schaffer, Phys. Rev. Lett **65**, 2491 (1990).

[135] G. Boyd, J. Engels, F. Karsch, E. Laermann, C. Legeland, M. Lütgemeier, and B. Petersson, Nucl. Phys. B **469**, 419 (1996).

[136] J. Kogut, M. Stone, H. W. Wyld, J. Shigemitsu, S. H. Shenker, and D. K. Sinclair Phys. Rev. Lett **48**, 1140 (1982).

[137] J. Kogut, M. Stone, H. W. Wyld, W. R. Gibbs, J. Shigemitsu, S. H. Shenker, and D. K. Sinclair Phys. Rev. Lett **50**, 393 (1983).

[138] J. Kogut, H. Matsuoka, M. Stone, H. W. Wyld , S. H. Shenker , J. Shigemitsu , and D. K. Sinclair Phys. Rev. Lett **51**, 869 (1983).

[139] H. Saito, S. Ejiri, S. Aoki, K. Kanaya, Y. Nakagawa, H. Ohno, K. Okuno, and T. Umeda, arXiv:1309.2445 [hep-lat] (2013).

[140] R. D. Pisarski and F. Wilczek, Phys. Rev. D **29**, 338 (1984).

[141] K. Rajagopal and F. Wilczek, Nucl. Phys. B **399**, 395 (1993).

[142] F. Wilczek, Int. J. Mod. Phys. A **7**, 3911 (1992); **7**, 6951(E) (1992).

[143] P. de Forcrand and O. Philipsen, J. High Energy Phys. **01**, 077 (2007).

[144] J.-W. Chen, K. Fukushima, H. Kohyama, K. Ohnishi, and U. Raha, Phys. Rev. D **80**, 054012 (2009).

[145] J.-W. Chen, K. Fukushima, H. Kohyama, K. Ohnishi, and U. Raha, Phys. Rev. D **81**, 071501(R) (2010).

[146] J.-W. Chen, H. Kohyama, and U. Raha, Phys. Rev. D **83**, 094014 (2011).

[147] M. Asakawa and K. Yazaki, Nucl. Phys. A **504**, 668 (1989).

[148] A. Barducci, R. Casalbuoni, S. de Curtis, R. Gatto, and G. Pettini, Phys. Lett. B **231**, 463 (1989).

[149] A. Barducci, R. Casalbuoni, G. Pettini, and R. Gatto, Phys. Rev. D **49**, 426 (1994).

[150] K. Kashiwa, M. Matsuzaki, H. Kouno, and M. Yahiro, Phys. Lett. B **657**, 143 (2007).

[151] A. Roberge and N. Weiss, Nucl. Phys. B **275**, 734 (1986).

[152] P. de Forcrand and O. Philipsen, Phys. Rev. Lett. **105**, 152001 (2010).

[153] K. Kanaya, Proc. Sci. LATTICE2010 (2010) 012.

[154] K. Kanaya, AIP Conf. Proc. **1343**, 57 (2011).

[155] W. Söldner, Proc. Sci. LATTICE2010 (2010) 215.

[156] J. Braun, B. Klein, H. -J. Pirner, and A. H. Rezaeian, Phys. Rev. D **73**, 074010 (2006).

[157] A. Dumitru, D. Röder, and J. Ruppert, Phys. Rev. D **70**, 074001 (2004).

[158] L. McLerran, E. Mottola and M. E. Shaposhnikov, Phys. Rev. D **43**, 2027

(1991).

[159] D. Kharzeev and A. Zhitnitsky, Nucl. Phys. A **797**, 67 (2007).

[160] M. A. Metlitski and A. R. Zhitnitsky, Nucl. Phys. B **731**, 309 (2005).

[161] M. A. Metlitski and A. R. Zhitnitsky, Phys. Lett. B**633**, 721 (2006).

[162] M. Dine, W. Fischler, and M. Srednicki, Phys. Lett. B **104**, 199 (1981).

[163] J. W. Kim, Phys. Rev. Lett. **43**, 103 (1979).

[164] R. D. Peccei and H. R. Quinn, Phys. Rev. D**16**, 1791 (1977).

[165] M. A. Shifman, A. I. Vainstein, and V. I. Zakharov, Nucl. Phys. B **166**, 493 (1980).

[166] A. R. Zhitnitsky, Sov. J. Nucl. Phys. **31**, 260 (1980).

[167] D. Kharzeev, Phys. Lett. B**633**, 260 (2006).

[168] B. I. Abelev *et al.* [STAR Collaboration], Phys. Rev. Lett. **103**, 251601 (2009).

[169] B. I. Abelev *et al.* [STAR Collaboration], Phys. Rev. C **81**, 054908 (2010).

[170] C. Vafa and E. Witten, Phys. Rev. Lett. **53**, 535 (1984).

[171] R. Dashen, Phys. Rev. D **3**, 1879 (1971).

[172] E. Witten, Ann. Phys. **128**, 363 (1980).

[173] G. Akemann, J. T. Lenaghan, and K. Splittorff, Phys. Rev. D **65**, 085015 (2002).

[174] M. Creutz, Phys. Rev. Lett.**92**, 201601 (2004).

[175] A. V. Smilga, Phys. Rev. D **59**, 114021 (1999).

[176] M. H. G. Tytgat, Phys. Rev. D **61**, 114009 (2000).

[177] P. di Vecchia and G. Veneziano, Nucl. Phys. B **171**, 253 (1980).

[178] D. Boer and J. K. Boomsma, Phys. Rev. D **78**, 054027 (2008).

[179] J. K. Boomsma and D. Boer, Phys. Rev. D **80**, 034019 (2009).

[180] B. Chatteriee, H. Mishra, and A. Mishra, Phys. Rev. D **85** 114008 (2012).

[181] T. Fujihara, T. Inagaki, and D. Kimura, Prog. Theor. Phys. **117**, 139 (2007).

[182] G. 't Hooft, Phys. Rept. **142**, 357 (1986).

[183] A. Barducci, R. Casalbuoni, G. Pettini, and R. Gatto, Phys. Lett. B **301**, 95 (1993).

[184] M. D'Elia and F. Negro, Phys. Rev. Lett. **109**, 072001 (2012).

[185] M. Frank, M. Buballa, and M. Oertel, Phys. Lett. B **562**, 221 (2003).

[186] H. Hansen, W. M. Alberio, A. Beraudo, A. Molinari, M. Nardi, and C. Ratti,

Phys. Rev. D **75**, 065004 (2007).

[187] J. O. Andersen, L. T. Kyllingstad, and K. Splittroff, J. High Energy Phys. **01**, 055 (2010).

[188] T. Sasaki, H. Kouno, and M. Yahiro, J. Phys. Conf. Ser. **432**, 012031 (2013).

[189] M. D'Elia and F. Sanfilippo, Phys. Rev. D **80**, 014502 (2009).

[190] A. Ali Khan *et al*, Phys. Rev. D **64**, 074510 (2001).

[191] S. Borsanyi, Z. Fodor, S. D. Katz, S. Krieg, C. Ratti, and K. K. Szabó, JHEP **1201**, 038 (2012).

[192] A. Bazavov, *et al.*, Phys. Rev. D **86**, 034509 (2012).

[193] R. Machleidt, Phys. Rev. C **63**, 024001 (2001).

[194] S. Weinberg, Physica A **96**, 327 (1979).

[195] P. Danielewicz, R. Lacey, and W. G. Lynch, Science **298**, 1592 (2002).

[196] J. M. Lattimer, Annu. Rev. Nucl. Part. Sci. **62**, 485 (2012).

[197] J. Antoniadis, *et al*, Science **340**, 1233232 (2013).

[198] P. B. Demorest, T. Pennucci, S. M. Ransom, M. S. E. Roberts, and J. W. T. Hessels, Nature **467**, 1081 (2010).

[199] A. W. Steiner, J. M. Lattimer, and E. F. Brown, Astrophys. J. **722**, 33 (2010).

[200] E. Epelbaum, W. Göckle, and U. -G. Meißner, Nucl. Phys. A **747**, 362 (2005).

[201] D. Blaschke, D. G. Dumm, A. G. Grunfeld, T. Klähn, and N. N. Scoccola, Phys. Rev. C **75**, 065804 (2007).

[202] L. Bonanno and A. Sedrakian, Astron. Astrophys. **539**, A16 (2012).

[203] V. A. Dexheimer and S. Schramm, Phys. Rev. D **81**, 015804 (2010).

[204] V. A. Dexheimer, J. Steinheimer, R. Negreiros, and S. Schramm, Phys. Rev. D **87**, 015804 (2013).

[205] N. Ippolito, M. Ruggieri, D. Rischke, A. Sedrakian and F. Weber, Phys. Rev. D **77**, 023004 (2008).

[206] H. -J. Schulze and T. Rijken, Phys. Rev. C **84**, 035801 (2011); and references therein.

[207] T. Maruyama, S. Chiba, H. -J. Schulze, and T. Tatsumi, Phys. Rev. D **76**, 123015 (2007).

[208] K. Masuda, T. Hatsuda, and T. Takatsuka, Astrophys. J. **764**, 12 (2013).

[209] D. H. Rischke, M. I. Gorenstein, H. Stöcker, and W. Greiner, Z. Phys. C **51**, 485 (1991).

[210] J. Steinheimer, S. Schramm, and H. Stöcker, J. Phys. G: Nucl. Part. Phys. **38**, 035001 (2011).

[211] M. Baldo and F. Burgio, Lect. Notes Phys. **578**, 1 (2001).

[212] M. Kohno, Phys. Rev. C **86**, 061301(R) (2012).

[213] R. B. Wiringa, V. G. J. Stoks, and R. Schiavilla, Phys. Rev. C **51**, 38 (1995).

[214] A. Akmal, V. R. Pandharipande, and D. G. Ravenhall, Phys. Rev. C **58**, 1804 (1998).

[215] T. Krüger, I. Tews, K. Hebeler, and A. Schwenk, arXiv:1304.2212 [nucl-th] (2013).

[216] S. L. Shapiro and S. A. Teukolsky, *Black Holes, White Dwarfs, and Neutron Stars* (John Wiley & Sons, New York, 1983).

[217] G. Baym, C. Pethick, and P. Sutherland, Astrophys. J. **170**, 99 (1971).

[218] T. Maruyama, N. Yasutake, and T. Tatsumi, Prog. Theor. Phys. Suppl. **186**, 69 (2010).

[219] N. Yasutake, T. Noda, H. Sotani, T. Maruyama, and T. Tatsumi, *Recent Advances in Quarks Research*, Nova, (2013), Chap.4, pp.63, ISBN 9781622579709, arXiv:1208.0427[astro-ph].